HARVARD UNIVERSITY
Graduate School of Arts and Sciences

DISSERTATION ACCEPTANCE CERTIFICATE

The undersigned, appointed by the

Department of Physics

have examined a dissertation entitled

Laser cooling and 1D magneto-optical trapping of calcium monohydroxide

presented by Louis William Baum

candidate for the degree of Doctor of Philosophy and hereby certify that it is worthy of acceptance.

Signature _____

Typed name: Professor John Doyle, Chair

Signature _____

Typed name: Professor Cora Dvorkin

Signature _____

Typed name: Professor Markus Greiner

Date: May 4, 2020

Laser cooling and 1D magneto-optical trapping of calcium monohydroxide

a dissertation presented
by
Louis William Baum
to
The Department of Physics

in partial fulfillment of the requirements
for the degree of
Doctor of Philosophy
in the subject of
Physics

Harvard University
Cambridge, Massachusetts
May 2020

Thesis advisor: Professor John Doyle Louis William Baum

Laser cooling and 1D magneto-optical trapping of calcium monohydroxide

Abstract

The rich internal structure of polyatomic molecules has inspired a number of theoretical proposals exploring a myriad of unique scientific and engineering frontiers, including quantum simulation and next-generation searches for physics beyond the standard model. Establishing full control over these complex quantum objects is likely necessary to harness their full potential; however, the same rich internal structure that gives rise to the immense scientific potential of polyatomic molecules also makes manipulating them a daunting task. In the past decade there has been considerable progress in the production, cooling, and control of diatomic species using direct laser cooling and magneto-optical trapping. This dissertation focuses on extending direct laser cooling and trapping to polyatomic molecules.

Direct laser cooling of triatomic radical calcium monohydroxide (CaOH) is demonstrated. This molecules is a prototypical example of a broad class of polyatomic molecules that includes symmetric and asymmetric tops. Transverse magneto-optical trapping is demonstrated, establishing the ability to scatter an unprecedented number of photons in a polyatomic species. An understanding of previously unappreciated intricacies of molecular structure is developed, that explains observations of novel vibrational decay pathways. High resolution spectroscopy

of hybrid vibrational modes is performed. A laser cooling scheme is constructed that will support future efforts to use the full range of laser cooling and high-fidelity detection techniques required to implement an optical tweezer array of polyatomic molecules. Our experimental efforts demonstrate the feasibility of direct laser cooling applied to CaOH, up ending long-standing assumptions of the inextricable complexity of polyatomic molecules.

Contents

To my family.

Acknowledgments

Nothing can be achieved in a vacuum and I am deeply thankful for the support of everyone who has surrounded me throughout my time in graduate school. The Doyle Group has become a second family and I could not wish for a more supportive environment to pursue a PhD.

I would like to thank my advisor John Doyle for his guidance and support. John's passion and willingness to commit to new projects has allowed our research efforts to grow in unforeseen directions. I have learned a tremendous amount from him including how to approach new scientific questions, navigating grant applications, even the nuances of good champagne, and I could not have asked for a better mentor or advisor. The scientific rigor and problem solving skills I learned from him will enable success in my future endeavors. I would like to thank Markus Greiner and Cora Dvorkin for agreeing to be on my thesis committee. They have always been excited to learn about my research and help developed my own understanding by asking insightful questions.

The progress and success of the experiment would not have been possible without the other members of the Doyle Group. Most importantly I would like to acknowledge Ivan Kozyryev, who taught me the ropes. His creativity and drive pushed our research to new heights and allowed us to explore systems that I would not have dreamed possible. He has been a mentor, a partner, and is now a valued friend. He has my utmost gratitude for all of his support and I

could not imagine my PhD journey without him. I would also like to thank Boerge Hemmerling, Kyle Matsuda, Alex Sedlack, and Phelan Yu for their friendship and contributions to the SrOH experiments.

I am grateful to Löic Anderegg, Ben Augenbraun, Sean Burchesky, Yicheng Bao, and Zack Lasner who went above and beyond to help get the CaOH experiment off of the ground. To Christian Hallas, Nathaniel Vilas, Shivam Raval, and Debayan Mitra who were invaluable to the experimental efforts described in this thesis. I am grateful to Sandra for friendship, support, and advice as well as all the other members of the Doyle group who make it such a special place.

I have been lucky to leverage the expertise of an amazing group of people to help resolve the technical challenges of my research. Stan Contreau, Steve Sansone, and Jim MacArthur have all helped translate and solve many ill-posed problems and their company has never failed to brighten my day. I am grateful for many amazing people who deal with everything else and who efforts allow me to focus on the science. Thank you to Lisa, Silke, Adam, Jan, Clare, Sam and Erika for all of the help.

Beyond the research, graduate school is filed with obstacles, trials and tribulations and I would not be here without the love and the support of my friends and family. The friends I have made in graduate school have made this an exceptional experience. The relationships I have built during this time have kept me sane and provided amazing memories. My parents and sister have always been there for me and I will always be thankful for their unwavering support.

Finally but most importantly, I would like to thank my fiancée Rachel. Her encouragement and support mean the world to me and is the secret to my success in graduate school. From long-distance to quarantine, I can not imagine a better partner. Together, we will navigate any of life's challenges.

Citations to Previously Published Work

Parts of this dissertation have been reported previously in the following papers

- *Collisional relaxation of vibrational states of SrOH with He at 2 K.* I. Kozyryev, L. Baum, K. Matsuda, P. Olson, B. Hemmerling, and J. M. Doyle. New J. Phys. 17, 045003 (2015).
- *Radiation pressure force from optical cycling on a polyatomic molecule.* I. Kozyryev, L. Baum, K. Matsuda, B. Hemmerling, and J. M. Doyle. J. Phys. B: At. Mol. Opt. Phys. 49, 134002 (2016).
- *Proposal for laser cooling of complex polyatomic molecules.* I. Kozyryev, L. Baum, K. Matsuda, and J. M. Doyle. ChemPhysChem 17, 3641 (2016).
- *Sisyphus laser cooling of a polyatomic molecule.* I. Kozyryev, L. Baum, K. Matsuda, B. L. Augenbraun, L. Anderegg, A. P. Sedlack, and J. M. Doyle. Phys. Rev. Lett. 118, 173201 (2017).
- *Coherent Bichromatic Force Deflection of Molecules.* I. Kozyryev, L. Baum, L. Aldridge, P. Yu, E. E. Eyler, J. M. Doyle. Phys. Rev. Lett. 120, 063205 (2018).
- *1D magneto-optical trap of polyatomic molecules.* L. Baum, N. B. Vilas, C. Hallas, S. Raval. D. Mitra, and J. M. Doyle. Phys. Rev. Lett. 124, 133201 (2020).
- *Direct Laser Cooling of a Symmetric Top Molecule* D. Mitra, N. B. Vilas, C. Hallas, L. Anderegg, B. L. Augenbraun, L. Baum, C. Miller, S. Raval, J. M. Doyle arXiv:2004.02848 (2020).

1

Introduction

Laser cooling spurred a revolution in atomic, molecular and optical (AMO) physics, producing atomic samples at unprecedented temperature scales which, in combination with evaporative cooling, enabled a huge breadth of scientific investigations and technological applications [1, 2, 3, 4]. As the temperature of a quantum system decreases, our ability to trap and manipulate these systems with external electric [5], magnetic [6], and optical [7] potentials increases, allowing us to isolate these systems from ambient perturbations and engineer artificial quantum systems. The development of new tools that lower temperature and increase phase-space density extend quantum control to new and more complex systems. This is a vital and active aspect of AMO physics. Full quantum control enables the study of nuanced interactions within and between quantum systems. This exquisite level of control has been established for

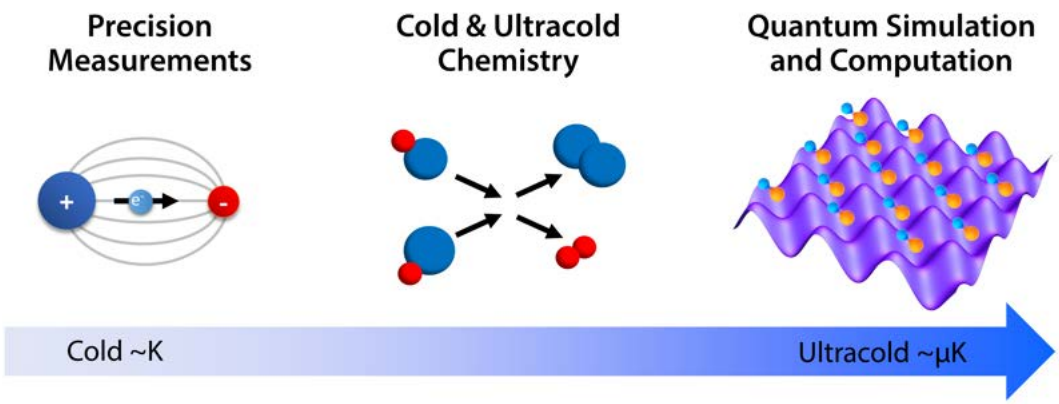

Figure 1.1: Applications of cold molecules as a function of temperature. Figure reproduced with permission from chapter 1 of ref. [14].

several atomic species, leading to applications ranging from ultra-precise atomic clocks [8] to quantum simulation of condensed matter systems [9]. Neutral atoms are well understood and provide an excellent tool for meteorology and building blocks for studying artificial quantum systems; however, molecules, rich with internal degrees of freedom, beckon with the promise of novel research avenues and advantages over atomic systems [10, 11, 12, 13].

1.1 Why cold molecules?

The internal structure of molecules gives rise to scientific applications spanning a wide range of temperature scales. Cold molecules ($\sim$2 K) are used for several types of precision measurements where their internal structure offers enhancements over atomic species [13]. Another fundamental research avenue is the study of the collisional properties in molecules to build an understanding of how energy is exchanged in molecular interactions through inelastic collisions and chemical processes. These studies have astrophysical relevance in the Kelvin regime and show the emergence of quantum behavior at lower temperatures. In the ultracold regime

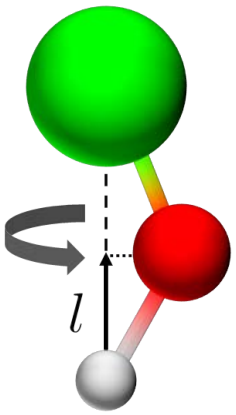

Figure 1.2: Schematic of CaOH bending mode with projection of nuclear orbital angular momentum l labeled.

($<$ 1 mK), molecules can be manipulated by optical potentials, leading to novel platforms for quantum simulation and quantum information [12, 11]. In addition to improving control over simpler molecular systems, expanding research to new and more complex species offers additional applications spanning biology and chemistry [15, 16, 17].

The work described in this dissertation focuses specifically on extending laser cooling to calcium monohydroxide (CaOH), a prototypical example of a broader class of Metal-Oxide-Radical (MOR) molecules [18]. MOR molecules feature a single metal-centered valence electron bound to a pseudohalogen ligand [19]. They are isoelectronic to alkali atoms, which were the first (and easiest) atoms to be laser cooled, and several of the diatomic species (e.g. CaF, SrF, and YO) for which laser cooling has been demonstrated [20, 21, 22, 23]. MOR molecules feature strong optical transitions and diagonal Franck Condon factors, which make them particularly well suited to laser cooling [18]. Previous studies of alkaline-earth containing species were motivated by considerable astrophysical interest in understanding the composition and energy spectrum of cool stellar objects [24, 25, 26]. The strong, accessible optical transitions and relative ease with which these samples are produced made them ideal systems

to study several types of molecular interactions (e.g. Renner-Teller interactions and Fermi resonances) yielding a sizable body of spectroscopic literature. These features of alkaline earth monohydroxides (e.g. SrOH and CaOH) make them prime candidates for laser cooling, optical manipulation, and high fidelity quantum state preparation and readout. Preliminary work in our lab on polyatomic molecules focused on SrOH as the optical transitions of that molecule were accessible with external cavity diode lasers. CaOH was chosen as a more favorable candidate for full laser cooling for two major reasons: one, the vibrational repumping transitions are in the 550-680 nm visible band where high power is accessible with dye lasers; two, the lower mass is expected to simplify radiative slowing, which is widely regarded as the largest challenge when laser cooling diatomic molecules.

Specifically, the complexity that arises in CaOH, relative to its diatomic analog CaF, is the presence of additional vibrational modes, most notably the presence of a bending vibrational mode that can possess non-zero angular momentum. In excited vibrational states with non-zero projections of vibrational angular momentum there are closely spaced opposite parity levels that can be mixed with a modest electric field. Mixing these levels polarizes the molecule, orienting it in the laboratory frame to make use of the tunable anisotropic dipole-dipole interactions that are at the heart of many quantum information and computation proposals. While this parity doublet energy structure exists in excited bending vibrational states for linear triatomics, it is a generic feature of polyatomic molecules. The dipole moment vs. electric field for CaOH in the $\widetilde{\mathrm{X}}(01^{1}0)$ state is shown in Figure 1.3. Here it is clear that not only do polyatomic molecules have states with near constant dipole moment, but they also have states without a dipole moment enabling interactions to be "switched off". More detailed descriptions of the multitude of applications for cold and ultracold diatomic and polyatomic molecules are found in the subsections below.

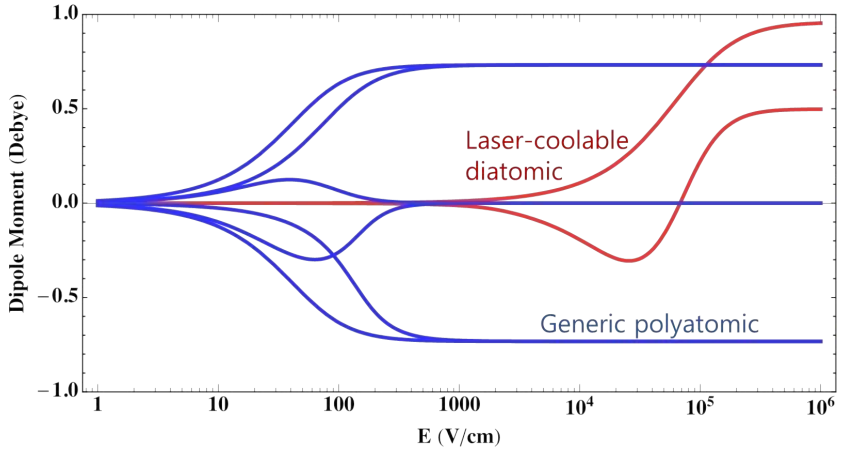

Figure 1.3: Dipole moment of CaOH plotted as a function of applied electric field. Note the existence of polyatomic states with positive dipole moment indicating molecular alignment with the applied field, negative dipole moment indicating anti-alignment, and zero dipole moment. Polarization occurs at modest and easily achievable electric fields for polyatomic molecules. While this case specifically represents CaOH in the $\widetilde{\mathrm{X}}(01^{1}0)$ state, this structure is a generic feature of polyatomic molecules. Diatomic molecules are represented by CaF and polarization occurs at significantly higher applied fields.

1.1.1 Precision measurement

Molecules are powerful tools for precision measurement, specifically tests of fundamental symmetries and the variation of fundamental constants. Diatomic molecules (ThO [27] and HF^{+} [28]) have been used as experimental probes searching for the electron electric dipole moment (EDM), and provide stringent limits on theories describing physics beyond the standard model. These molecules possess an angular momentum structure with a projection of electron orbital angular momentum along the internuclear axis, giving rise to a parity doublet that allows the molecule to be fully polarized in the lab frame. This allows the large effective internal electric field of the molecules to be leveraged [29], enhancing the sensitivity to an electron EDM. Critically, the same energy level structure provides a powerful tool for systematic error rejection. Similar experiments have been proposed in other diatomic species (YbF)

that are well suited to laser cooling. Experiments with YbF are predicted to more sensitive to an electron EDM than current limits [30]. Proposals using polyatomic species (YbOH) combine the ability to implement laser cooling with the valuable parity doublet structure and are predicted to be capable of improving EDM sensitivity by 3 orders of magnitude over current limits [31]. Since the original YbOH proposal there has been impressive progress towards the production of sub-mK samples of YbOH for a next-generation electron EDM experiment [32].

Molecules also provide a unique platform to test the time variation of fundamental constants. Such variation may be the result of couplings between ultralight dark matter fields and ordinary matter [33, 34]. The combination of energy scales in molecules ($E_{el} : E_{vib} : E_{rot} = 1 : \sqrt{\mu} : \mu$), where $\mu \equiv \frac{m_e}{mp}$ is electron to proton mass ratio, leads to near degenerate states that arise from different physical motions. The energy of rotation and vibration scales differently with μ, so monitoring the difference in energy between two such states provides a limit on the variation of μ with time. A list of transitions that have sensitivities to variation of α and μ can be found in ref. [35, 33]. Experimental limits have been set through spectroscopy of polyatomic molecular systems [36, 34] and further experiments using molecules have been proposed [37, 38]. The use of cold, trapped samples to perform precision spectroscopy will lead to significant improvements in these measurements [39, 40].

1.1.2 Cold collisions and controlled chemistry

Collisions are a fundamental physical process that is only partially understood in molecular systems [41]. Due to the natural limitations of laser cooling (the Doppler and recoil limit), secondary cooling techniques based on collisions, such as sympathetic cooling and evaporative cooling, are typically required to achieve samples with temperatures low enough to

observe quantum degeneracy[1] [13]. Sympathetic cooling of trapped molecules through collisions with a colder co-trapped atomic species have been proposed as one method for further cooling of molecules [43, 44]. *Ab initio* theoretical analysis of collisions between SrOH and Li predict favorable collisional properties for sympathetic cooling [45]. The similar electronic structure of strontium hydroxide and calcium hydroxide make it likely that these results also apply to CaOH. Evaporative cooling removes the hottest particles, allowing the sample to collisionally thermalize at lower temperatures. Evaporative cooling is ubiquitously used to cool atomic samples to quantum degeneracy. CaOH-CaOH collisions in the $\widetilde{\mathrm{X}}(01^{1}0)$ excited vibrational state have also been theoretically modeled, predicting favorable properties for evaporative cooling [46]. These predictions make use of a technique to shield molecules from short-ranged inelastic collisions and chemical loss pathways through the application of external fields [47, 48].

Cold chemistry is a rich field studying collisions in a regime where quantum properties begin to dominate [11, 49]. Single quantum state preparation of molecular samples can have dramatic effects on the collisional properties of the system [50]. Chemical reactions can be controlled through application of external fields [51, 52]. There are efforts underway to study fundamental chemical processes using single pairs of molecules, prepared in a single controllable quantum state and observing the reactants [53]. Polyatomic molecules enrich chemical studies by offering vast chemical diversity. One could also imagine generating ultracold functional groups by dissociating laser cooled MOR molecules, mirroring research efforts to produce organically relevant atomic species that are not susceptible to laser cooling [54, 55]. Additionally, the phenomenon of chirality, where two molecular isomers are mirror images of one another, can only be studied in polyatomic systems. Chirality plays a defining role in

[1] Ref. [42] is a notable exception where quantum degeneracy is achieved without evaporative cooling.

certain chemical and biological processes [56, 57].

1.1.3 Quantum information and simulation

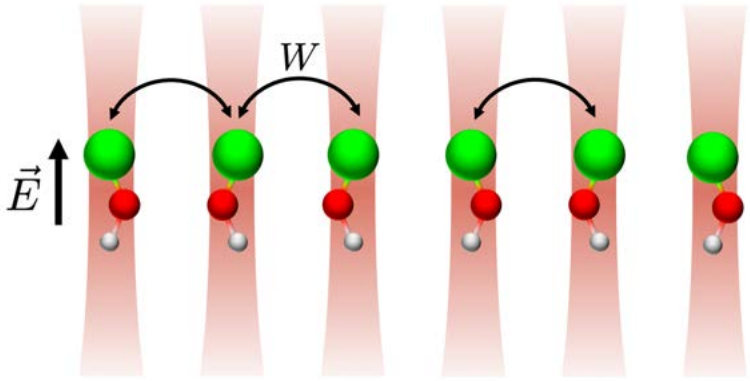

Figure 1.4: Schematic of a proposed array of optical tweezers containing CaOH molecules in the excited $\tilde{X}(01^10)$ state

Molecules have been proposed as candidates for a variety of quantum information and simulation proposals making use of long-range dipolar interactions [10, 58, 59]. In particular, $^2\Sigma^+$ ground state molecules, with an unpaired electron spin, may be used to simulate a variety of models including lattice-spin models [60], the Hubbard model with the addition of three body interactions [61], and non-trivial topological systems [62]. Polyatomic molecules, specifically symmetric tops, have also been proposed to simulate unconventional quantum magnetism [63]. In addition, molecules are excellent candidates for quantum computation, as they have long coherence times and rich internal structure that can be used to encode qubit states. There are a number of proposals using molecules to implement high fidelity gates for quantum information applications [64, 65, 66, 67, 68, 69]. Polyatomic molecules in optical tweezers, such as the recently laser cooled $CaOCH_3$ [70], have also been proposed as a scalable system for quantum computation [71]. Recently, diatomic molecules have been loaded into an optical

tweezer array where non-destructive imaging allows for rearrangement into defect-free systems [72, 73]. This represents the first stage of a powerful new quantum information platform we hope to emulate with laser cooled CaOH molecules as depicted in Figure 1.4

1.2 Producing cold molecules

The internal energy structure of molecules makes it difficult to concentrate population in a single quantum state at high temperatures. There are a variety of techniques used to generate samples of cold and ultracold molecules, broadly categorized as direct and indirect techniques. Indirect techniques construct ultracold molecules from pre-cooled atomic constituents. Direct techniques can be applied directly to a gaseous sample of molecules and generally combine a pre-cooling step (e.g. buffer gas cooling or supersonic expansion) with one of many slowing techniques in order to load a trap. This section summarizes the advantages and progress of a number of experimental technologies.

1.2.1 Indirect production of cold molecules

A variety of diatomic molecules have been created through association of previously cooled atomic samples. Initial efforts to produce ground state polar molecules were successful with KRb, using a Feshbach resonance to create weakly bound molecules that are coherently transferred to the ground state using STIRAP to achieve temperatures of $\sim$350 nK [74]. Recently this technique has yielded quantum degenerate samples of KRb molecules [75]. These techniques have also been extended to a number of other bialkai species including NaK, RbCs, NaRb and LiNa [12, 76]. An alternative approach is photoassociation [77], where two atoms are directly excited to a bound molecular state, which forms bound molecules though spontaneous decay. Spontaneous decay populates a myriad of rovibrational states, placing funda-

mental limits on the efficiency of this process. Coherent photoassociation using STIRAP techniques has been demonstrated which circumvents spontaneous decay and the resulting limit on preparation efficiency [78, 79]. Thus far, the molecules created with indirect techniques have been limited to bialkali species but theoretically these techniques can be applied generically to construct molecules from pre-cooled atomic samples.

1.2.2 Supersonic expansion

Supersonic expansion cooling is a technique that is able to produce a wide range of molecular samples with cold internal temperatures. In short, a carrier gas (typically an inert noble gas) is allowed to expand through an orifice that is significantly larger than the mean free path of the gas. Stable molecules may be introduced into the high pressure volume before the orifice, while radical species or species that do not have sufficient vapor pressure are introduced into the expansion region just outside of the orifice. Many collisions within and downstream of the nozzle impart a large velocity boost in the forward direction. This process converts random molecular motion into directed motion along the beam propagation direction. The transverse velocity and internal energy is converted into forward velocity. While this process is most efficient in monatomic gases, polyatomic molecules experience similar cooling when seeded into a carrier gas. Rotational cooling is effective, reaching temperatures of 1-10 K and vibrational cooling occurs to a significantly reduced extent, reaching temperatures of 30-100 K [80]. The typical number of collisions a molecule experiences during this process is 10^2-10^3 [81] This cooling comes at the cost of a high forward velocity which presents a challenge to some experiments. This technique has been used extensively for spectroscopic studies [82], collisional experiments with merged supersonic beams [83, 84], and has been used in combination with several of the slowing techniques discussed below to produce trapped samples of molecules.

This technique is the subject of many reviews, and for additional detail we refer the reader to a sampling of those works [85, 86].

1.2.3 Buffer gas cooling

Buffer gas cooling is a general technique that can be applied to a wide range of atoms and molecules. A hot sample is introduced into a buffer gas cell, where the translational motion is cooled through repeated elastic collisions with the buffer gas, typically inert (He or Ne). The buffer gas is maintained at low temperatures, through collisions with the cell walls held at cryogenic temperatures. For molecular samples, inelastic collisions lead to cooling of the rotational and vibration degrees of freedom, although cooling of rotation is more efficient. Molecules are translationally and rotationally thermalized with the buffer gas after 10-100 collisions [6, 87]. Molecules entrained in buffer gas exit the cell to form a beam with low forward velocities [88, 89]. At higher buffer gas flows, the efficiency of extraction increases due to hydrodynamic effects leading to molecular fluxes order of magnitude higher than other beam production techniques [90]. Several reviews of this technique are available for further details [88, 91].

Buffer gas cooling has enabled loading of magnetic traps resulting in a quantum degenerate sample of metastable He without the use of laser cooling [92]. Cryogenic buffer-gas beams (CBGBs) provide a versatile tool generating cold, bright, and slow beams of both atoms and molecules [93, 94]. CBGBs of molecules have been directly loaded into magnetic traps using optical pumping to remove kinetic energy in combination with the magnetic field [43]. CBGBs have also been used to load magneto-optical traps of lanthanide atoms without additional slowing mechanisms [95]. The low forward velocity and high brightness of CBGBs make them excellent tools for precision measurement [96] and a near ideal source for molec-

ular laser cooling experiments. The development of the buffer gas source for CaOH will be discussed later in this work.

1.2.4 Slowing techniques

There are a variety of slowing techniques that use a combination of applied electromagnetic fields to bring molecular beams to lower velocities where they can be loaded into traps for further study. These slowing techniques have been used to load a variety of traps allowing study of molecules in conservative magnetic [97, 98, 99, 100, 101], electric [5, 102, 103, 104] and optical [72] potentials. It should be noted that several trapping strategies have allowed further cooling of the trapped sample including evaporate cooling in a magnetic trap [105], laser cooling in magneto-optical traps [21, 106, 107, 108] and optical dipole traps [109] as well as optoelectric-sisyphus cooling in electrostatic traps [110, 111, 112].

Zeeman and Stark decelerators are commonly employed in combination with supersonic beam sources. These techniques apply magnetic (Zeeman) or electric (Stark) fields to generate a potential hill. Molecules lose kinetic energy climbing this potential hill. The fields are switched off diabatically, removing energy from the beam. This process is repeated many times, typically with guiding or focusing stages interspersed between slowing stages. These techniques have been successful in decelerating large number of atomic and molecular species and we refer the reader to several reviews of this technology [113, 114, 115]. A variant of Stark deceleration, optical stark deceleration [116], uses high power laser light to produce the potential hills used to remove kinetic energy. A variant of Zeeman decelerators is a moving magnetic trap [117], where samples are trapped in the moving frame and gradually decelerated to rest. This technique has the advantage that samples are transversely confined throughout the slowing process reducing losses due to plumbing. Similar in concept to a moving mag-

netic trap, mechanical deceleration has been applied to molecules by the centrifugal motion of the potential created by an electrostatic guide [118]. This technique takes advantage of the slower velocity distribution of a buffer gas beam source has been used to decelerate a several polyatomic species [119].

Alternative approaches combine the use of laser light with external fields. Originally implemented to load deep magnetic traps, Optical Loading employs two optical pumping steps that allows low field seeking (LFS) particles to climb a magnetic potential before being optically pumping into a high field seeking (HFS) state [43]. HFS particles continue to climb the magnetic potential as they approach the trap center before they are optically pumping into trapped (LFS) states . This technique only requires scattering two photons and is applicable to wide range of molecular species. This technique can be extended from one to multiple stages in the proposed Zeeman-Sisyphus slowing scheme, where the additional length requires guiding elements to mitigate transverse loss [120]. Additionally, a Zeeman slower for molecules has been proposed that combines the powerful effect of cooling with deceleration to increase the number of trappable molecules at the cost additional repumping requirements [121].

To date, molecular laser cooling experiments have used radiation pressure to slow molecules to the capture velocity of a molecular MOT. Initial slowing of diatomic molecules used white-light slowing techniques [122, 123], where an overdriven electro-optical modulator (EOM) adds a series of sidebands to broaden the laser light to continuously address molecules as the Doppler shift changes due to deceleration. Chirped slowing is another purely radiative technique where frequency of the slowing laser is swept at a rate matching the deceleration to continuously address molecules. This technique provides two advantages over whitelight slowing: 1, it compresses the velocity distribution as fast molecules pile up in lower velocity classes; 2, it allows all available laser power to be used to address a single velocity class, increasing the maximum deceleration. Several diatomic laser cooling experiments rely on

chirped slowing[124, 125].

1.3 Thesis overview

This thesis will discuss our approach to the creation of ultracold polyatomic molecules by utilizing the unique skillset of the Doyle group combining a background in buffer-gas cooling, the expertise resulting from laser cooling of CaF, and experience gained through pioneering demonstrations of laser cooling and coherent control of triatomic radical SrOH. This thesis focuses on the experimental efforts to produce, manipulate, cool, and trap the polyatomic radical calcium monohydroxide (CaOH). Chapter 2 will provide an overview of relevant molecular structure. Chapter 3 will review design consideration of the cryogenic molecular source. Chapter 4 will discuss the production of CaOH and the efforts that were taken to enhance production and lower beam velocity. Chapter 5 will discuss laser manipulation of CaOH molecules and how we establish a quasi-closed cycling transition. Chapter 6 will detail our investigation of unexpected loss in the system and its resolution. Chapter 7 will detail the first demonstration of magneto-optical forces in a polyatomic system. Chapter 8 will discuss the outlook and the next steps toward an sub-mK sample of CaOH molecules.

2

CaOH Molecular Structure

Structure plays an integral role in determining which experimental techniques are best suited to exert control over a molecule. An initial proposal by Di Rosa [126] outlined three criteria that enable direct laser cooling of molecules: one, the existence of strong electronic transitions; two, diagonal Franck-Condon factors (FCFs); three, the absence of interfering metastable states. By understanding how molecular structure gives rise to these characteristics, we can identify molecules that are suitable for laser cooling with promising qualities for use in science and engineering (see previous chapter). The alkaline earth monohalide diatomic molecules (e.g. CaF [22], SrF [20], BaF [127], and RaF [128]) are a class of diatomic molecules that have been identified as suitable for laser cooling. The electron wavefunction of these molecules is centered on the metal atom and projects away from chemical bond. This is

caused by hybridization of *s* and *pσ* orbitals that compose the ground state electronic orbital in diatomic and linear triatomic molecules as shown in Figure 2.1 [129]. This allows the electron to be electrically excited while minimally perturbing the chemical bond potential, which ultimately leads to diagonal FCFs.

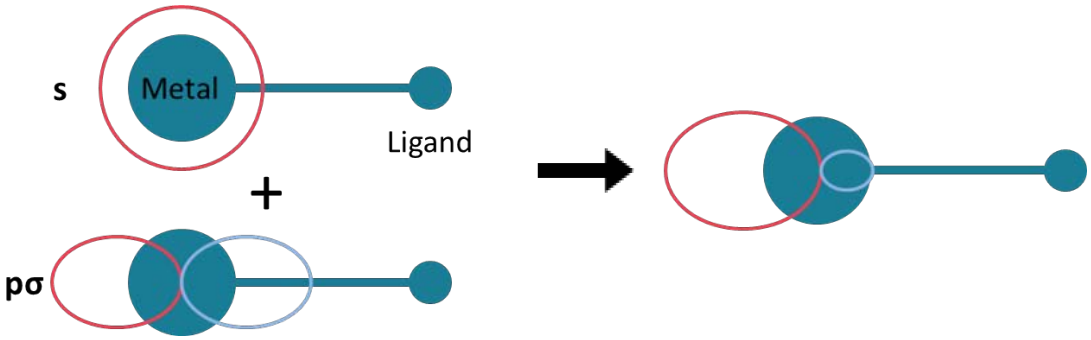

Figure 2.1: Simplified diagram illustrating the hybridization of *s* and *pσ* orbitals leading to a polarized unpaired electron distribution that is localized on the metal atom.

Similar molecular properties are seen in polyatomic molecules where the halogen (often fluorine) is substituted with a pseudohalogen, a functional group with chemical properties similar to halogen elements [130]. The simplest example of a pseudohalogen is a hydroxyl group (OH). The structural similarity between CaF and CaOH is a testament to the power of this approach. We have proposed further extensions to this idea by identifying a broad class of molecules dubbed "MOR" molecules where a metal (M) is bound to an interchangeable ligand (R) using oxygen (O) as an intermediary. MOR molecules contain examples of symmetric and asymmetric tops as well as chiral species [18]. While CaOH is similar to diatomic molecules like CaF, the addition of a single atom introduces new vibrational degrees of freedom with the concomitant increase in complexity. This chapter will describe the structure of linear triatomic molecules and how to construct a photon cycling scheme to enable laser cooling and control of CaOH.

2.1 The Born-Oppenheimer approximation

A quantum mechanical description of molecular structure begins with the time-independent Schrödinger equation [131]:

$$\widehat{\mathrm{H}}_{Mol}\,\Psi_{Mol} = E\,\Psi_{Mol} \tag{2.1}$$

The molecular Hamiltonian ($\widehat{\mathrm{H}}_{Mol}$) describes how the K nuclei interact with the N electrons via the Coulomb interaction[1] in a molecular state with energy E. The terms in the Hamiltonian can be grouped to highlight various interactions as follows:

$$\widehat{\mathrm{H}}_{Mol} = \widehat{\mathrm{T}}_N + \widehat{\mathrm{T}}_e + \widehat{\mathrm{V}}_{N,N} + \widehat{\mathrm{V}}_{e,e} + \widehat{\mathrm{V}}_{N,e} \tag{2.2}$$

These terms represent the nuclear kinetic energy, electronic kinetic energy, the nuclear-nuclear repulsion, the electron-electron repulsion, and the nuclear-election attraction respectively [132].

The Born-Oppenheimer approximation [133] is invoked to simplify this expression. The Born-Oppenheimer approximation states, the magnitude of the Coloumb force is equal on the nuclei and the electrons, but the electrons have significantly lower mass. As a result, the low-mass electron cloud is assumed to adiabatically follow the potential defined by the position of the heavy nuclei. In the Born-Oppenheimer approximation the nuclear motion (vibration and rotation) is separated from the electronic motion and the wavefunction describing the molecule is approximated to be:

[1] Here we ignore all interactions relating to electronic or nuclear spins as the energy shifts due to these interactions are small. These contributions will treated as perturbations of the Schrödinger equation.

$$|\Psi_{Mol}\rangle = |\psi_{el}\rangle\,|\chi_N\rangle \tag{2.3}$$

Leading to a description of molecular energy consisting of the sum of the electronic potential and the nuclear energy:

$$E_{Mol} = U_{el} + E_N \tag{2.4}$$

Similarly, the nuclear energy consisting of both vibration and rotation is often separated, in an approximation that is conceptually similar to but formally distinct from the Born-Oppenheimer approximation. This gives rise to a simplified Hamiltonian that allows us to consider the contributions from the electronic, vibrational, and rotational degrees of freedom independently.

$$\widehat{\mathrm{H}}_{Mol} = \widehat{\mathrm{H}}_{el} + \widehat{\mathrm{H}}_{vib} + \widehat{\mathrm{H}}_{rot} \tag{2.5}$$

Corrective terms can be added to this Hamiltonian to provide a more complete description of the system [134]. In the course of our work with CaOH, there are several instances where we observed a breakdown of the Born-Oppenheimer approximation, meaning we see direct coupling between the electronic degree of freedom and the vibrational degree of freedom. These instances are described in detail in Section 6.2.1.

2.2 Electronic structure of CaOH

Even after separating the electronic Hamiltonian from the rotational and vibrational contributions, it remains difficult to accurately solve the Schrödinger equation for molecules from first principles. An approach that has been successful to derive electronic energies in alkaline earth containing molecules is ligand field theory. This method was implemented on calcium mono-

halides by Rice, Martin, and Field [19] and later generalized to other alkaline earth monohalines [135]. While ligand field theory is a quantitative technique, the existence of a large body of spectroscopic work on CaOH has allowed us to rely on experimental measurements and spectroscopic constants rather than the quantitative results of ligand field theory for predictions when performing spectroscopy. Nevertheless, for completeness, a short description of ligand field theory is provided here.

Ligand field theory stipulates that the electronic structure and properties of an alkaline earth containing species can be derived by perturbing the electronic structure of the alkaline earth ion (Ca+) by the appropriate negatively charged ligand (OH^-). Mathematically this is represented by the following expression:

$$\widehat{\mathrm{H}} = \widehat{\mathrm{H}}_{Ca^+} + \widehat{\mathrm{H}}_{LF} \tag{2.6}$$

where $\widehat{\mathrm{H}}_{Ca^+}$ describes the energy of the free calcium ion and $\widehat{\mathrm{H}}_{LF}$ describes the interaction of the valence electron of the Ca^+ ion with the negatively charged ligand. The ligand is treated as a point charge fixed at a given internuclear separation.

This perturbation manipulates the energy levels in three ways. First, it rearranges the energy levels of the atomic ion orbitals. Second, it splits the atomic orbitals into the m_L components. Finally, it allows orbitals of the same m_L to mix. This third effect generally has the greatest impact on the Hamiltonian of a given molecular state, as molecular state may be comprised of a mixture of multiple atomic orbitals. Chapter 2 of ref. [136] contains additional information on ligand field theory including a graphical representation of how the ionic orbitals evolve into the electronic states for molecules with $C_{\infty V}$ symmetry, such as CaOH. Chapter 8 of ref. [136] contains a correlation diagram showing how the energy levels of CaOH arise from the diatomic analog CaF.

2.3 Vibrational structure of linear polyatomic molecules

Linear polyatomic molecules comprised of a number of atoms (N) have 3N-5 vibrational degrees of freedom[2] [131]. The vibrational modes in CaOH are labeled with four quantum numbers $(v_1, v_2^{|l|}, v_3)$, where v_1, v_2, and v_3 indicate the number of quanta in the symmetric stretching mode, the bending mode, and the antisymmetric stretching mode, respectively. l labels the nuclear orbital angular momentum in the bending mode and takes values of $l = -v_2, -v_2+2, ..., v_2$ [137]. Each of these modes is approximated as a harmonic oscillator with an total energy given by $G(v_1, v_2, v_3)$:

$$G(v_1, v_2, v_3) = \sum_i \omega_i (v_i + d_i/2) \tag{2.7}$$

where d_i is the degeneracy and ω_i is the vibrational frequency of the i^{th} vibrational mode. However, a more complete description of the vibrational potential allows cross coupling between vibrational modes as well as anharmonic terms. The vibrational energy levels of polyatomic molecules are expressed as a series expansion [137]:

$$G(v_1, v_2, l, v_3) = \sum_i \omega_i (v_i + \frac{d_i}{2}) + \sum_i \sum_{k \geq i} x_{ik} (v_i + \frac{d_i}{2})(v_k + \frac{d_k}{2}) + g_{22} l^2 + \dots \tag{2.8}$$

where x_{ik} and g_{22} are anharmonicity constants. It should be noted that the above treatment is highly approximate for many molecules and there are a number of coupling mechanism that may perturb the energy levels of a given system. For an exhaustive treatment of these

[2] Nonlinear molecules posses 3N-6 vibrational degrees of freedom, this can be intuitively understood as the chemical bonding of a nonlinear molecules breaks the degeneracy of the bending vibration removing a vibrational degree of freedom but generates an additional rotational moment of inertial and so splits a degenerate rotation axis into two rotational degrees of freedom.

mechanisms please consult references [137, 131, 136, 134]

2.4 Rotational structure

The rotational structure of CaOH is approximated by a rigid rotor description [138], where solving the Schrödinger equation results in:

$$E_J = BJ(J+1) \tag{2.9}$$

Here B is the rotational constant that is defined as:

$$B = \frac{h}{8\pi^2 c I_{B_e}} \tag{2.10}$$

where I_{B_e} is the equilibrium moment of inertia. This description works well for many applications but an additional term is needed to account for the centrifugal stretching of the molecular bond as it rotates. This leads to the expression [139]:

$$E_J = BJ(J+1) - D[J(J+1)]^2 \tag{2.11}$$

D can be neglected for many spectroscopic applications, but the contribution become significant at high values of J.

2.4.1 Angular momenta in CaOH

The angular momentum quantum numbers that best describe the system are the sum of many different angular momenta. These angular momenta may couple to each other due to different physical mechanisms, influencing which quantum numbers are used to conveniently de-

scribe a system. The limiting cases of how the angular momenta are coupled are described by Hund's cases which identify which quantum numbers are most convenient [139]. For CaOH, the molecule is well described by either Hund's case (a) or Hund's case (b), pictured in Figure 2.2. In CaOH, the electronic states with no electronic orbital angular momentum ($\widetilde{\mathrm{X}}$, $\widetilde{\mathrm{B}}$, and $\widetilde{\mathrm{D}}$ are best described by Hund's case (b) with the quantum numbers $|\Lambda,\ N,\ S,\ J\rangle$, while the $\widetilde{\mathrm{A}}$ state is best described by Hund's case (a) with the quantum numbers $|\Lambda,\ S,\ \Sigma,\ J,\ \Omega\rangle$.

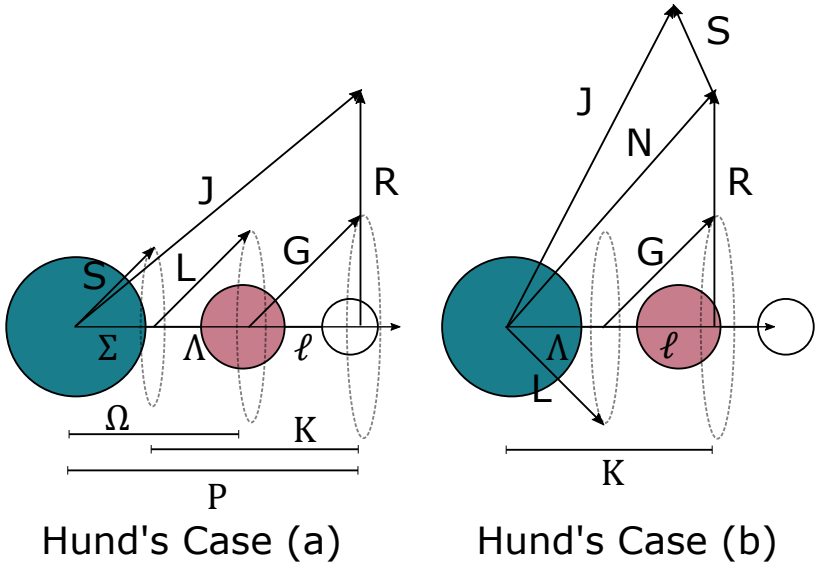

Figure 2.2: (left) Coupling of angular momenta for a linear polyatomic molecules in Hund's case (a) (e.g. the $\widetilde{\mathrm{A}}$ state of CaOH). (right) Coupling of angular momenta for a linear polyatomic molecules in Hund's case (b) (e.g. the $\widetilde{\mathrm{X}}$, $\widetilde{\mathrm{B}}$, and $\widetilde{\mathrm{D}}$ states of CaOH).

Hund's case (a)

Hund's case (a) describes the case where the angular momenta are coupled as defined by the hierarchy of coupling strengths electrostatic $>$ spin-orbit $>$ rotational. **L** is strongly coupled to the internuclear axis by the electrostatic Hamiltonian. This reflects that the chemical bond is the dominant energy scale in the system. The projection of L onto the internuclear axis is

called Λ. Next, the spin-orbit interaction couples **S** to **L**. The projection of of **S** onto the internuclear axis is called Σ. The sum of the projection of Σ and Λ, called Ω, is coupled to the angular momentum of rotation **R** resulting in **J**.

Hund's case (b)

Hund's case (b) describes the case where the angular momenta are coupled as defined by the hierarchy of coupling strengths electrostatic > rotational > spin-orbit. Again **L** is strongly coupled to the internuclear axis by the electrostatic Hamiltonian, with a projection called Λ. Due to a weak or non-existent (**L**=0) spin-orbit interaction S is not coupled to the internuclear axis, and Ω is not defined. The rotational Hamiltonian term couples Λ to the rotational angular momentum (**R**) of the molecule resulting in **N** = **R** + **K**. Physically, this coupling may be thought of as the effect of the magnetic field generated by the rotating molecule [140]. Finally, the spin-rotation interaction couples **S** to **N** resulting in **J** = **N** + **S**.

Table 2.1: Angular Momentum in CaOH

Quantum Number Describing	Symbol
Vibration	v
Vibrational Angular Momentum	**G**
Rotational Angular Momentum	**R**
Electronic Orbital Angular Momentum	**L**
Total Angular Momentum	**J**
Electron Spin	**S**
Nuclear Spin	**I**

Quantum Number	Hunds Case (a)	Hunds Case (b)
Total Angular Momentum (T.A.M.)	$\mathbf{J} = \mathbf{L} + \mathbf{S} + \mathbf{R}$	$\mathbf{J} = \mathbf{N} + \mathbf{S}$
T.A.M. without Electron Spin	n/a	$\mathbf{N} = \mathbf{L} + \mathbf{G} + \mathbf{R}$
T.A.M. with Nuclear Spin	$\mathbf{F} = \mathbf{J} + \mathbf{I}$	
Projection of **L** on internuclear axis	Λ	
Projection of **S** on internuclear axis	Σ	
Projection of **G** on internuclear axis	l	
K =	$\Lambda + l$	
P =	$\Lambda + l + \Sigma$	
Ω =	$\Lambda + \Sigma$	n/a

2.4.2 Energy levels of CaOH

An expression for the energy levels of a linear polyatomic molecules in Hund's Case (b) and **G**=0 is given by [141]:

$$F_1(N) = T_v + B''_v N(N+1) - D''_v N^2(N+1)^2 + \gamma_v/2N \tag{2.12}$$

$$F_2(N) = T_v + B''_v N(N+1) - D''_v N^2(N+1)^2 - \gamma_v/2(N+1) \tag{2.13}$$

where T_v is the vibronic term value, the subscript on the F refers to the upper and lower spin-rotation component for each rotational level, and γ_v is the spin rotation constant. Similar expressions are available for molecules in Hund's case (a) states like the $\widetilde{\mathrm{A}}$ state of CaOH. The $^2\Pi_{1/2}$ manifold is described by:

$$F_{1c}(J) = T_v - A_v/2 + B'_{v1/2} J(J+1) - D'_{v1/2} J^2(J+1)^2 - p_v/2(J+1/2) \tag{2.14}$$

$$F_{1d}(J) = T_v - A_v/2 + B'_{v1/2} J(J+1) - D'_{v1/2} J^2(J+1)^2 + p_v/2(J+1/2) \tag{2.15}$$

where p_v is a Λ doubling parameter and A_v is the spin-orbit interaction. The $^2\Pi_{3/2}$ manifold is described by

$$F_{2c}(J) \approx F_{2d}(J) \approx T_v + A_v/2 + B'_{v3/2} J(J+1) - D'_{v3/2} J^2(J+1)^2 \tag{2.16}$$

for this expression the Λ doubling parameter is neglected as it was unresolved. It should also be noted that all hyperfine interactions are neglected in these expressions as the hyperfine splitting is unresolved due to the natural linewidth of the optical transitions [142].

These energy expressions hold for excited stretching vibrational modes, with slight modification of the molecular constants[3]. In excited bending vibrational levels, the angular momentum of bending vibrations must be taken into account modifying the energy expression to [144]

$$F_1(N) = T_v + B''_v(N(N+1) - l^2) - D''_v(N(N+1) - l^2)^2 + \frac{\gamma_v}{2}N \pm q_v/2N(N+1) \quad (2.17)$$

$$F_2(N) = T_v + B''_v(N(N+1) - l^2) - D''_v(N(N+1) - l^2)^2 - \frac{\gamma_v}{2}(N+1) \mp q_v/2N(N+1) \quad (2.18)$$

Here F_1 and F_2 are the upper and lower spin-rotation components and the upper/lower sign refers to the e/f parity of the state. For states with vibrational angular momentum **G**, $\mathbf{N} \geq \mathbf{G}$. It should be noted that this expression, while adequate for spectroscopy, has been simplified in the high N limit. A more complete description of the spin-rotation interaction in states with vibrational orbital angular momentum is available in ref. [145] which results in a correction to the spin rotation terms.

Electronic transitions in molecules are labeled to describe the changes in quantum numbers between excited and ground states as

$$^{\Delta N}\Delta J_{F'_i F''_j} \quad (2.19)$$

where ΔN, and ΔJ is specified with the shorthand P, Q, and R for -1, 0, and +1 respectively.

[3] e.g. $B_v = B_e - \sum_i \alpha_i(v_i + \frac{d_i}{2})$ [143]

2.5 Parity

One feature of interest for a variety of scientific endeavors is the presence of closely spaced parity doublets. In diatomic molecules, without orbital angular momentum, parity doublets arise from adjacent rotational states where the parity of the system behaves as $(-1)^J$. Certain angular momentum structures cause opposite parity states within the same rotational level. Λ-type doubling is a common example of parity doublet structure as described in ref. [132]. In CaOH *l*-type doubling, described below, provides a near degenerate parity doublet.

There are two common notations for parity used in the literature: the total parity notation (+/-), and the rotationless parity notation (e/f). The rotationless notation labels the parity of the ro-vibronic wavefunction with the J-dependence removed. To convert from (e/f) to (+/-) the following relationship is used [132]:

$$\begin{array}{cc} \text{e} & \text{f} \\ (+)\,(-1)^J & (-)\,(-1)^J \end{array}$$
for integer J

$$(+)\,(-1)^{J-\frac{1}{2}} \qquad (-)\,(-1)^{J-\frac{1}{2}}$$
for half-integer J

This notation is important for identifying parity selection rules when designing a photon cycling scheme that prevents rotational branching. The dipole transition selection rule (+ $\longleftrightarrow$ -) becomes (e $\longleftrightarrow$ e) and (f $\longleftrightarrow$ f) for P and R ($\Delta J = |1|$) branches and (f $\longleftrightarrow$ e) for Q ($\Delta J = 0$) branches [132].

2.5.1 *l*-type doubling

In linear triatomic species, the projection of vibrational angular momentum onto the internuclear axis, *l*, can take on differently signed values. For example in the (01^10) state, $l = \pm 1$

with the sign of l corresponding to the orientation of the angular momentum projection. These two states are nearly degenerate, with a small splitting caused by a Coriolis interaction with the molecular rotation [137]. The projection l switches sign under the parity operator, therefore odd and even superpositions of the l states form parity eigenstates. The splitting of these parity eigenstates in the first excited bending mode of CaOH is $\sim$40 MHz [146].

2.5.2 Laser cooling scheme for CaOH

In order to apply optical forces and other laser cooling techniques to atoms, it is necessary to scatter many photon before an atom is lost to a state that is not addressed by the laser light. These states are known as "dark states". In atomic species, it is straightforward to find a combination of selection rules that limit spontaneous decay to the original ground state establishing a "cycling transition". In order to create a cycling transition in molecules we must consider how to avoid loss channels that arise from all degrees of freedom. The electronic and rotational degrees of freedom are governed by selection rules; however, vibrational decay is not governed by rigorous selection rules. Vibrational decay is governed by wavefunction overlap, quantified by Franck-Condon factors defined in this section.

In order to close the electronic degree of freedom one must ensure that there is no significant branching to long lived metastable electronic states. This can be accomplished if the laser cooling transition is chosen between the ground state and the lowest lying excited state or by relying on angular momentum selection rules to prevent $\Delta L > 1$[4] decay. Using the lowest lying electronic state is not a requirement and large optical forces have been applied in CaF and SrOH using the $\widetilde{\mathrm{X}} - \widetilde{\mathrm{B}}$ transition [123, 148].

Closing the rotational degree of freedom exploits a combination of parity (+ $\longleftrightarrow$ -) and ΔN

[4] we neglect electronic quadrupole and magnetic dipole transitions as they are sufficiently suppressed [147, 14]

=0,±1 selection rules. As originally proposed in ref. [149], the P(N=1) branch of the first rotationally excited state is used to minimize the number of lasers required to close the rotational degree of freedom. This is schematically depicted in Figure 2.3

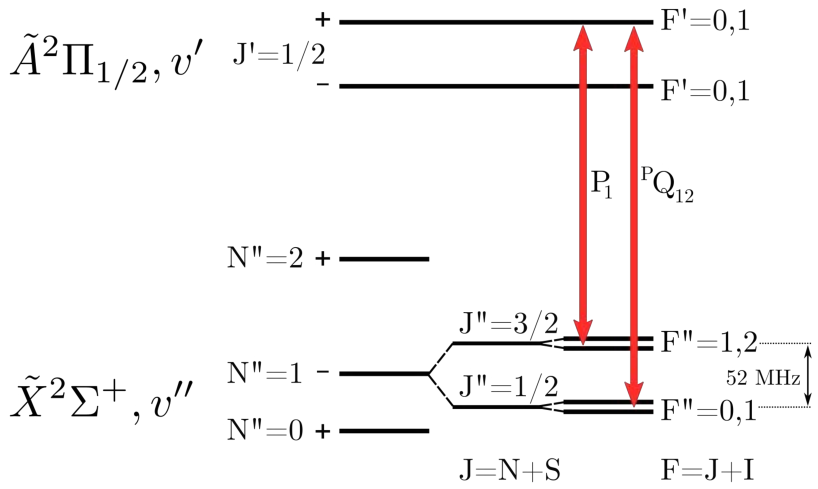

Figure 2.3: Rotational structure of CaOH illustrating the $\widetilde{X}^2\Sigma^+(v_1''v_2''v_3'') \rightarrow \widetilde{A}^2\Pi_{1/2}(v_1'v_2'v_3')$ $P_1(J'' = \frac{3}{2})$ and ${}^PQ_{12}(J'' = \frac{1}{2})$ rotationally closed transitions are shown [126]. The parity of the ground states is indicated by the sign to the right of the N'' value while the parity of the excited states is indicated to the right of the J' value. The level diagrams are not to scale.

The primary complication in establishing a closed cycling transition of molecules is vibrational decay. This is compounded in polyatomic species where the additional atomic constituents increase the number of vibrational modes . Vibrational selection rules are limited to vibrational states with vibrational angular momentum. In general, vibrational decay is simply described by wavefunction overlap, the projection the vibrational wavefunction from the excited state onto the basis formed by the vibrational wavefunctions of the ground state. The intensity of a transitions is proportional to the square of the transition moment integral:

$$I_{e'v'e''v''} = |\langle \psi_{e'}, \psi_{v'} | \boldsymbol{\mu} | \psi_{e''}, \psi_{v''} \rangle|^2 \tag{2.20}$$

For symmetric vibration, there is no selection rule on Δv. For bending mode transitions, the Born Oppenheimer approximation separates vibrational angular momentum from electronic angular momentum leading to a $\Delta l = 0$ selection rule. This approximation breaks down as described in Section 6.2.1. The separation of the electronic and vibrational wavefunctions simplifies the transition intensity expression to :

$$I_{e'v'e''v''} = \langle \psi_{e'} | \boldsymbol{\mu} | \psi_{e''} \rangle^2 \langle \psi_{v'} | \psi_{v''} \rangle^2 \tag{2.21}$$

$$I_{e'v'e''v''} = |R_e|^2 q_{v'-v''} \tag{2.22}$$

Where $|R_e|$ is the electronic transition dipole moment and $q_{v'-v''}$ is the Franck-Condon factor.

$$q_{v'-v''} = | \langle \psi_{v'} | \psi_{v''} \rangle |^2 \tag{2.23}$$

Molecules with diagonal Franck-Condon factors limit the number of states populated by spontaneous emission. In order to recover lost population a vibrational repumping laser is employed to optically pump molecules back into the ground vibrational state to continue cycling photons. The Franck-Condon factors of CaOH have been measured in previous experiments [150] and in this thesis (see Chapter 6). The laser cooling scheme presented in Figure 2.4 will allow for scattering an average of 2200^{+400}_{-300} photons per molecules with 6 lasers of different wavelengths.

2.6 CaOH molecular constants

The following tables have been aggregated from a number of spectroscopic references for ease of use. All constants unless otherwise noted are in units of (cm^{-1}). Values in parenthesis are one standard error in units of the last digit of the corresponding constant. Values in square

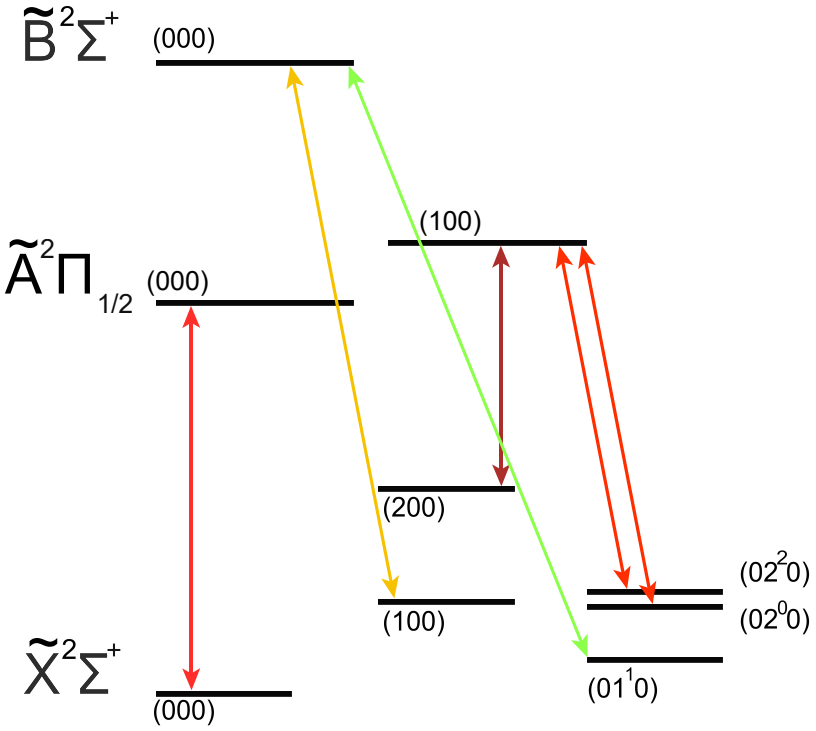

Figure 2.4: Laser cooling scheme for CaOH.

brackets were held as constant during the spectroscopic fit.

Table 2.2: Molecular Parameters for CaOH in the $\tilde{X}^2\Sigma^+$ and $\tilde{A}^2\Pi$ states [151, 152, 153, 154]

	$\tilde{X}^2\Sigma^+$	$\tilde{A}^2\Pi$
v_1	614.79	628.4821(15)
G^0_{020}	682.90	
ω^0_2	349.34	358.652(3)
x^0_{22}	-3.95	-3.892(3)
$\varepsilon\omega_2$		-35.6652(19)
ε		-0.0973
$\hat{g}_4$		-0.0997(3)
k_{122}		2.027×10^{75}
φ_{122}		29.2035(14)
α_2	0.001089(6)	0.001167(9)
γ_{22}	0.000111(3)	0.000087(5)
γ_{ll}	-0.000121(3)	-0.000078(4)
ω_1	614.79	614.79
ω_2	357.23	366.435
ω_3	3738[a]	3738[a]
B_e	0.3366106	0.3436560
α_1	0.002200(10)	0.0023153(70)
α_2	0.001089(6)	0.001167(9)
α_3	0.000397[b]	0.000397[b]
ζ_{21}	0.1428	0.1603
ζ_{23}	0.9898	0.9871
$r_e(Ca-O)$	1.9746 Å	1.9532 Å
$r_e(O-H)$	0.9562 Å	0.908 Å
f_{11}	2.669 mdyn/Å	2.849 mdyn/Å
f_{13}	0.463 mdyn/Å	0.908 mdyn/Å
f_{33}	7.850 mdyn/Å	7.894 mdyn/Å
f_{22}	0.0611 mdyn · Å	0.0640 mdyn · Å
f_{122}	-0.165 mdyn	-0.167 mdyn
f_{322}	0.136 mdyn	0.227 mdyn

[a] Estimated based on ref [151]
[b] Estimated based on ref [152]

Table 2.3: Molecular Constants (cm^{-1}) for the $\widetilde{X}$ vibrational states of CaOH [154, 153].

	$\tilde{X}^2\Sigma^+(000)$	$\tilde{X}^2\Sigma^+(100)$	$\tilde{X}^2\Sigma^+(200)$	$\tilde{X}^2\Sigma^+(300)$	$\tilde{X}^2\Sigma^+(400)$
T_v	0.0	609.015(10)	1210.150(8)	1803.054(15)	2387.272(77)
B_v	0.33433411(1)	0.33219(3)	0.32995(2)	0.32772(4)	0.32579(20)
D_v	$0.38600(3)\times10^{-6}$				
γ_v	$0.115946(23)\times10^{-2}$	0.111×10^{-2}			

	$\tilde{X}(010)\ ^2\Pi$	$\tilde{X}(020)\ ^2\Sigma$	$\tilde{X}(020)\ ^2\Delta$
T_v	352.9259(9)	688.67(1)	713.040(9)
B_v	0.3334580(16)	0.333047(4)	0.332562(11)
D_v	$0.2943(16)\times10^{-6}$	$0.415(2)\times10^{-6}$	$0.466(6)\times10^{-6}$
γ_v	$0.1184(11)\times10^{-2}$	0.1184×10^{-2}	0.111×10^{-2}
q_v	$-0.7181(2)\times10^{-3}$		
g_{22}		6.0869(12)	6.0869(12)

Table 2.4: Molecular Constants (cm^{-1}) for the $\widetilde{B}$ vibrational states of CaOH.

	$\tilde{B}^2\Sigma^+(000)$ [155]	$\tilde{B}^2\Sigma^+(100)$ [156]
T_v	18022.268(1)	18629.699[1]
B_v	0.339409(10)	0.33219(3)
D_v	$3.707(100)\times10^{-7}$	$5.16(23)\times10^{-7}$
γ_v	-0.043615(46)	-0.043624(83)

[1] Extracted from measured transitions Appendix D.

Table 2.5: Molecular Constants (cm^{-1}) for the $\widetilde{A}$ vibrational states of CaOH [153].

	$\tilde{A}^2\Pi(000)$	$\tilde{A}^2\Pi(100)$	$\tilde{A}(010)$	$\tilde{A}(020)$
T_v	15998.1220(7)	166263.917(1)	16360.3890(4)	16700.172(2)
A_v	66.8181(12)	67.159(3)	67.0951(7)	[67.0951]
B_v	0.3412200(23)	0.3389047(41)	0.3402609(16) ($^2\Delta$)	.3395830(48) (02^00)
			0.3402123(9) ($^2\Sigma$)	.3392718(68) (02^20)
D_v	$0.3891(11)\times10^{-6}$	$0.3780(17)\times10^{-6}$	$0.3976(5)\times10^{-6}$ ($^2\Delta$)	$0.4186(17)\times10^{-6}$
			$0.3990(5)\times10^{-6}$ ($^2\Sigma$)	
p^e	-0.04287(9)	-0.04405(7)	-0.04472(8)	-0.04547(9)
q^e	$-0.3257(74)\times10^{-3}$	$-0.4178(58)\times10^{-3}$	$-0.3072(84)\times10^{-3}$	$-0.5423(38)\times10^{-3}$
γ_v	0.0304	[0.0304]	0.2617(5)	[0.02617]
A_Dv	0.135×10^{-3}	$0.368(7)\times10^{-3}$	$0.1232(7)\times10^{-3}$ ($^2\Delta$)	$-1.38(2)\times10^{-3}$
			$0.140(2)\times10^{-2}$ ($^2\Sigma$)	
A_H			$-0.140(3)\times10^{-6}$	
γ_D			$-.119(2)\times10^{-4}$	$1.098(15)\times10^{-5}$
$\varepsilon\omega_2$			-36.2634(6)	-36.5624(7)
$\varepsilon_D\omega_2$			$0.741(8)\times10^{-3}$	$-0.172(4)\times10^{-3}$
W_1		10.3250 (5)		10.3250 (5)
q^v			$-0.6978(17)\times10^{-3}$	$-0.7356(9)\times10^{-5}$
g_K			0.5937(5)	[0.5937]
g_{22}				7.1939(10)

3

Cryogenic Source Design

The buffer gas beam source used in this work produces a cold, slow beam of molecules, which for the reasons described in Chapter 1 is critical for direct laser cooling experiments. The primary drawback of buffer gas sources is the cost and complexity involved with cryogenic equipment. This chapter outlines the concerns that arise when designing of a cryogenic system with the goal of serving as a practical guide making buffer gas sources more accessible to individuals without prior cryogenic experience.

CaOH was first studied in Broida oven sources at temperatures of 500-700 Kelvin [141, 153, 136]. The relatively high temperature of these sources were not able to resolve rotational states and later spectroscopic work relied on supersonic expansion to generate internally cold samples [157, 143, 158, 153]. While supersonic expansion is sufficient for spectroscopy, it

produces a fast moving beam of molecules that would hinder slowing and trapping efforts.

The photon cycling scheme used in CaOH requires molecules to be in the N=1 rotational state and the low velocity is required for effective slowing given the limited photon scattering rates in molecules that are low compared to atoms. Following successful diatomic laser cooling experiments we use a cryogenic buffer-gas beam source. Given the boxy form factor of the equipment, it is colloquially referred to as the "beam box". This chapter will cover the design considerations and operation of our source which is designed around the Cryomech PT415 1 K Cryostat, which we refer to as the 1 K system. As this system was the first model with integrated recirculating helium system employed in our lab, substantial efforts were made to debug and stabilize the system. These efforts are detailed in Appendix C. Additionally, cryogenic engineering reference and directions for fabricating common beam box components are presented in Appendix B.

3.1 Heat transfer and cooling

Fundamental to the operation of a buffer gas source is the ability to maintain the buffer gas cell at temperatures of a few Kelvin. To optimize our source we want to maximize the population of CaOH in the $\widetilde{X}^2\Sigma^+(000)$ $(N = 1)$ state. If we assume that the molecules are thermally distributed between rotational levels, the population in a single level is given by $P(N) \propto (2N+1) \times e^{BN(N+1)/kT}$ where $B \approx 0.5$ K is the rotational constant of CaOH and N is the rotational quantum number. Given the value of B, we find that the population in N=1 is maximized when the temperature is $\sim$1 K, as indicated in Figure 3.1.

Previous work in our lab has relied on pumped liquid helium to provide cooling at $\sim$2 K. However liquid cryogens have a number of disadvantages. Not only are they costly but as a cryogen reservoir is finite, they lead to experimental downtime as the reservoir periodically

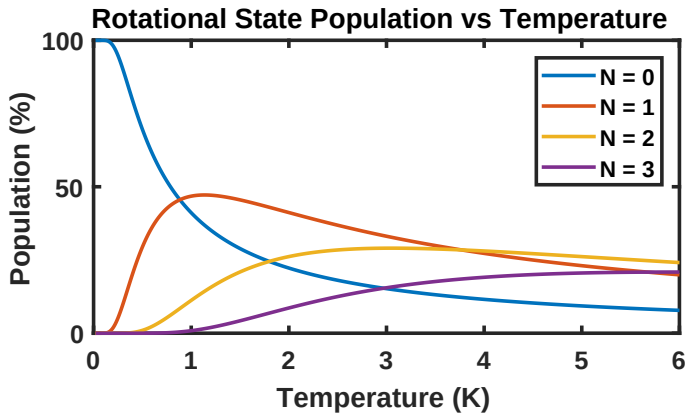

Figure 3.1: Population in each rotational state as a function of temperature for CaOH.

needs to be refilled. Careful cryogenic design can minimize these disadvantage by reducing the passive heat load to increase the amount of time between refills, but for this experiment we opted for a commercial system that can provide sufficient cooling power to maintain cell temperatures indefinitely.

3.1.1 Cryomech PT415 1 K cryostat

Our experiment uses a Cryomech PT415 1 K Cryostat depicted in Table 3.1. This system is comprised of two main components, a pulse tube (Cryomech PT415) and a closed cycled loop of helium gas. The pulse tube maintains active cooling on two surfaces, the 1^{st} stage at $\sim$40 K and the 2^{nd} stage at $\sim$4 K. These two stages provide cooling for blackbody radiation shields and charcoal sorbs which are described described later in this chapter. The cooling power of the pulse tube on the two stages is indicated in Table 3.1.

The closed cycle loop of helium gas enables the system to reach lower temperatures. He-

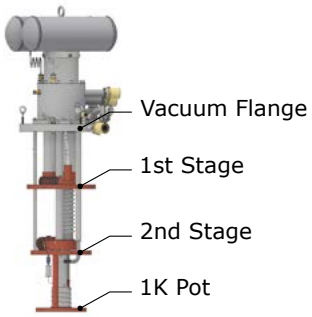

Figure 3.2: Diagram of the system that highlights the relevant surfaces.

Table 3.1: Tabulated cooling capacities of the PT415 with 1 K recirculating system.

1st Stage		2nd Stage		1K Pot	
Temperature (K)	Cooling Power (W)	Temperature (K)	Cooling Power (W)	Temperature (K)	Cooling Power (mW)
315.0	-	315.0	-	1.52	0
27.4	0.0	2.6	0.0	1.655	100
45.0	64.8	4.2	0.0	1.707	200
27.6	0.0	4.0	1.5	1.743	300
45.0	74.7	2.5	0.0	1.799	400

lium gas flows into the cryostat where it is precooled on the 40 K stage. It proceed to be liquefied on the 4 K stage. The liquid He is collected in the 1 K pot before being pumped out of the cryostat, providing cooling through evaporation. Our buffer-gas cell is thermally anchored to the 1 K pot and thermalizes to $\sim$2 K. This system is specified to be able to handle up to 400 mW of heat load at 1.8 K, which is sufficient for our needs. One must take care to prevent excessive heat load on either the 1^{st} or 2^{nd} stage of the pulse tube as this may heat the recirculating He reducing the cooling capacity of the unit or even preventing liquefaction.

3.1.2 Radiative heat transfer

Within the vacuum chamber, convective heating from the residual gas can be neglected. Radiative and conductive heat transfer must be considered carefully to limit the heat load de-

positing on the buffer gas cell. Power emitted by a black body is described by the Stephan-Boltzmann Law:

$$\dot{\mathrm{Q}} = \sigma A T^4 \tag{3.1}$$

Where the power emitted by a black body ($\dot{Q}$) is related to the Stephan-Boltzmann Coefficient (σ), the temperature (T), and area (A) of the object. Few objects are well approximated as a black body. A more complete theoretical description includes the emissivity which captures the overall effect of reflectivity of the object. For simplicity, the emissivity is often assumed to be a constant independent of wavelength. This description is known as a grey body where the power emitted is described by the following expression that includes the emissivity (ε).

$$\dot{\mathrm{Q}} = \varepsilon \sigma A T^4 \tag{3.2}$$

The emissivity can change the resulting power transfer due to blackbody radiation by several orders of magnitude and can be the determining factor in a successful design. The emissivity of several commonly used materials is listed in table Table 3.2

Our buffer gas cell, described in great detail later in this chapter, is a 2 inch cube made of copper. A quick calculation of the radiative heat load due to the room temperature vacuum chamber yields:

$$\dot{\mathrm{Q}} = (0.78)(\sigma)\left(6(2\text{ in})^2\right)\left((300\text{ K})^4 - (2\text{ K})^4\right)$$

$$\dot{\mathrm{Q}} \approx 5.5 \text{ Watts}$$

Material	Surface Finish		
	Polished	Oxidized	Unpolished
Aluminum	0.039 - 0.057	0.2-0.31	0.09
Copper	0.03 - 0.052	0.78	-
Gold	0.025	-	0.47
Stainless Steel	0.075	-	0.85
PTFE	-	-	0.92
Sapphire	-	-	0.48
Aluminized Mylar (NRC-2) aka “superinsulation”	-	-	0.044

Table 3.2: Emissivity of commonly used materials in buffer gas sources [159].

Table 3.3: Power per unit area emitted by a black body at a given temperature.

Temperature	300 K	77 K	40 K	4 K
Power per unit area (mW/cm^2)	46	0.2	1.5×10^{-2}	1.5×10^{-6}

Which by far exceeds the amount of cooling possible with our 1 K system. This highlights the need to reduce the radiative heat load. Given the strong temperature dependence of the power emitted by a grey body, reducing the temperature of the emitting surfaces lowers the heat load dramatically. We use the 1^{st} and 2^{nd} stages of the PT415 to provide cooling to two nested boxes that act as radiation shields as depicted in Figure 3.3. Table 3.3 indicates the relative heat load from black body radiation at several relevant temperatures and shows how quickly this heat load can be reduce to manageable levels.

The 40 K radiation shield cooled by the 1^{st} stage of the pulse tube is made of aluminum 6061 and measures 16.5” by 15” by 18”. Aluminum was chosen due to its low cost, light weight, and thermal conductivity. Given its relatively large dimensions, the heat load due to

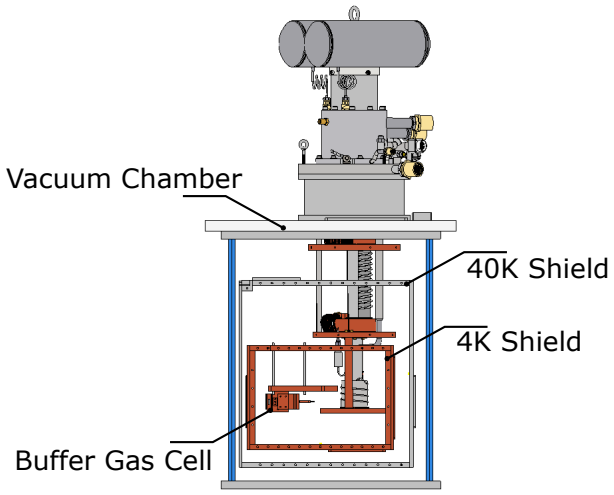

Figure 3.3: Beam box diagram with integrated PT415 1 K system highlighting the radiation shields.

black body radiation exceeds 350 Watts, assuming oxidized aluminum. In order to reduce this heat load to a reasonable level we use between 8-16 layers of superinsulation (aka aluminized mylar or NRC-2) to reduce the effective emissivity [160]. The effective emissivity of 16 layers of NRC-2 is $\varepsilon_{eff} \approx 1^{-3}$ which reduces the heat load by to an estimated ~ 0.5 Watts which is well within the cooling power of the PT415.

While a 40 K radiation shield would be sufficient to reduce the radiative heat load on the buffer gas cell, we also use the 4 K stage of the PT415 to construct an additional radiation shield. The primary purpose of this shield, discussed in Section 3.2, is to provide an anchor point for cryopumps to remove the ^{4}He buffer gas, but it also serves to block any stray room temperature radiation that might make it through gaps or imperfections in the 40 K shield.

3.1.3 Conductive heat transfer

In addition to the radiative heat load, we must also consider conductive heat transfer. A simple linear heat flow model given by Eq. 3.3 is sufficient to approximate the heat loads due to

conduction when the temperature difference is low. The total heat flow is given by

$$\dot{Q} = \frac{k\,A\,\Delta T}{L} \tag{3.3}$$

where $\dot{Q}$ is power, k is thermal conductivity, A is the cross sectional area, ΔT is change in temperature and L is the length. Thermal conductivity is strong a function of temperature so simple linear estimates are often poor approximations over large temperature ranges. The integral form of equation Eq. 3.3 is:

$$\dot{Q} = \frac{A}{L}\int k dT \tag{3.4}$$

Engineering lookup tables provide numeric solutions for the integral of k over standard temperature ranges. For managing heat loads one calculates $\dot{Q}$ but when designing thermal links Eq. 3.4 is algebraically inverted to solve for the acceptable thermal gradient ΔT.

Material selection is critical as the thermal conductivity varies widely across materials. Appendix B contains a number of useful references for thermal conductivity but Figure 3.4 is included in the main text to illustrate the range of thermal conductivity in different materials.

Thermal conduction through the pulse tube is ignored in this section under the assumption that the specified cooling capacity accounts for any heat leakage through the pulse tube itself. The 40 K and 4 K radiation shields are structurally disconnected from the pulse tube with flexible heat links in order to prevent thermally induced stresses from applying unintentional forces when the pulse tube is active. The radiation shields are rigidly supported with four $\frac{1}{4}$-20 stainless steel (316) threaded rods. Stainless steel is chosen for it low thermal conductivity and diameters of the threaded rods (0.188” minor diameter) is sufficient to provide rigidity while maintaining low thermal conductivity. The 40 K shields are suspended 4.75” below the room temperature vacuum chamber and the 4 K shields are suspended 5.75” below the 40 K shields,

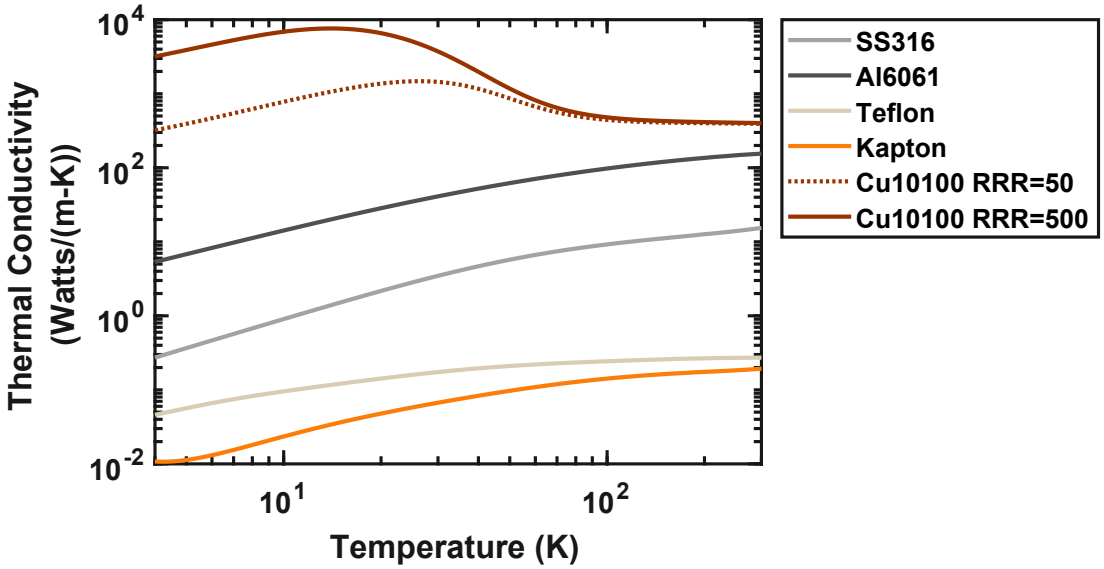

Figure 3.4: Thermal conductivity of commonly used materials in beam box design [161].

these figures lead to an estimated heat load due to conduction of:

$$\dot{Q}_{40} = \left(\frac{\pi \times (0.188")^2}{4.75"}\right) \int_{40}^{300} k_{SS304} dT \qquad \dot{Q}_4 = \left(\frac{\pi \times (0.188")^2}{5.75"}\right) \int_{4}^{40} k_{SS304} dT$$

$$\dot{Q}_{40} = 1.8 \text{ W} \qquad \dot{Q}_4 = 50 \text{ mW}$$

Thermal conduction through structural support is manageable with the choice of stainless steel threaded rods. The other source of conductive heat load are heaters and thermometers used to monitor and control temperatures in the beam box.

There are three types of thermometers used in the design of this beam box — DT470, DT670 and RX-102a all available commercially from Lake Shore Cryogenics. These thermometers rely on 4-wire readings to measure both voltage and current across the thermometer. DT470 and DT670 models are accurate from ∼4-500 K, while RX-102a thermometers are sensitive from 0.1 - 40 K. For heaters we use thin film resistors thermally anchored to copper lugs and apply heat by passing electrical current through the resistors. Appendix B contains a sec-

tion describing the production of these heaters. Heaters and thermometers must be connected to room temperature electronics, these connections can lead to unintentional conductive heat loads if make haphazardly.

If one were to naively use copper leads for these thermometers of a reasonable length ($\sim$1 m) and gauge (32 AWG) the resulting heat load can be substantial - 6.5 mW per wire - 26 mW per thermometer a substantial heat load when applied to the coldest sections of the beam box. To manage the heat load we typically use phosphor-bronze or manganin wire which reduces the heat load to $\sim$1 mW per thermometer.

The solution for heaters is not as simple, both phosphor-bronze and manganin have significant electrical resistance and applying current though resistive leads can cause the wire itself can heat substantially leading to failure or outgassing which compromises vacuum conditions. For this reason high resistances are often chosen for heaters to limit the required current, in addition we use copper leads that are thermally anchored to the 1^{st} and/or 2^{nd} stage where the higher cooling capacity makes the heat loads manageable. When $\pm$0.05 K accuracy temperature readings are desired, we also thermally anchor the thermometer leads. Whenever a electrical connection is made between materials maintained at different temperatures the gauge and length of wire is chosen carefully to ensure that we are not creating a thermal short.

Just as important as minimizing undesired heat loads, it is also critical to ensure that thermal connections made between materials designed to be at the same temperature are robust and the thermal conductivity is high. For this reason the beam box is made of materials with excellent thermal conductivity and the dimensions of the components are chosen to reduce thermal gradients wherever possible. Thermal contact between surfaces depends on the surface quality and the force compressing the joint [162]. Though two surfaces may appear to be in complete contact, there remains surface texture at the micrometer scale that reduces the effective cross sectional area through which heat transfer may occur. Increasing the force com-

pressing the joint deforms the surface structure increasing the effective cross sectional area. Preparing the surface by sanding at high grit (resulting in smoother surfaces) similarly improves thermal conductivity. An alternative approach is to use a compressible material (e.g. gold or indium) to fill the microscale voids between materials [162].

To avoid overconstraining the system as well as thermally induced stresses, flexible heat links are used to link the pulse tube to the radiation shields as well as the buffer gas cell. These heat links are constructed of braided copper (Cu10100) rope (AWG 2/0) with a cross sectional area equivalent of 0.67 cm^2 welded into copper lugs that can be screwed into place. An example of how to make these heat links is provided in Appendix B.

3.2 Vacuum constraints

In addition to cryogenic considerations, this apparatus must be able to create and maintain a vacuum to prevent attenuation of the molecular beam. The vacuum chamber is pumped down and vacuum is maintained by one 250 L/s turbomolecular pump (Varian V 250) which is backed by a SH-110 Scroll Pump. Both of these pumps are "dry" meaning no oil is used for lubrication and thus they are suitable for high vacuum applications. With these two pumps in operation and the beam box is a room temeprature, the vacuum chamber reaches pressures of $\sim$ 100 μTorr in a few hours and a base pressure of $\sim$ 1 μTorr over a few days. However, the radiation shields severely impede the pumping speed of any gas load created inside the 4 Kelvin region. During experimental operation the dominant gas load in the system is the helium buffer gas introduced into the cell to thermalize the molecular species. The turbomolecular pump used to evacuate the system is not sufficient to prevent a buildup a He inside of the cryogenic region. To alleviate this issue, we make use of charcoal adsorption pumps, or "sorbs".

3.2.1 Sorbs

Sorbs rely on the adsorption of gas molecules onto a surface at low temperatures. Any sufficiently cold surface will act as a pump causing gas particles to stick to it. However, as a surface becomes coated, the efficiency of pumping decreases for helium. Charcoal is used because it has macro and micro structure that vastly increases the effective surface area for gas adsorption ($\sim$ 1000 m^2/g [163, 164]). Much of this effective surface area resides within the grains of charcoal, and as a result particles typically are adsorbed on the outer layers and migrate to the interior of the charcoal granule. This migration process can be frozen out at low temperatures (2-3 K for helium) resulting in a loss of pumping speed [165, 163]. Pumping speeds of 6 L/s per cm^2 of apparent surface area can be achieved with charcoal sorbs at 4 K [6] the amount of sorb in our vacuum system should produce pumping speeds in excess of 2×10^4 L/s.

Under typical operating conditions we do not approach the levels of buffer gas flow that could cause saturation of the charcoal sorbs. While sorbs exposed to He can be readily regenerated by heating the sorbs to above 40 K, exposure to contaminants such as oils are known to cause a permanent reduction in pumping speed. In order to preserve the effective pumping speed of sorbs, we typically use stacks of charcoal sorb we refer to as "protected sorb". These stacks (e.g. in Figure 4.19) not only increase the surface area over which sorb can be applied but the sorb in the center of the stacks is protected from contaminants by the surrounding cold surfaces. The solid angle by which any contaminant may ballistically collide with the sorb in the center is very low. Even with protected sorb it is a good practice to replace any sorb on the timescale of a few years to maintain the pumping speed of the vacuum system. The addition of other contaminates such as methanol may also cause a degradation in sorb pumping speed, therefore best practices would replace sorbs more frequently if a convenient opportu-

nity arises.

The heat of adsorption for helium gas on charcoal can be conservatively estimated at 2 kJ/mol [163, 166]. This implies that a flow of 10 sccm of helium buffer gas will contribute a heat load of a few mW over all available surface area. As a result the additional heat load due to sorbs is negligible. A detailed procedure for making sorbs is available in Appendix B.

3.3 Buffer gas cell design

Our buffer gas cell is based on the design from Hsin-i's thesis [89] and the design used to laser cool CaF [14]. While much of the work described in this thesis would be possible with the faster, brighter single stage buffer gas cell [167], for reasons outlined in Section 4.8 a single stage source was not effective in this apparatus and we will not describe it here. This section will focus on the two styles of two-stage buffer gas cells used in this work. The performance of the cells is comparable. This section will focus on the relevant cell parameters and heat load considerations from the hot methanol capillary often referred to as the hot fill line (HFL).

3.3.1 Two-stage buffer gas cell

We varied a number of parameters of our buffer gas cell in order to optimize beam properties. Much of this work was done with Ca atoms, which were later found to misrepresent CaOH beam properties. As a result, I have restricted this section to technical considerations of the hot fill line. The production of molecules will be discussed in the next chapter. Our buffer gas cell is pictured in Figure 3.5. The dimensions listed here produce the bright and slow beam of CaOH described in later chapters. All metal components are made of copper 10100 unless otherwise noted. The buffer gas cell has an inner diameter of 1" and is 2" in length. The 1^{st} aperture is 5 mm in diameter. The 2^{nd} stage aperture is 7 mm in diameter and it is covered by

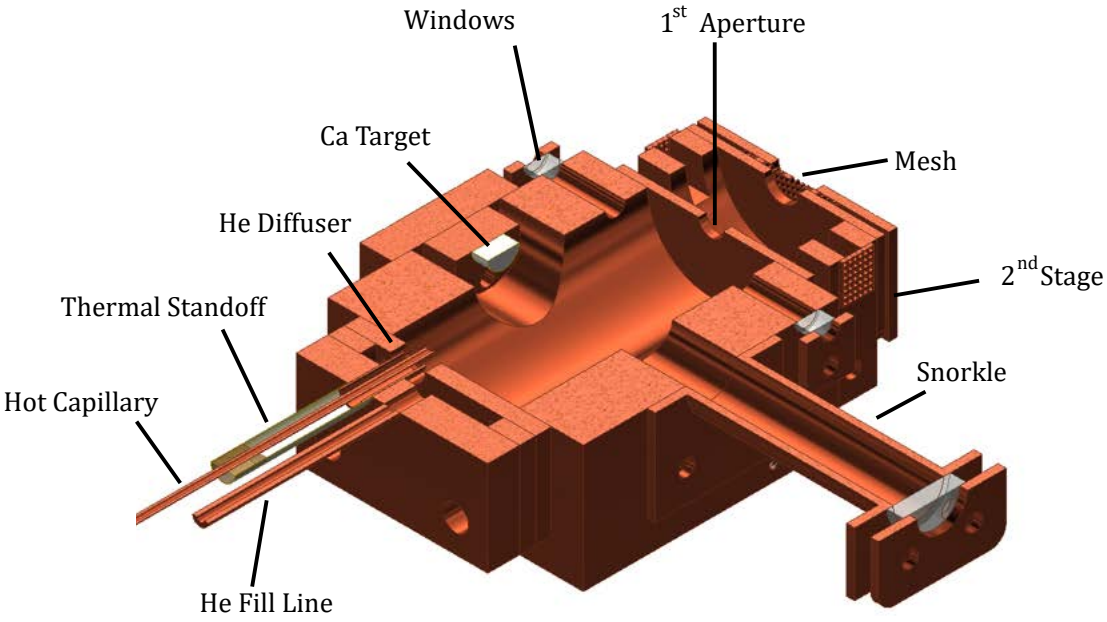

Figure 3.5: 2 stage buffer gas cell depicted in cutaway.

a 42% transparency mesh with pore sizes of $\sim$ 0.8 mm. The mesh is an unspecified copper alloy used in past buffer gas cell designs. Smaller pore sizes have been observed to produce slightly slower molecular beams. The 2^{nd} stage is spaced 2.8 mm from the 1^{st} stage with copper washers. There is a flexible heat link from the 1^{st} stage to the 2^{nd} stage to ensure good thermal contact. Helium enters the cell through a 1/8" copper diameter tube centered on the back of the cell it encounters a diffuser before entering the main cell volume. The calcium target is set approximately flush with the cell inner diameter. The ablation window provide optical access to the target is at the end of a snorkel to minimize the accumulation of dust and other debris from ablation. The cell is held together with 4 brass threaded rods. These rods are also used as anchor points used to support the HFL with kevlar thread.

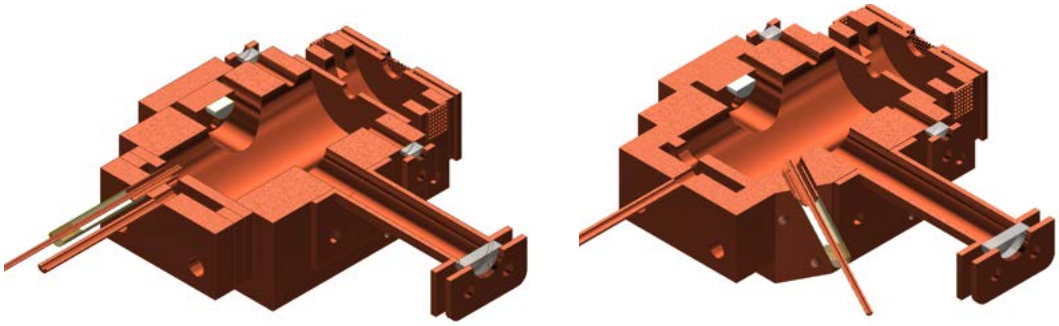

Figure 3.6: Buffer Gas cell designs used in this work. (left) Initial buffer gas cell design based on the buffer gas cell used to laser cool CaF [14]. In this configuration the hot capillary enters the back of the buffer gas cell. (right) buffer gas cell design used after moving cell away from the 4 K surface see Figure 4.15. Here the hot capillary is directed directly at the calcium target. No significant difference in performance was noted between these cell designs.

3.3.2 Hot fill line

The HFL used to introduce methanol into the buffer gas cell is based on the design from the CaF experiment, where it was used to introduce sulfer hexafluoride into the buffer gas cell [14]. The HFL was designed to operate at room temperature $\sim$ 290 K to maintain methanol vapor pressure. [168, 169]. It was empirically discovered that operation at 250 K was sufficient. This design separates the HFL into two parts: First, the majority of the HFL made of 1/16" diameter tube that has heaters at regular intervals; Second, the HFL end which enters the buffer gas cell. These two elements are connected with a flexible length of PTFE tubing which shrinks at cryogenic temperatures making a seal against vacuum. This modular design was necessary to facilitate routine maintenance.

For the first component, we initially used a stainless steel tube studded with resistors at 1" intervals with thermometers at the top and bottom of this length. The poor thermal conductivity of the stainless steel allows this design to be "turned off", removing excess heat load from the cell. This allowed us to measure the effect of the HFL temperature on the properties of a calcium beam. We concluded that there are no significant differences in beam properties with

the HFL on or off. Eventually we switched from stainless steel to copper for the length of the HFL in order to increase the thermal conductivity, reducing the risk of an unwanted cold spot. The HFL length is wrapped with superinsulation to minimize the radiative heat loss in the line and minimizing heat load in the cryogenic apparatus.

The second part of the design allows us to carefully manage the heat load on the buffer gas cell. It consists of a 1/16" diameter copper capillary that is heated with two (redundant) 1 kΩ resistors and is thermally isolated from the cell. This capillary is held in place with a Teflon thermal standoff, made of 2:1 PTFE heat shrink, this heat shrink has an inner diameter of 0.188" is 0.005" thick and 1.1" long. It is connected to the capillary with a small (3/8" long, 3/16" diameter) Ultem cylinder that is snug on the copper capillary. These dimensions lead to an estimated heat load of$\sim$ 25 mW by conduction with a $\Delta T = 300K$. The radiative heat load of the HFL dominates at $\sim$ 200 mW. In combination, the heated fill line is estimated to add 225 mW to the Buffer Gas cell, which is in good agreement with experimental data.

It should be noted that the major failure mechanism for this design was the formation of a thermal connection between the end of the copper capillary and the buffer gas cell. This could occur if the HFL moved slightly during cool down or if methanol ice made a connection between the end of the HFL and the buffer gas cell. It is critical to secure the HFL end that enters the buffer gas cell so that it cannot move. This is accomplished by using carefully tensioned kevlar strings to secure the hot capillary. Properly secured the entire buffer gas cell can be manipulated by the HFL. Images of a secured HFL are shown in Figure 3.7

3.4 Improvements and considerations for future designs

While this system is quite robust, there are several areas that could be improved in future designs. For practical considerations, it is useful to warm up and cool down rapidly. The cool

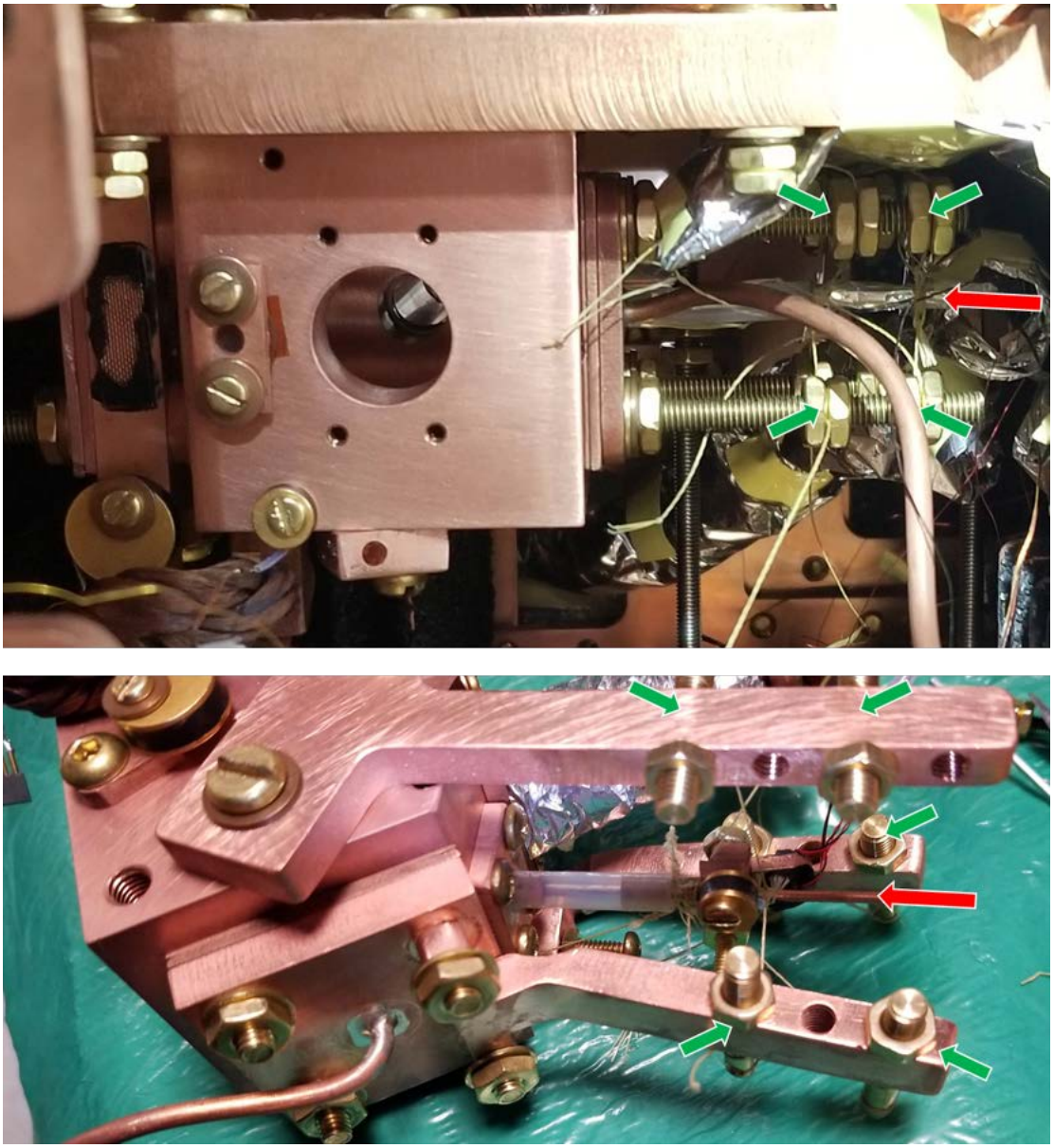

Figure 3.7: (top) *In situ* buffer gas cell with HFL coming out the back. Brass rods that compress the cell components provide support for the HFL. (bottom) Buffer gas cell with HFL at an angle. Pictured support structure (colloquially named the "claw") provides rigid support of the HFL. HFL indicated in red. Anchor points indicated in green.

down time for this apparatus is approximately 18 hours. While this is favorable compared with other similar experiments, reducing this time to 12 hours would allow you to thermally cycle the dewar overnight allowing rapid prototyping. In the current apparatus deicing of methanol can be achieved in 12 hours reaching a maximum temperature of 180 K before returning to 2 K. This dewar was designed to minimize thermal gradients across the radiation shields and performs well in this respect. However, reducing the amount of thermal mass on the radiation shields could significantly reduce the cool down time. Similarly, the addition of large heaters ($\sim$ 500 W/shield) to facilitate a rapid warm up would be useful.

As described in Section 4.8, the major issue with this system is the buildup of helium inside of the 4 K region. In order to mitigate or eliminate this issue, I would recommend that any future experiment maintain at least 4" of distance between the cell exit and the 4 K surface. In addition I suggest large amounts of protected sorb around the 4 K aperture. Future designs should allow the distance of the cell to the 4 K aperture to be modified easily.

The HFL is another area where future designs may improve. This dewar requires the HFL to enter from the side of the beam box, which causes some complications when removing the cell for maintenance. Future designs that incorporate HFLs should strongly consider having them enter the cryogenic space from the back with as few contortions as possible. In addition, the HFL should be gold plated to reduce emissivity and potential radiative heat load.

There are several features of this beam box that constrained the design but were never used. This beam box can accommodate a second pulse tube. Now that the system has been shown to operate sufficiently with a single pulse tube, future designs should use a centered pulse tube with the cell mounted below lowest surface of the pulse tube for convenient access. Additionally, this design was intended to be used in combination with a 2D MOT and as a result the radiation shields in the direction of molecular beam propagation are closely spaced to minimize the distance to the transverse cooling region. In future designs, I would recommend leaving at

least 1.5” between surfaces to ensure a vacuum conductance in excess of 100 L/s. To further ensure high conductance, polished gold-plated copper can be used in place of super insulation as a means of reducing emissivity on the 77K shield.

4

Cryogenic production of CaOH

CaOH is reactive and cannot be stored for long periods of time under normal conditions. In order to study this polyatomic radical it must be created *in situ*. There are several techniques that have been used to produce CaOH for study. Early studies relied on Broida ovens which produce molecules at relatively high temperature (500-700 K) [156]. Later, supersonic beams were employed to obtain internally cold samples and allowed for rotationally resolved spectroscopy [150, 170]. CaOH is produced in this work with a buffer gas source, described in the preceding chapter. This production method is well matched to a direct laser cooling experiment because it produces a bright cryogenic buffer-gas beam with a forward velocity near the effusive limit. This chapter will describe and characterize our cryogenic source.

4.1 Buffer-gas cooling

In order to produce CaOH radicals we use a combination of laser ablation and buffer gas cooling. A diagram of our buffer gas cell is shown in Figure 4.1. The molecules are introduced into the gas phase by ablation of either a solid pressed-powder precursor $Ca(OH)_2$ or ablation of a calcium metal target in the presence of methanol vapor. The CaOH molecules rapidly thermalize through elastic collisions with helium buffer gas. The He buffer gas is introduced into the cell at flow rates of 1-10 standard cubic centimeters per minute (sccm). This flow rate allows us to tune the density of buffer gas in the cell from 10^{14} to 10^{16} cm^{-3}. Our buffer gas cell is thermally anchored to a recirculating liquid helium system that maintains a temperature of $\sim$ 2 K. Under these conditions, the mean time between collisions varies from τ = 0.7-70 μs. Elastic collisions thermalize the molecules translational and rotational degrees of freedom in $\sim$ 10-100 collisions [6, 87]. Thermalization of the vibrational degree of freedom in general is not as efficient [88]. As the energy of the vibrational excitation decreases, vibrational relaxation has been observed to occur more rapidly. Ref. [171] investigates vibrational relaxation for linear triatomic SrOH as well as summarizing similar results in other molecules. Within the buffer gas cell time dynamics may be studied with absorption spectroscopy or the molecules may be extracted into a cryogenic buffer-gas beam for further study.

4.1.1 Diffusion cross section for CaOH $\widetilde{X}$(000) (N = 1) – He at 2 K

Determination of the diffusion cross section of CaOH molecules with He buffer gas in combination with the measurements of excited vibrational state dynamics within the cell would allow measurements of the vibrational relaxation cross section [171]. The rate of vibrational relaxation can have significant impact on the natural population of excited vibrational states

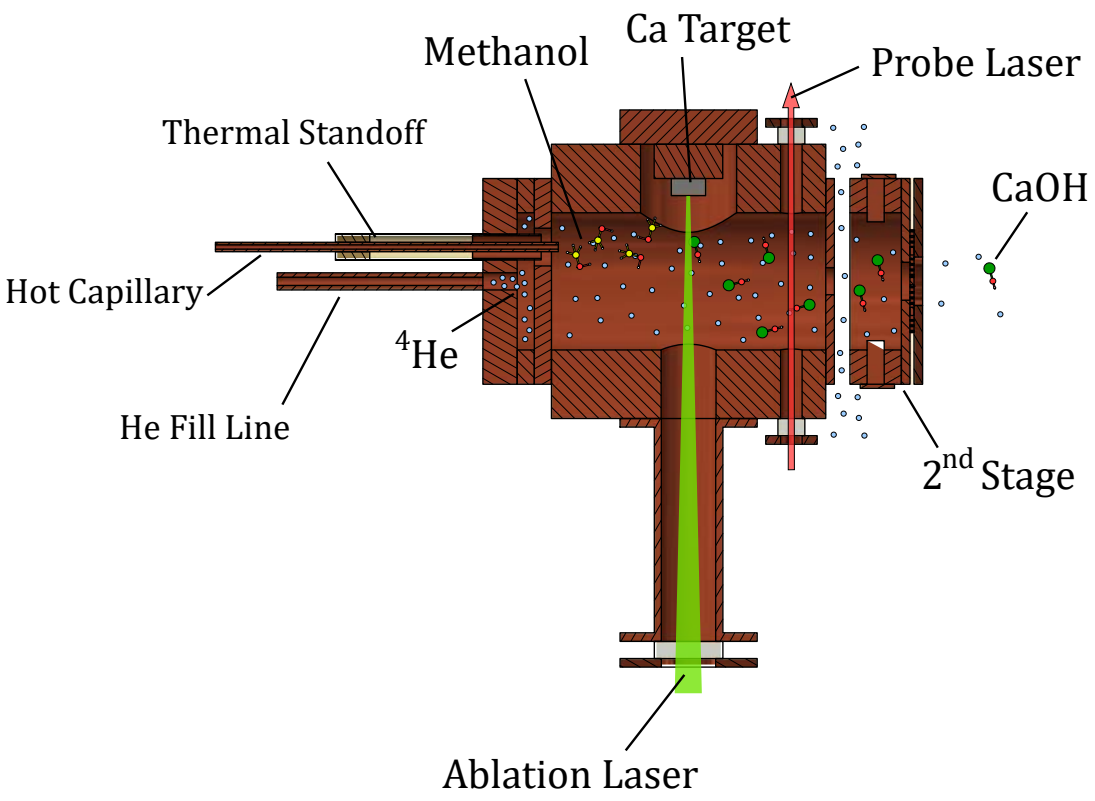

Figure 4.1: A diagram of our buffer gas cell with the hot capillary entering through the back. The cell is maintained at 2 K.

in the beam. This has implications for performing spectroscopy to determine optical pumping laser frequencies. As described in Appendix D, the spectroscopy we performed does not rely on natural population but uses optical pumping to populate the state of interest. As a result, no vibrational relaxation cross sections were measured in the course of this work. The diffusion cross section can be extracted using data taken to characterize the performance of the beam source.

We measure the diffusion cross section by monitoring the time dynamics of CaOH molecules inside of the buffer gas cell. Absorption spectroscopy, described later in this chapter, allows us to monitor molecule density as a function of time. In combination with the molecule den-

sity, the temperature and density of helium buffer gas must be known. The temperature can be reasonably inferred from rotational state population distributions, Doppler broadening of spectroscopic features, and thermometer readings. We control the density of helium in our cell with a mass flow controller, which allows us to vary the buffer gas flow from 0-10 standard cubic centimeters per minute (SCCM). In order to convert a flow rate into a density, we rely on the steady state assumption that flow into the cell is equal to the flow out of the cell.

$$\frac{f}{V} = \frac{n_{He}}{\tau} \tag{4.1}$$

Where f is the flow rate in atoms/second and n_{He} is the number density of He, and τ is the pump out time ($\tau = \frac{V}{C}$ where C is the conductance of the cell exit aperture. Using Eq. 3.72 from [172] the expression for conductance of an aperture in the molecular flow regime is described by:

$$C = 3.64 \times 10^3 \, A \sqrt{\frac{T}{M}} \tag{4.2}$$

Here C is in units of cm^3/sec, T is the temperature in Kevin, M is the mass in amu and A is the open area of an the aperture in cm^2. While we have made many changes to our buffer gas cell, for the data presented below the relevant parameters yield a conductance of C = 1260 cm^3/sec. After some algebraic manipulation Eq. 4.1 becomes:

$$\frac{f}{C} = n_{He} \tag{4.3}$$

The calculated conductance allows a conversion between flow rate and helium density. 1 SCCM of flow is 7.5×10^{17} atoms/sec, corresponding to a helium density of $\sim3\times10^{14}$ atoms/cm^3. For this cell geometry the helium density can be tuned from 1×10^{14} to 3×10^{15} atoms/cm^3.

The time decay of molecular signal during an ablation pulse is due to diffusion of molecules to the cell walls and pump out of the cell through the aperture. This is mathematically described as:

$$\frac{1}{\tau_{000}} = \frac{1}{\tau_{\mathrm{d}}} + \frac{1}{\tau_{\mathrm{p}}} \tag{4.4}$$

Where τ_{000}, τ_{d}, and τ_{p} are the timescales for the decay of (000) vibrational mode molecules (τ_{000}) due to diffusion (τ_{d}) and cell pump-out (τ_{p}). For low buffer-gas flows $\tau_{\mathrm{d}}/\tau_{\mathrm{p}} < 1$ [90], and the molecule loss is primarily due to diffusion to the cell walls. Therefore, from our measurements of τ_{000} we can directly determine the diffusion lifetime of the molecules in our cell: $\tau_{\mathrm{d}} \approx \tau_{000}$.

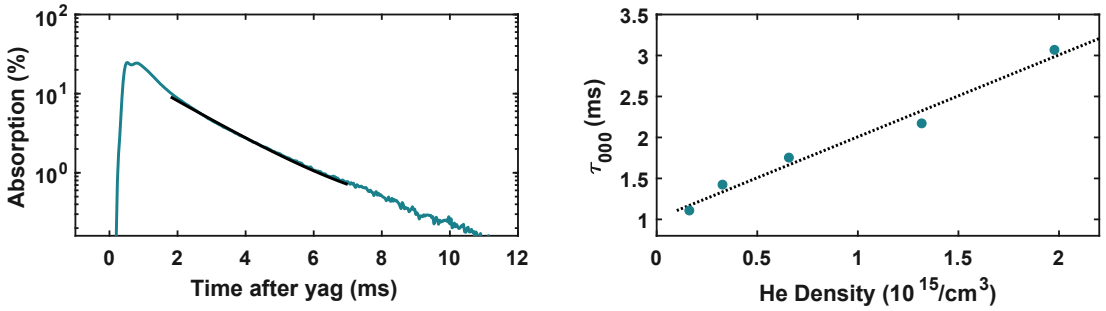

Figure 4.2: (left) In-cell absorption signal of CaOH $\widetilde{\mathrm{X}}(000)$ (N = 1) molcules vs. time. An exponential fit (black) is overlayed showing excellent agreement after initial ablation dynamics subside. (right) fitted decay time (τ_{000} vs helium density. The linear dependence fits the model described by Eq. 4.5

When higher-order diffusion modes have decayed, the in-cell $\widetilde{\mathrm{X}}(000)$ population profile is well fitted by a single exponential (Figure 4.2). We determine the CaOH-He momentum transfer cross section by measuring the diffusion lifetime of CaOH $\widetilde{\mathrm{X}}(000)$ molecules as a function of helium density. From Figure 4.2 we find that τ_{000} has a linear dependence on the helium density and conclude that (000) mode molecule loss is primarily dominated by diffusion. For a cylindrical cell of length L and radius r the time constant of the exponential decay for molecules diffusing through helium gas of density (n_{He}) is given by [173]:

$$\tau_d = \frac{n_{He}\,\sigma_d}{\bar{v}\,G} \tag{4.5}$$

$$G = \frac{3\pi}{32}\left(\frac{j_{01}^2}{r^2} + \frac{\pi^2}{L^2}\right) \tag{4.6}$$

where $\bar{v} = \sqrt{8k_BT/\pi\mu}$ is the mean CaOH $-$ ^{4}He collision velocity at temperature T with reduced mass of the atom-molecule system μ and the diffusion cross section σ_d and $j_{01} \approx 2.405$ is the first root of the Bessel function $J_0(x)$. Eq. 4.5 reflects that in the diffusive regime (τ_d/τ_p<1) the in-cell lifetime is directly proportional to the helium density, as seen in our data (Figure 4.2).

Measurements of τ_{000} at different helium density allow us to extract the value of the diffusion cross section, $\sigma_\mathrm{d} \approx \tau_{000}\bar{v}G/n_\mathrm{He}$, using Eq. 4.5. We determine the CaOH diffusion cross section in He at 2 K to be $\sigma_\mathrm{d}(\mathrm{CaOH} - {}^4\mathrm{He}) = 1.3(4) \times 10^{-14}\,\mathrm{cm}^2$ where the error is dominated by the uncertainty in the He density. The CaOH $-$ He diffusion cross section is similar to SrOH [171] and larger than previously measured for diatomic molecules [174, 175].

4.2 Absorption spectroscopy

Buffer gas cell geometry plays a significant role in the characteristics of the atomic or molecular beam produced during an ablation event. While there is much left to be optimized for a given production technique or species, there have been significant efforts to characterize the performance of buffer gas cells [88, 176, 89]. This work will focus specifically on the production of CaOH for the express purposes of laser cooling and magneto-optical trapping. Absorption spectroscopy is an invaluable technique to monitor production of atomic or molecular species which can accurately determine the density produced in a buffer gas cell. In short this

technique relies on the resonant absorption cross section of the species of interest to scatter photons from a laser probe beam, attenuating its transmission. By monitoring the probe beam power one can determine the density and temperature of the species of interest.

The resonant absorption cross section[1]. (σ_0) is [177]

$$\sigma_0 = \frac{\lambda^2}{2\pi}\frac{2J'+1}{2J''+1} \tag{4.7}$$

where J'' is the total angular momentum in the ground state and J' is the total angular momentum in the excited state. For a finite temperature sample Doppler broadening contributes to frequency dependence as follows [177]

$$\sigma(\delta) = \sigma_D e^{-(\frac{\delta}{\Gamma_D})^2} \tag{4.8}$$

where δ is the detuning from resonance, $\sigma_D = \frac{\sqrt{\pi}}{2}\frac{\gamma}{\Gamma_D}$, Γ_D is the Doppler width, and γ is the natural linewidth of the transition. The Doppler width is given by[2]:

$$\Gamma_D = \sqrt{\frac{2k_BT}{mc^2}} f_o \tag{4.9}$$

For CaOH, reasonable experimental parameters are as follows: a Doppler temperature of 3.2 Kelvin fitted from Figure 4.4 corresponding to $\Gamma_D = 34.5$ MHz, $\gamma = 6.25$ MHz [178] and $\lambda = 626$ nm. This results in a $\sigma(\delta = 0) = 5.6 \times 10^{-11}$ cm^2 when using the $(J'' = \frac{3}{2}) \rightarrow (J' = \frac{1}{2})$ transition. We then use Beer's laws to describe the attenuation of light as it propagates through a sample [132].

[1] Under the assumption that the lifetime is dominated by spontaneous decay to a single state. See eq. 3.145 in [177] for details.

[2] Convention varies. The factor of 2 in the numerator can absorbed into the standard form of a Gaussian distribution.

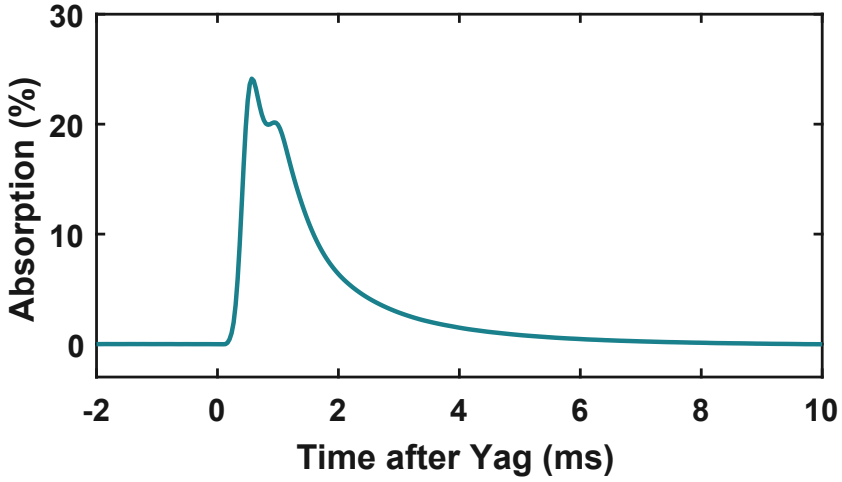

Figure 4.3: Resonant in-cell $\widetilde{X}^2\Sigma^+(000) \rightarrow \widetilde{A}^2\Pi_{1/2}(000)(P_1)$ line CaOH Absorption signal While ablating a $Ca(OH)_2$ pressed powder target. This trace is consistent with an in-cell density of 1.6×10^9 molecules/cm^3

$$\frac{I}{I_0} = e^{-\sigma\, n_0\, l} \tag{4.10}$$

Using a typical in-cell absorption trace given by Figure 4.3 the absorption signal is ∼20% and the cell diameter or l = 1" which implies we have an in-cell density of;

$$\frac{I}{I_0} = e^{-\sigma\, n_0\, l} \tag{4.11}$$

$$ln(.8) = -\sigma n_0 l \tag{4.12}$$

$$\frac{ln(.8)}{-\sigma l} = n_0 \tag{4.13}$$

$$n_0 = 1.6 \times 10^9 \text{molecules/cm}^3 \tag{4.14}$$

which is a factor of ∼ 3 lower than the number of diatomic molecules (CaF,CaH,SrF) produced by similar sources [176, 14, 179]. CaOH is produced via two methods, either by abla-

tion of a $Ca(OH)_2$ pressed-powder target or through a chemical source where methanol vapor is introduced to the buffer gas cell which reacts with calcium atoms created by ablation of a calcium metal target. The number of calcium atoms produced through either of these methods exceeds the number of CaOH molecules. Typically, the in-cell density of calcium atoms is $\sim 10^{12}$ atoms/cm^3 as measured through absorption. The calcium atoms produced during ablation can be used for two purposes. Given the higher flux of atoms compared with molecules they can be used to debug and characterize the source with high signal to noise. In addition, one may convert the excess Ca to CaOH molecules with a deep understanding of the chemical reactions between calcium atoms and OH containing molecules such as water, hydrogen peroxide, and methanol that result in CaOH [154, 156, 180, 170, 181].

4.3 Ablation of $Ca(OH)_2$ pressed powder target

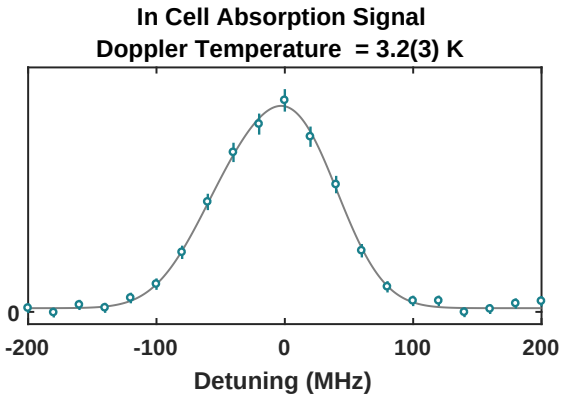

Figure 4.4: In-cell absorption spectrum for CaOH. The 52 MHz spin-rotation splitting is unresolved in the cell as Doppler broadening dominates the lineshape of the transition. A fit to two Gaussian profiles split by 52 MHz indicates a translational temperature of 3.2(3) K.

One technique that reliably produces CaOH molecules is ablation of a $Ca(OH)_2$ target. We

compress $Ca(OH)_2$ powder into a solid precursor and ablation produces CaOH radicals in the gas phase. These molecules are produced in a buffer gas cell with a transverse Doppler temperatures of 3.2 K as shown in Figure 4.4. Doppler broadening obscures the 52 MHz spin-rotation splitting of CaOH in this spectrum [142]. Ablation produces the molecules at high temperatures and the molecules thermalize is a few ms as can be seen in Figure 4.5.

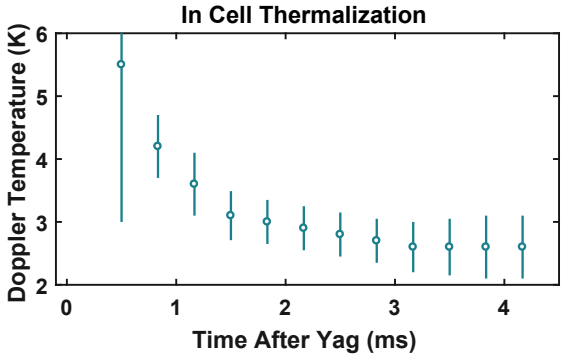

Figure 4.5: Doppler temperatures as a function of time after ablation. Temperature of the molecules decreases as they thermalize with the cell mediated by elastic collisions with ^{4}He buffer gas

4.4 Chemical production of CaOH

Several laser cooling experiments use sources based on ablation of solid targets [182, 183, 179], others rely on chemical production methods [184, 14]. For CaF, solid precursor targets have been shown to degrade on the timescale of days leading to an increases in beam velocity [14]. This is attributed to a build of up dust inside the buffer gas cell, a known issue observed for several species including CaH, CaF, and SrOH [89, 167, 14].

Motivated by the potential for a brighter and more stable source of CaOH, we tested chemical production. We tried a number of different chemical reactants to produce CaOH, indicated in the list of reaction shown in Table 4.1. At room temperature these reactants are all liquids. We were able to introduce the reactants into the buffer gas cell through a capillary held at 250

Reaction	ΔH_0^0 (kJ/mol)
$Ca(^1S_0) + H_2O_2 \rightarrow CaOH + OH$	-199
$Ca(^1S_0) + CH_3OH \rightarrow CaOH + CH_3$	-29
$Ca(^1S_0) + H_2O \rightarrow CaOH + H$	88
$Ca(^3P_2) + H_2O_2 \rightarrow CaOH + OH$	-382
$Ca(^3P_2) + CH_3OH \rightarrow CaOH + CH_3$	-212
$Ca(^3P_2) + H_2O \rightarrow CaOH + H$	-95

Reaction	ΔH_0^0 (kJ/mol)
$Ca(^1S_0) + CH_3OH \rightarrow CaOCH_3 + H$	23
$Ca(^3P_2) + CH_3OH \rightarrow CaOCH_3 + H$	-154

Table 4.1: This table indicates the reactions that have been used in the literature to produce CaOH and $CaOCH_3$. This is a partial reproduction of Table 23 from ref. [181]. ΔH_0^0 is enthalphy of the reaction and a negative enthalphy indicates that the reaction is exothermic.

K. We did not observe significant CaOH production when using water vapor seeded with $\sim$1% hydrogen peroxide as a reactant. The low vapor pressure of hydrogen peroxide compared to water limited the maximum concentration of hydrogen peroxide. We were unable to find hydrogen peroxide in a form where we could introduce it at higher concentrations. However, significant CaOH production was observed using methanol as a reactant (Figure 4.6).

We found that the production of CaOH molecules from the Ca + Methanol chemical reaction is an order of magnitude better then the pressed powder targets when ablating with lower YAG laser pulse energy. Because the energy of the ablation laser is correlated with molecular beam velocity this is potential advantage over a pressed powder target. At higher ablation energy, similar production is observed, but the molecular beam from pressed-powder contains a factor of 2 more molecules. The discrepancy in the molecular beam is likely a result of a

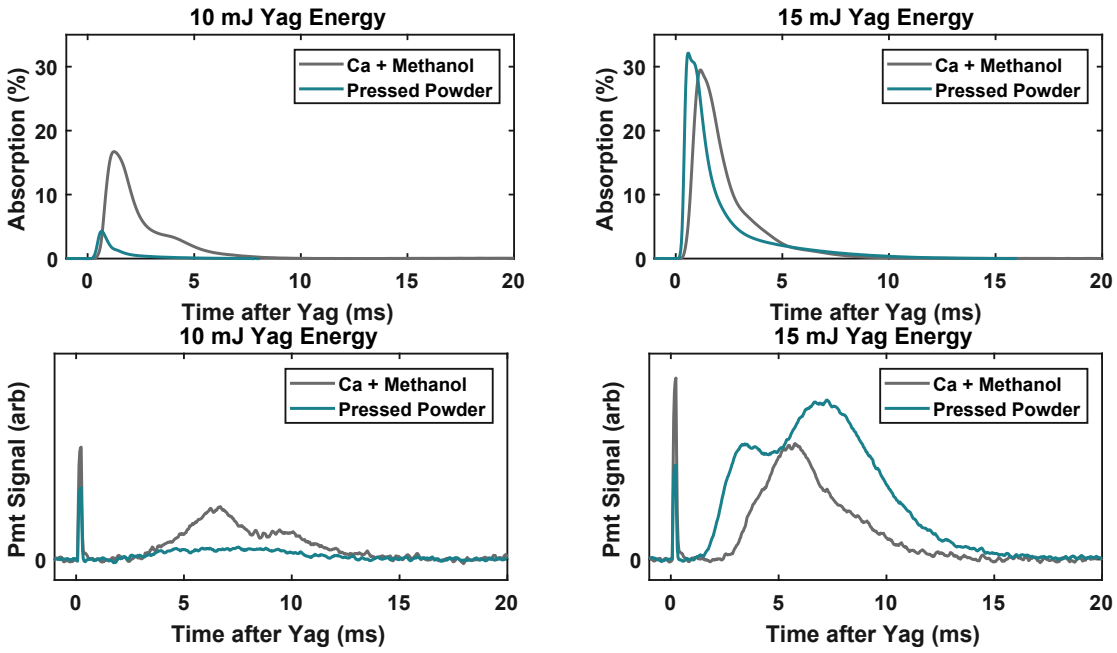

Figure 4.6: (top) In-cell and (bottom) in beam comparison of chemical and powder sources. Methanol vapor is introduced to the cell at a rate of 0.12 sccm. (left) At lower YAG energies (10 mJ) the calcium and methanol chemical source produces significantly more molecules then the pressed powder target. (right) At higher YAG energy (15 mJ) the pressed powder performs similarly to the chemical source.

buildup of helium gas inside the 4 K section (described in Section 4.8.2) that is exacerbated by methanol ice.

Figure 4.7 shows the CaOH molecular signal as a function of methanol flow into the buffer gas cell. CaOH production saturates at flow rates of ∼0.05 sccm to signal levels that are comparable to the pressed powder at high YAG energies. One significant benefit of the chemical source compared to a pressed powder source is a significant increase in the stability of the source. Pressed powder targets have shot to shot fluctuations where the molecular signal varies by nearly 100%. The chemical source typically has shot to shot fluctuations of of 10-20%. This stability is vital when scanning experimental parameters to optimize parameters.

There are some drawbacks of using the chemical source. Introduction of methanol vapor to the buffer gas cell leads to a build up of methanol ice on the interior of the cell. Similar ice

buildups have been observed for CaF chemical production sources [184, 14]. While flowing methanol into a cell, we observe an increase in beam velocity and a degradation in molecular signal (see Figure 4.8) that we attribute to the build up of methanol ice inside of the cell. Not only do we observe that reducing the methanol flow increases the timescale for these issues but we can also "de-ice" the cell (warm up to temperatures of ∼200 K [168]) in order to recover the molecular signal and beam velocity profile of a clean cell.

We have experimentally determined that in order to produce a stable signal of CaOH molecules over 1 week of experimental work we must reduce the methanol flow to 0.02 sccm which reduces our CaOH signal by a factor of 4 when compared with a pressed powder target. The ability to "de-ice" the cell allow us to operate with the same target for approximately 3 months without cleaning the cell or replacing the target. It may be possible to modify the cell geometry to alleviate some of the limitations imposed by methanol ice, but currently there are advantages and disadvantages to both the pressed powder and chemical source of CaOH.

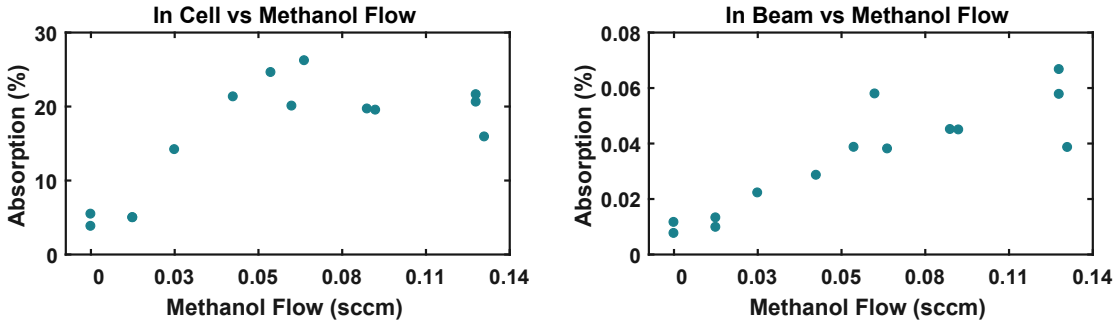

Figure 4.7: Production of CaOH molecules using calcium and methanol chemical reaction as a function of the flow rate of methanol vapor into the buffer gas cell. (left) In-cell absorption signal. (right) Absorption signal 1 cm away from cell exit.

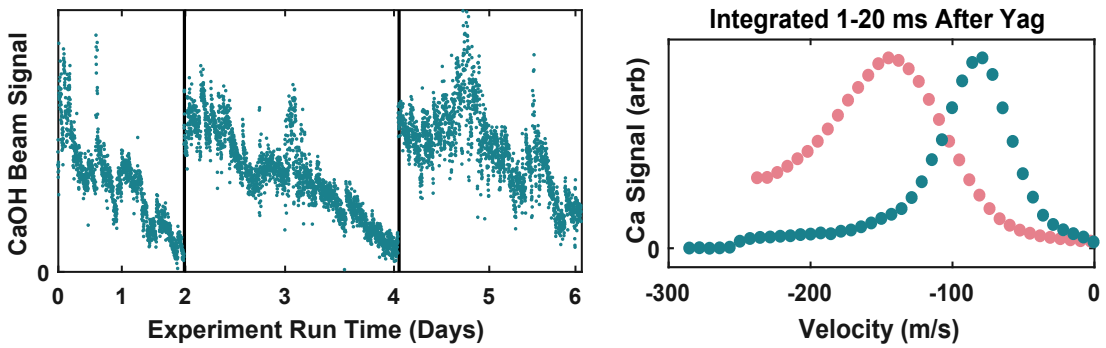

Figure 4.8: (left) CaOH beam signal vs experimental run time. Black vertical lines indicate de-ice cycles. While the signal is recoverable upon deicing the cell, a rapid degradation in beam signal is observed at methanol flow rates of 0.04 sccm. This timescale can be extended to $\sim$ 1 week by reducing the flow to 0.015 sccm with a corresponding decrease in molecular signal (Figure 4.7). (right) the velocity of a beam of calcium atoms is shown in pink, after a de-ice cycle the velocity profile changes to the blue data points.

4.5 Excitation of metastable Ca to enhance CaOH production

Increasing the brightness of our molecular source would accelerate progress towards magneto-optical trapping. In a typical ablation pulse, the ratio of CaOH molecules to calcium atoms is approximately 1:10[3] If even a small fraction of the calcium atoms produced during ablation could be converted into a molecules it could significantly enhance the brightness of our source. The literature reports enhancement of CaOH molecule production when the calcium atoms are in the excited metastable $^3P_1$ state [170, 187, 188]. Recent efforts using Yb atoms to produce YbOH molecules was able demonstrate an order of magnitude increase in YbOH production by exciting Yb atoms into the metastable $^3P_1$ state [189].

In calcium there are several pathways that may be used to populate the $^3P_1$ state. These pathways are depicted in Figure 4.9. The strong $^1S_0$ to $^1P_1$ transition is typically used for laser cooling and the branching ratio from the $^1P_1$ state to the $^1D_2$ state is 1 part in 10^5 [190]. the $^1D_2$ state decays to the $^3P_1$ state with a lifetime of 2.2 ms. The calcium $^1S_0$ to $^1P_1$ transition

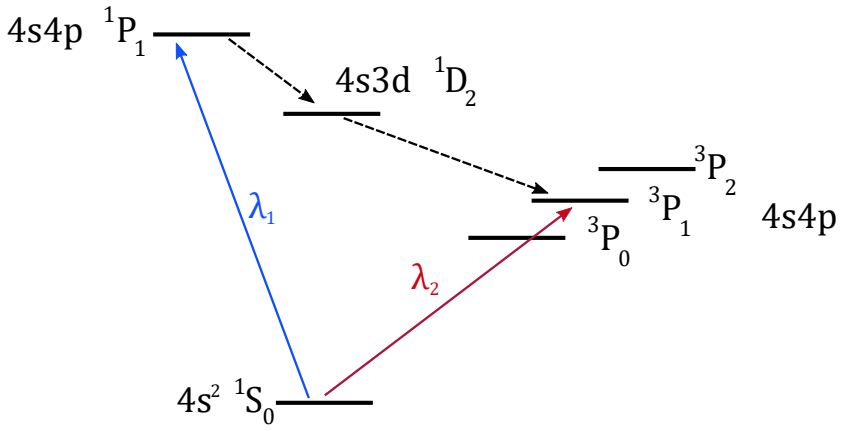

Figure 4.9: Calcium Energy Structure indicating metastable states used in previous chemical reactions to produce CaOH and Optical pumping pathways used to populate these states.λ_1 indicates the strong transition at 423 nm where the $^1P_1$ state has a lifetime of 4.6 ns and a corresponding natural linewidth of 34 MHz [185]. λ_2 indicates the intercombination line which is significantly weaker with a lifetime of .34 ms and natural linewidth of 410 Hz [186].

can easily be saturated and scattering rates of ∼100 MHz can be achieved. Thus, excitation of calcium atoms on the $^1S_0$ to $^1P_1$ transition can optically pump ground state atoms into the excited $^1P_1$ transition metastable state on the timescale of a few ms. Alternatively, calcium atoms can be directly excited to the $^3P_1$ state along the intercombination line. The small linewidth of this transition limits the number of atoms in the excited state and thus requires substantial laser power for efficient optical pumping.

4.5.1 Enhancement with $^1S_0$ to $^1P_0$ excitation (or lack thereof)

We attempted to observe enhancement through optical pumping through the $^1P_1$ state. The saturation intensity of the $^1S_0$ to $^1P_0$ transition is I_{sat} = 60 mW/cm^2 [190]. We used 55 mW of 423 nm laser light focused down to a beam waist of ∼ 0.5 mm leading to a saturation parameter ($s = \frac{I}{I_{sat}}$) of ≈100. The 423 nm laser copropagated with the YAG ablation laser in order to excite calcium atoms produced during ablation. To limit the heat load on the buffer

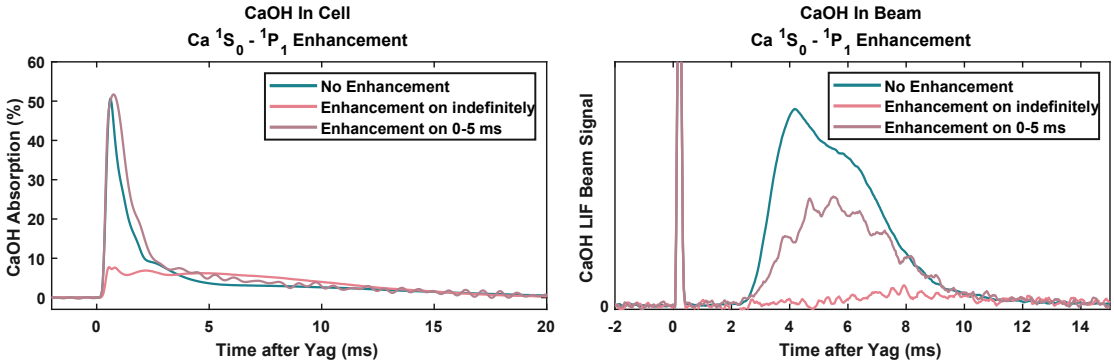

Figure 4.10: Here we see the effects of exciting the $^1S_0$ to $^1P_0$ transition in the cell copropagating with the Nd:YAG ablation beam. Additional light was seen to be detrimental to CaOH production both in the buffer gas cell and in the molecular beam. The detrimental effect was larger in the molecular beam and the reduction in molecule number was larger the longer the $^1S_0$ to $^1P_0$ excitation beam was applied.

gas cell we installed a shutter to control duration the excitation light. The results of these tests are shown in Figure 4.10.

The molecular signal was degraded by the excitation light and detuning the laser by several GHz indicated that this was not a resonant phenomenon. We attribute the reduction of the molecular signal in the presence of this excitation light to heating caused by the 423 nm laser.

4.5.2 Enhancement with $^1S_0$ to $^3P_1$ excitation

Exciting calcium atoms directly to the $^3P_1$ state requires a large amount of laser power given the relatively weak line strength and significant level of Doppler broadening in the buffer gas cell. The saturation intensity for the $^1S_0$ to $^3P_1$ transitio is I_{sat} = 190 μW/cm^2 [190]. Following ref. [177], the number of atoms in the excited state is:

$$\delta N \sim \frac{\gamma}{\Gamma_D} N_{tot} \tag{4.15}$$

Here δN is the fraction of atoms the light interacts with, γ is the power broadened linewidth, and Γ_D is the Doppler broadened linewidth.The power broadening is given by:

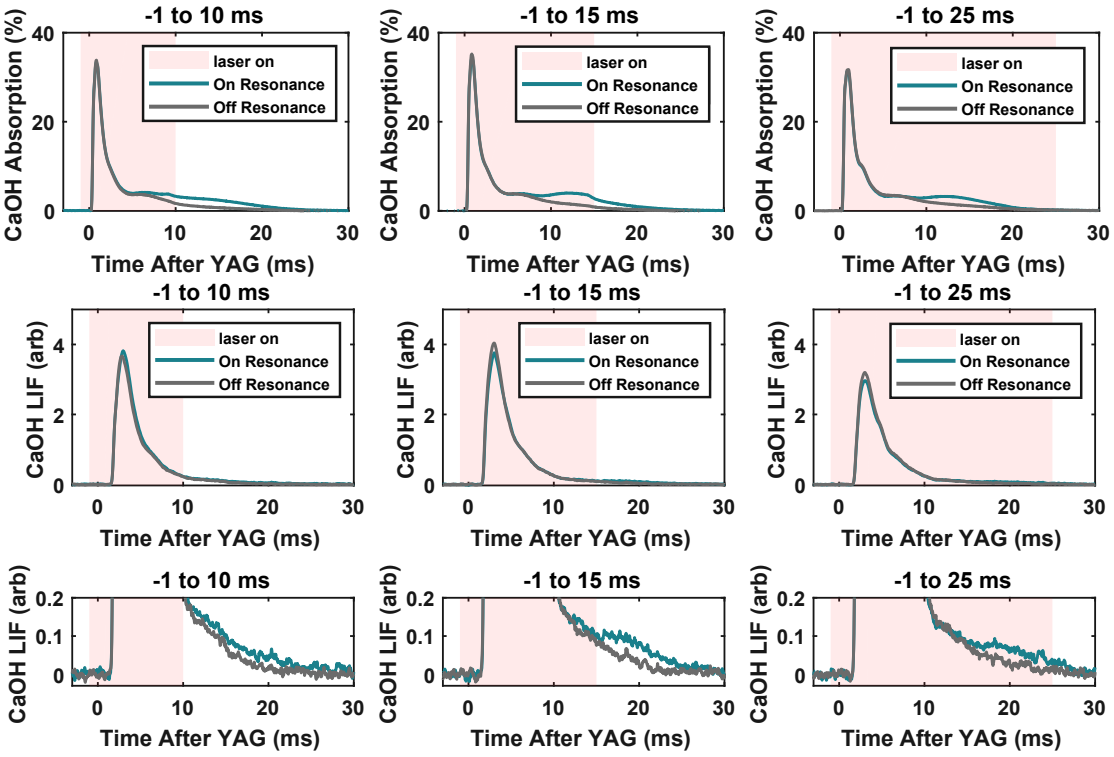

Figure 4.11: Molecular signal enhancement as a function of the time the enhancement light is applied. Shaded red area indicates the time interval during which the enhancement light is applied copropagating with the YAG ablation laser. The enhancement is measurably larger for longer time intervals as long as Ca atoms remain in the buffer gas cell (25 ms after ablation) The enhancement in beam is significantly smaller the effect in cell.

$$\gamma = \gamma_0\sqrt{1+s} \tag{4.16}$$

where γ_0 is the natural linewidth and s is the saturation parameter. Incorporating Doppler broadening from Eq. 4.9 the fraction of molecules in the excited state is:

$$\delta N \sim \frac{\gamma_0\sqrt{1+s}}{\frac{\omega_0}{c}\sqrt{\frac{2k_BT}{M}}}N_{tot} \tag{4.17}$$

Using reasonable experimental values for temperature (2 K) and laser power (s$\sim 10^8$) this

expression becomes

$$\delta N \sim 0.01 N_{tot} \tag{4.18}$$

While this is a small fraction of the total atoms produced during ablation. The number of atoms excited to the metastable $^3P_1$ state is a factor of 10 larger than the number of molecules produced during ablation. We were able to observe an effect of the enhancement laser under these conditions as shown in Figure 4.12 and Figure 4.11.

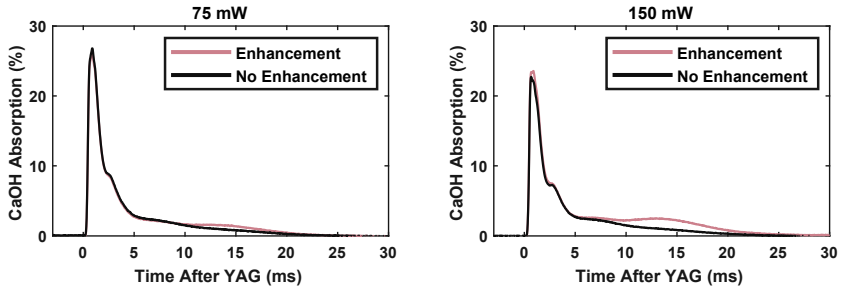

Figure 4.12: In-cell enhancement with 75 mW (left) and 150 mW (right) of enhancement light.

The enhancement is more pronounced in the cell compared to molecular beam and there is a clear increase in enhancement signal as the excitation light is applied for longer duration and at higher powers. However, this effect is small, enhancing the molecular beam signal by only a few percent. If we extrapolate this enhancement and assume we can excite all of the atoms to the metastable state this would translate to a factor of 2-5 increase in molecular signal. Experimental efforts in Yb enhancement indicate that there is another factor of unity that may be gained by applying the excitation light in a different location in the buffer gas cell [189].

Given the technical limitations and insignificant enhancement we did not pursue this further. The magnitude of the enhancement is larger at long times, suggesting that it may preferentially enhance slow molecules. This possibility should be explored when attempting to slow the molecular beam.

4.6 Velocity sensitive detection

In order to determine the forward velocity distribution of our cryogenic buffer-gas beam, we rely on Doppler-sensitive laser-induced fluorescence. One of the detection lasers propagates towards or against the direction of particle motion. As a result the Doppler-shifted laser frequency only comes on resonance when the detuning of the laser compensates for the Doppler shift. This Doppler shift is proportional to the particle velocity and allows us to map a frequency shift onto a velocity. The Doppler shift is described by:

$$\Delta f = \frac{v\,\mathrm{Cos}\theta}{\lambda} \tag{4.19}$$

Where Δf is the Doppler shift, v is the velocity of the particle, θ is the angle between the velocity vector and the laser propagation direction, and λ is the wavelength of the laser light.

The signal from Doppler-sensitive detection is reduced an order of magnitude compared to transverse detection. For atomic beams this does not pose a issue but for molecular beams this poses a significant limit to signal to noise. As a result, we use off diagonal photon counting which allows for sensitive detection of photons emitted by the molecules with simultaneous rejection of the laser light used to excite the molecules.

4.7 A cold slow beam of CaOH

One key parameters of our buffer gas beam that affects our ability to laser cool is the forward velocity distribution. While cryogenic buffer-gas beams offer slow, bright sources of molecular radicals, cell geometry plays a significant role in determining the forward velocity distribution [176]. Characterizing the forward velocity is important when optimizing our source for its intended use of loading a 3D magneto-optical trap (MOT). Recent diatomic MOTs have

slow capture velocities compared with atomic MOTs, typically $\leq$ 10 m/s [191, 14]. Estimates of the capture velocity for a MOT of CaOH are $\sim$ 7 m/s [192]. Sources of cold molecules typically have significantly higher velocities, which necessitates the use of slowing techniques. For molecules, these slowing techniques are typically inefficient compared to atoms and thus small adjustments in the velocity profile of a molecular source can have dramatic effect on the number of molecules available in a MOT [14, 183]. Buffer gas beams have significantly higher flux compared to other sources of cold molecules and are used ubiquitously for molecular laser cooling experiments [167].

Our initial cell design replicated the cell designed for optical loading [89] and later used in experimental work in laser cooling CaF molecules [14, 193]. We varied an number of cell parameters, optimizing the signal and velocity profile of a Ca beam, taking advantage of the high single to noise of atomic beams. Ultimately, for the work described in this thesis, we used the cell design presented in Section 3.3.1. This cell design produces a cold calcium atomic beam with a velocity profile shown Figure 4.13 with a peak forward velocity of $\sim$ 80 m/s and a spread of $\sim$50 m/s (FWHM). The same source produces a slightly faster cold CaOH beam with a peak velocity of $\sim$ 85 m/s and a similar velocity spread .

While the molecular beam produced by a two-stage buffer gas cell offers incredibly slow velocity distributions, a single stage buffer gas cell can offer a slightly faster but significantly brighter beam, often with an order of magnitude increase in flux. This additional signal is useful when performing spectroscopy of CaOH molecules [167].

Using calcium atoms for characterization, we found that a single stage beam source increased the beam flux by the expected factor of 5-10 [167]. We also measured a concomitant increase in forward velocity from $\sim$ 80 m/s to $\sim$ 125 m/s. This increase in velocity is due to boosting of the atoms by collisions with helium that preferentially occur from behind [176]. A comparison of the velocity distributions from both cell designs is presented in Figure 4.14.

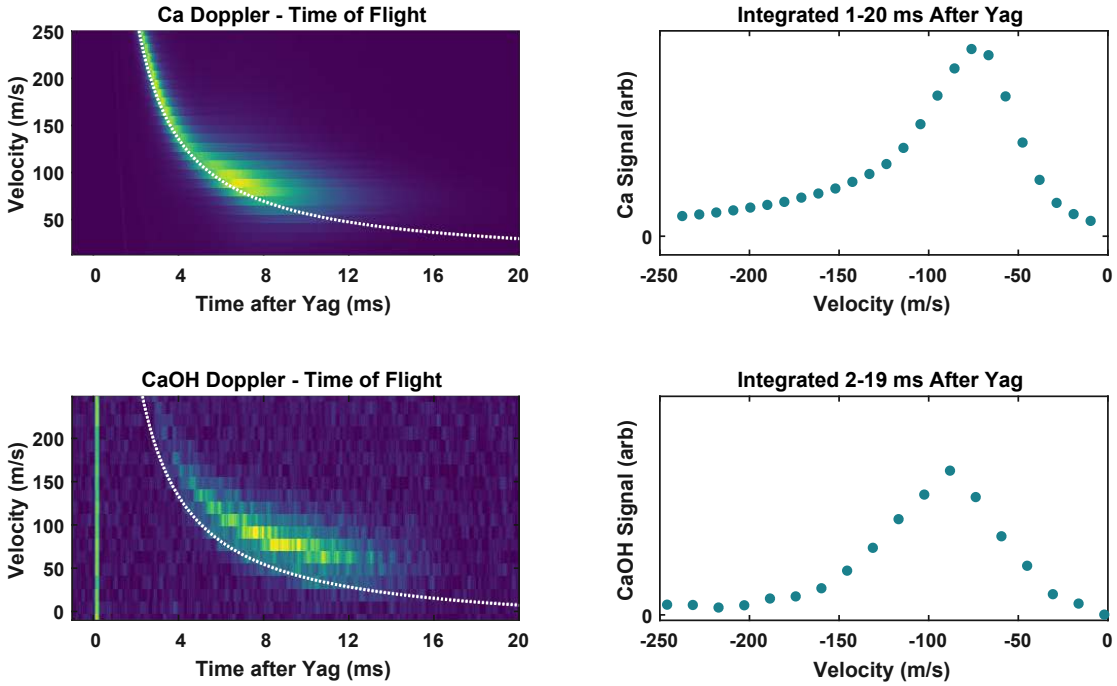

Figure 4.13: (top) Calcium atomic beam data. (bottom) CaOH beam data. (left) Velocity vs Time-of-flight spectrum.(right) Beam velocity distribution integrated over time. Atomic data collected by exciting the atoms on the $^1S_0$ to $^1P_0$ transition by driven by a laser counter propagating to the molecular beam at an angle of 27 degrees. Molecular data collected by optically pumping molecules into the $\widetilde{X}(100)$ vibration state in the detection region while scanning the velocity sensitive the $\widetilde{X}(100) \rightarrow \widetilde{B}(000)$ repumping transition by driven by a laser counter propagating to the molecular beam. Photons produced by the spontaneous decay of the $\widetilde{B}(000)$ state can be spectroscopically filtered from background light for high signal to noise. The white dotted line indicates ballistic motion of a particle generated at the cell 0.5 ms after the YAG ablation and serves as a guide to the eye.

4.8 A surprisingly fast beam of CaOH

When we measured the forward velocity of the CaOH molecular beam produced with a single stage source we found that the molecules were dramatically faster than the calcium atoms. This is illustrated in the velocity scan shown in Figure 4.15. The first model we tested to explain this anomalously fast beam was the use of methanol in the chemical source. It was thought that the presence of methanol ice within the cell could prevent thermalization of

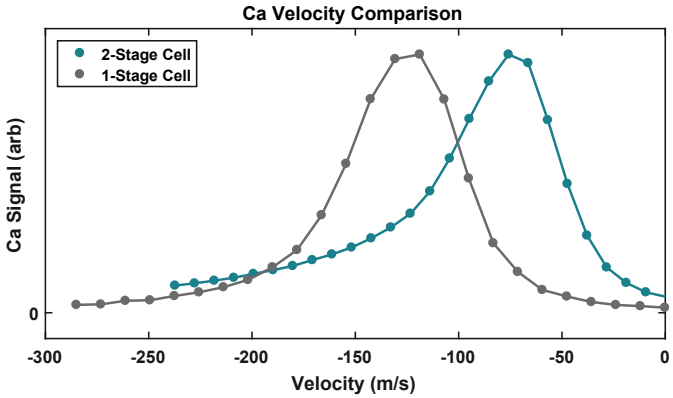

Figure 4.14: Comparison of the velocity profile of calcium beams produced with single stage and 2-stage buffer gas cells. The distributions have been normalized for comparison.

CaOH molecules. While the temperature of the molecules can be extracted from Doppler scans of the in cell signal, this method is known to produce unreliable results. In previous work, Doppler temperatures extracted from in cell measurements indicated temperatures higher than other methods [174]. We conducted rotational temperature measurements in order to determine if the molecules are thermalizing with the buffer gas. These measurements are shown in Figure 4.16 and confirm that the rotational degree of freedom thermalizes to cell temperatures.

4.8.1 Beam attenuation through He collisions

Another model to explain the high forward velocity is a build up of pressure somewhere along the beam line, leading to collisions attenuating the molecular beam. These collisions would have to preferentially effect slower molecules. Studies of helium-helium collisions at low temperatures indicate an increase in total effective cross section at low velocities [194]. We would expect similar behavior for the CaOH - He cross section. If collisions are modifying the velocity distribution we would expect to measure different velocity profile at the exit of the

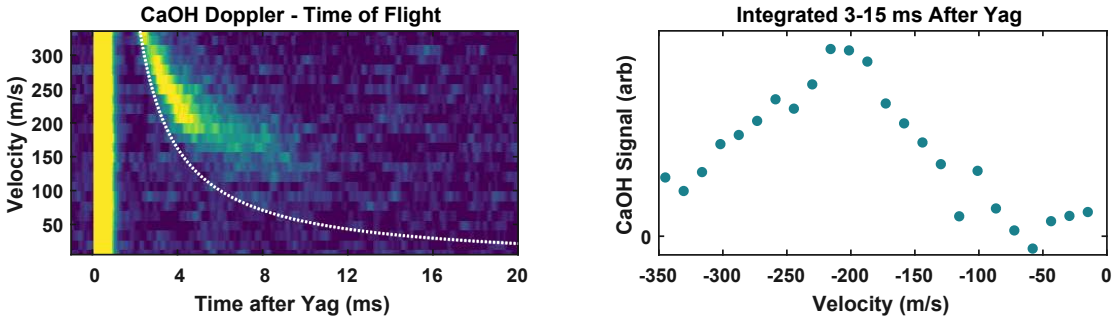

Figure 4.15: (left) CaOH Doppler vs. time of flight spectrum. Data collected by optically pumping molecules into the $\widetilde{X}(100)$ vibration state in the detection region while scanning the velocity sensitive the $\widetilde{X}(100) \rightarrow \widetilde{B}(000)$ repumping transition. Photons produced by the spontaneous decay of the $\widetilde{B}(000)$ state can be spectroscopically filtered from background light for high signal to noise. The white dotted line indicates ballistic motion of a particle generated at the cell 0.5 ms after the YAG ablation and serves as a guide to the eye. (right) CaOH beam velocity distribution integrated from 3 to 15 ms after YAG ablation. Note the peak at $\sim$ 200 m/s.

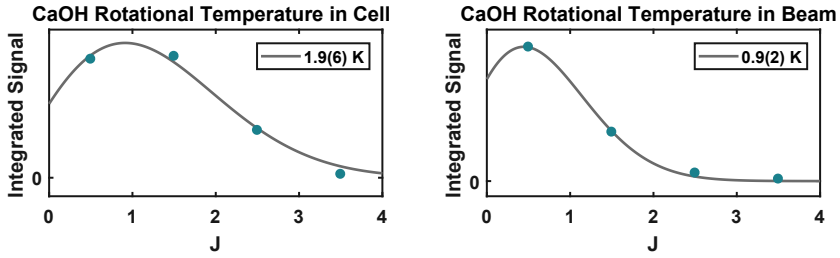

Figure 4.16: Rotational Temperature of a CaOH beam both inside of the buffer gas cell cell (left) and in the cryogenic buffer-gas beam (right). In-cell temperatures are consistent with full thermalization and lower temperature in the beam indicates possible cooling by adiabatic expansion as the beam leaves the buffer gas cell.

cell.

By directing a laser addressing the $\widetilde{X}^2\Sigma^+(000) \rightarrow \widetilde{A}^2\Pi_{1/2}(000)$ transition counter propagating to the molecular beam directly into the cell we were able to detect fluorescence from the molecules directly outside of the buffer gas cell with an EMCCD camera. Though scattered light was significant, background subtraction allowed us to observe molecular signal. We were then able to detect fluorescence vs. laser detuning and map out the velocity profile of molecules approximately 1 cm after the cell exit. It is known that the velocity distribution of

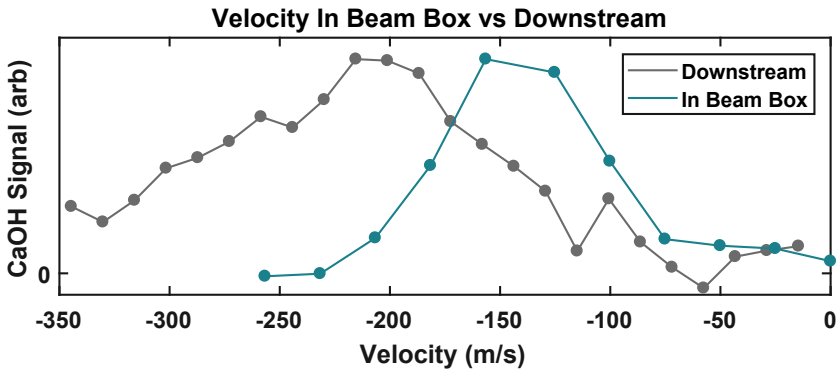

Figure 4.17: Measurement of the velocity inside of the 4 K region of the beam box (blue) vs velocity distribution measured downstream (grey). The distributions have been normalized for comparison. This indicates substantial loss of low velocity molecules. This is strong evidence pointing to a build up of helium inside of the 4 K region leading to collisional attenuation of the buffer gas beam which would preferentially remove slow moving molecules.

molecules and atoms is boosted to higher velocities by collisions with He as the beam exits the buffer gas cell, this boosting effect stabilizes $\sim$ 1 cm from the cell exit [89, 176]. Figure 4.17 displays the velocity distribution measured 1 cm from the cell exit and the velocity distribution measured downstream. The clear difference confirms the attenuation of slow molecules.

4.8.2 Improvement and resolution

Pressure measurements in the room temperature regions of the vacuum system indicated pressures of 0.5 to 5 $\times$ 10^{-7} Torr when flowing 0 to 10 sccm of He buffer gas, which is sufficient to prevent unwanted collisions. This directed us to explore a build up of helium inside of the cryogenic region. We modeled the flow of of He buffer gas given our particular geometry (results shown in Figure 4.18), we determined that there was build up of helium between the cell and the aperture in the 4 Kelvin shield. Estimates of He pressure range from $\sim 5\times10^{-6}$ to 10^{-5} Torr. This helium build up, specifically the helium counter propagating to the molecular beam, was likely responsible for the attenuation of low velocity molecules.

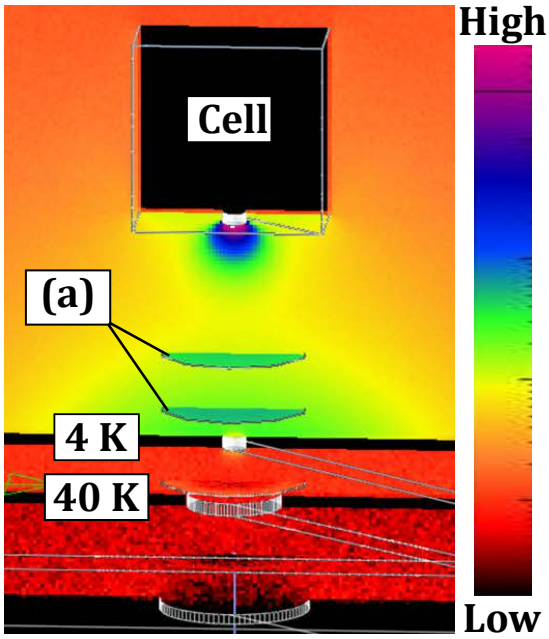

Figure 4.18: Color map of helium pressure inside of the 4 K shields. Semi-circular sections labeled (a) indicate helium counter propagating to the molecular beam. Estimates of He pressure range from $\sim 5\times10^{-6}$ to 10^{-5} Torr which are high enough to cause significant beam attenuation.

In order to reduce the helium density near the 4 Kelvin aperture, we made several changes to the vacuum system:

- We moved the cell further away from the 4 K surface.
- We added additional sorbs surrounding the 4 K aperture (see Figure 4.19)
- We added protected sorbs to the outside of the 4 K shield.

After these changes were made we took a series of velocity scans at different He buffer gas flow rates. These scans are shown in Figure 4.20. As the helium buffer gas flow is reduced we see a growth of the low velocity signal. This trend indicates that we are limited by He buffer gas build up inside of the 4 Kelvin section. The trend continues even at very low flows (0.5 sccm) and as a result we conclude that further reduction of the buffer gas would continue to

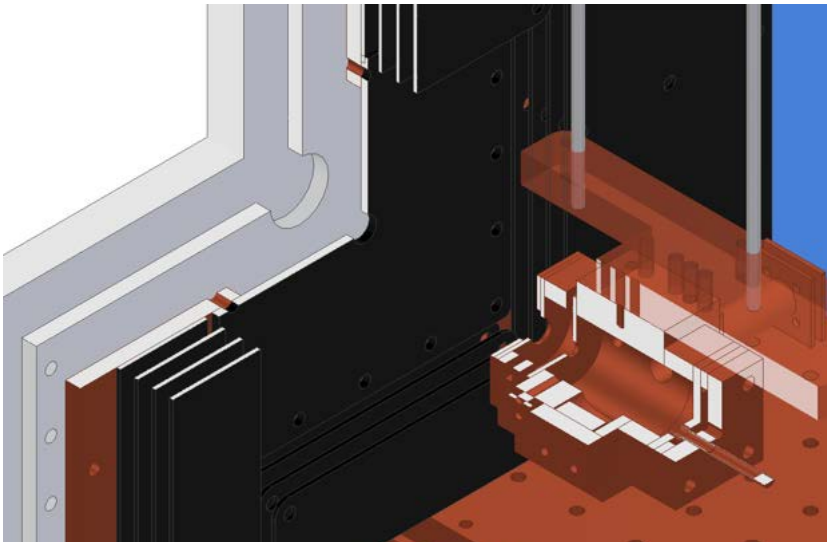

Figure 4.19: Here we see a cut away view of the two-stage buffer gas cell, shields and the sorbs surrounding the 4 K exit aperture. The multiple layers provide protected sorb as well as significantly increase the surface area for cryo pumping. Surfaces colored black are coated with charcoal to improve cryopumping.

be beneficial for the molecular beam. There are several methods we could have used to maintain buffer gas density inside the cell while reducing the helium density along the beam line, including a conical skimmer, additional distance between the cell exit and the 4 K shield, or reduction in the size of the cell exit aperture. We decided to circumvent this issue by going back to a 2-stage buffer gas cell. In a two-stage configuration, the second stage redirects helium flow away from the direction of beam propagation such that it reduces the He density by an order of magnitude near the 4 K aperture, side stepping the issue.

It should be noted that previous buffer gas beam sources use similar distances from the cell exit to the 4 K aperture without apparent issues. One of these sources produces YbOH using chemical production with methanol another produced SrOH using ablation of $Sr(OH)_2$. It is suspected that the higher mass of these species makes them less susceptible to attenuation through He collisions. A chemical source producing CaF does not show this attenuation effect.

There, the distance between the cell and 4 K aperture is $\sim$6", corresponding to a reduction of He by a factor of 4. Taken together these data points indicate that typical buffer gas sources operate in a regime where problems may arise from changing the density of He in front of the cell by a factor of unity. These problems can be mitigated with changes to experimental geometry, especially having sufficient distance between the cell and 4 K aperture. The details of this helium build up remain to be elucidated by a future detailed study.

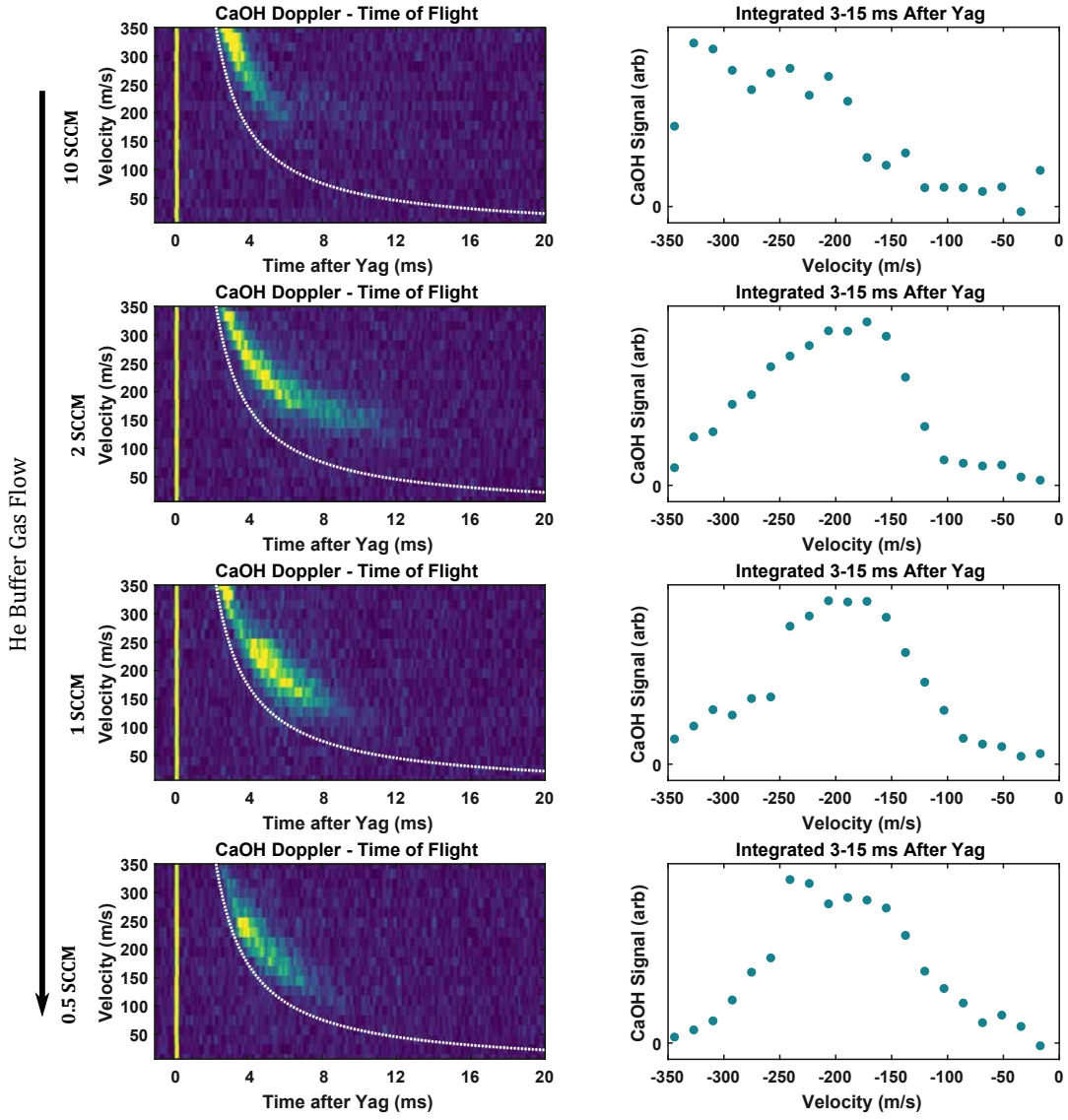

Figure 4.20: Downstream CaOH beam velocity as a function of He buffer gas flow. This is after installation of charcoal sorbs and moving the cell exit away from the 4 K aperture to lower helium buildup inside of 4 K region. As the helium flow is reduced molecular signal at low velocity classes increases. Note this data is normalized.

5

Laser manipulation of CaOH

Laser manipulation of both internal and external degrees of freedom for neutral atoms [2], molecules [195, 20], and microscopic objects [196, 197, 198, 199] has revolutionized atomic molecular and optical physics. In most cases, these manipulations are based on a resonant interaction between the quantum system and the light field to change the internal state of the quantum system in a well controlled manner. Many of these interactions are due to a momentum change in the system, where upon absorption of a photon of wavelength λ, the momentum p of the quantum object changes by $\Delta p = \hbar k = \hbar c/\lambda$. The system can return to its original state through emission of the photon, which carries its own momentum change. Over many cycles the momentum change due to spontaneous emission averages to zero. The momentum change from a single photon, while measureable [200], is small and to achieve significant

changes to the motion of the system this process is repeated many times. In order to bring a beam of CaOH moving at 100 m/s, to near the capture velocity of a MOT will requires 10^4 photon-emission cycles .

The complex internal structure of molecules, while rich with applications, makes cycling many photons difficult as spontaneous emission leads to decay to a large number of distinct grounds states. Recent advances in laser cooling show great promise for several diatomic species (e.g. SrF [201, 20, 122, 107, 202, 203, 204], CaF [123, 147, 21, 108, 205, 125, 206], and YO [23, 124, 106]), and the extension to larger species has been demonstrated for a few molecules (e.g. SrOH [148],YbOH [32], and CaOCH3 [70]) further complicated by the concomitant vibrational and rotational modes. In this chapter we demonstrate photon cycling of CaOH, perform radiation force deflection, and characterize the photon scattering rate. Photon cycling allows for greatly enhanced molecular detection, and the resulting radiation pressure force enables state-selective deflection and the extension to longitudinal beam slowing.

5.1 Photon cycling of CaOH

In order to construct a quasi-closed photon cycling scheme, it is necessary to prevent rotational branching. The rotational structure of CaOH is described in detail in Section 2.4 and the relevant energy levels are shown in Figure 5.1. We replicate previously developed schemes that were successful in diatomics and triatomic work [23, 22, 126, 201, 123, 207, 32, 192], addressing the first excited rotational state using the $P(N'' = 1)$ branch. A combination of rotational selection rules causes molecules to return to the original rotational state . There is additional structure due to the spin-rotation interaction, this causes the $P(N'' = 1)$ line to split into the $P_{11}(J'' = 3/2)$ and ${}^{P}Q_{12}(J'' = 1/2)$ lines 52 MHz apart. The nuclear spin on the hydrogen creates additional hyperfine splitting, but this below the natural linewidth of the

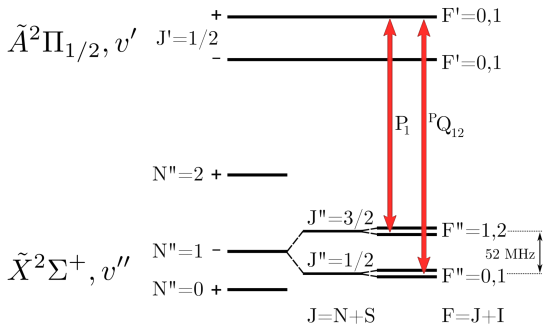

Figure 5.1: Rotational structure of CaOH illustrating the 52 MHz spin-rotation splitting in the electronic ground state as well as the unresolved hyperfine structure (1.5 MHz and 7 kHz in the $J'' = \frac{3}{2}$ and $J'' = \frac{1}{2}$ states respectively [142]). The $\widetilde{X}^2\Sigma^+(v_1''v_2''v_3'') \rightarrow \widetilde{A}^2\Pi_{1/2}(v_1'v_2'v_3')$ $P_1(J'' = \frac{3}{2})$ and $^PQ_{12}(J'' = \frac{1}{2})$ rotationally closed transitions are shown [126]. The parity of the ground states is indicated by the sign to the right of the N'' value while the parity of the excited states is indicated to the right of the J' value. The rotational structure of the $\widetilde{B}^2\Sigma^+(000)$ state is analogous to that of the $\widetilde{X}^2\Sigma^+$ states and is not pictured. Rotational closure on repumping lines through this state is achieved by driving $P_1(J'' = \frac{3}{2})$ and $^PQ_{12}(J'' = \frac{1}{2})$ transitions to the $\widetilde{B}^2\Sigma^+(N' = 0, J' = \frac{1}{2}, +)$ state. The level diagrams are not to scale.

electronic transition [142] and therefor neglected.

Experimentally, we can observe photon cycling by detecting the laser induced fluorescence from CaOH molecules as a function of detuning as we scan two laser frequencies. This is shown in Figure 5.2, where the leftmost peak occurs when only the $P_{11}(J'' = 3/2)$ transition is on resonance, the rightmost peak occurs when only the $^PQ_{12}(J'' = 1/2)$ line is on resonance, and the large center peak occurs when both transitions are simultaneously addressed. We observe a dramatic increase in signal when we close the rotational degree of freedom. Molecules excited on either the $P_{11}(J'' = 3/2)$ or $^PQ_{12}(J'' = 1/2)$ lines scatter on average 2 photons before decaying to the other spin-rotation state. If both spin-rotation states are addressed molecules will scatter photons until they decay into a dark vibrational state, corresponding to ~ 22 photons in CaOH [150].

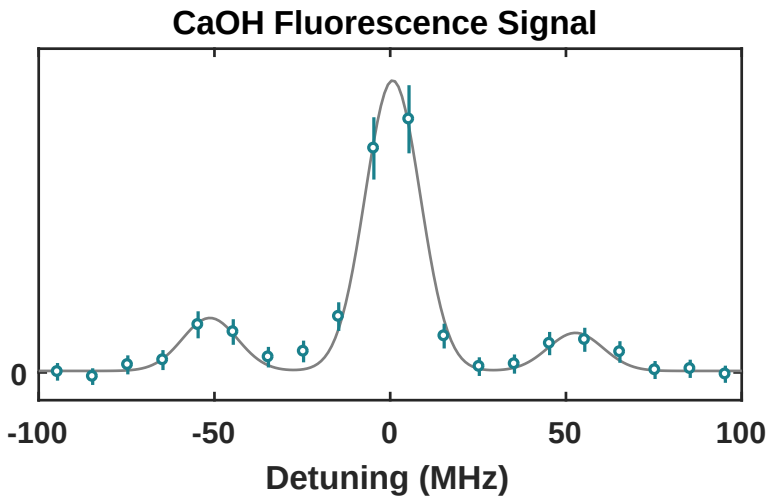

Figure 5.2: In-beam fluorescence spectrum of $\widetilde{X}^2\Sigma^+(000) \rightarrow \widetilde{A}^2\Pi_{1/2}(000)$ transition in CaOH. Two laser frequencies split by the spin-rotation splitting (52 MHz) are scanned across two transitions. The leftmost peak occurs when only the $P_{11}(J'' = 3/2)$ transition is on resonance, the rightmost peak occurs when only the ${}^PQ_{12}(J'' = 1/2)$ line is on resonance, and the large center peak occurs when both transitions are simultaneously addressed.

5.2 Experimental configuration

Once we have closed the rotational degree of freedom, the next step in extending our photon cycling scheme is to repump molecules that decay to other vibrational states in the $\widetilde{X}$ electronic manifold. In order to confirm that we are optically pumping molecules into higher vibrational states we constructed a beam line with three distinct regions with optical access as shown in Figure 5.3. The first region, the "interaction region", will allow us to apply lasers to manipulate the momentum of the molecules or optically pump them into a different internal quantum state. The second region, the "clean up region", will allow us to apply repumping

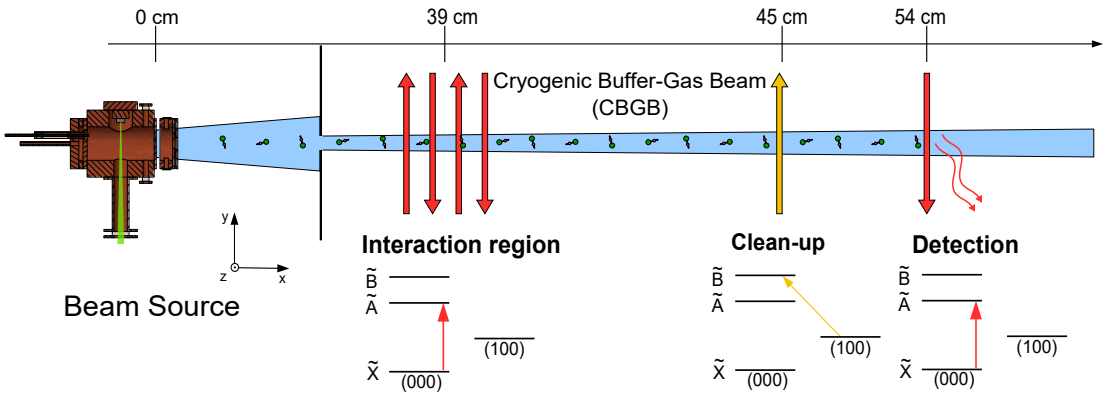

Figure 5.3: Depletion-Revival experimental configuration

lasers to recover population lost to dark vibrational states. The third region, the "detection region", is used to detect molecular population in a state selective manner. This experimental apparatus is useful with minor modifications for a number of experiments, including radiation pressure force, laser cooling, or vibrational spectroscopy.

In the initial test, we apply the main cooling laser ($\widetilde{X}^2\Sigma^+(000) \rightarrow \widetilde{A}^2\Pi_{1/2}(000)$) to optically pump molecules from the $\widetilde{X}^2\Sigma^+(000)$ state into the $\widetilde{X}^2\Sigma^+(100)$ state. Then apply the first repumping laser ($\widetilde{X}^2\Sigma^+(100) \rightarrow \widetilde{B}^2\Sigma^+(000)$) to recover the lost population. The results of this test are summarized in figure Figure 5.4. The trace in grey indicates the baseline signal from unperturbed molecules in the $\widetilde{X}^2\Sigma^+(000)(N'' = 1)$ state. If we apply the main cycling laser in the interaction region, we observe the pink trace corresponding to a complete loss of molecular population. This confirms that we are optically pumping molecules out of the $\widetilde{X}^2\Sigma^+(000)(N'' = 1)$ state. If we apply the main cycling laser in the interaction region and the first repumper in the clean up region, we observe the blue trace. This configuration recovers $\sim$ 90% of the molecular population, which is consistent with the expected branching ratios.

Higher order vibrational states can be repumped in a similar manner to confirm the recovery of molecular population. In addition, this depletion-revival signal can be used as a pow-

erful spectroscopic tool to find vibrational repumping transitions and characterize branching ratios as outlined in Chapter 6.

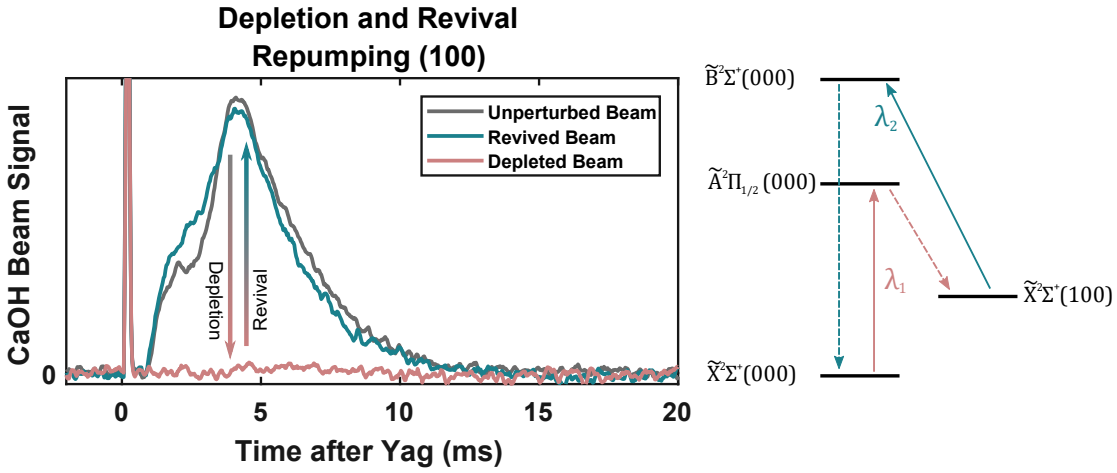

Figure 5.4

5.3 Radiation pressure force

Once we have determined that we are recovering the population from higher vibrational states, we can characterize photon cycling in the CaOH molecular system through the resulting radiation pressure force. The number of photons scattered can be determined by observing the magnitude of momentum shift in the molecules and the scattering rate can be extracted by varying the spatial extent of the laser light in combination with measurements of the velocity distribution of the molecular beam. Before presenting experimental results, we will summarize the theory of radiation pressure force in molecular systems. In atomic systems it is straightforward to isolate two quantum states that are well described as an effective two-level system; however, in order to prevent rotational branching, diatomic and linear triatomic systems generically rely on $J'' \rightarrow J' = J'' + 1$ type transitions where a two-level system model is not adequate. This complication does not originate from the vibrational degree of freedom, but

from the angular momentum resulting from rotation. A key conclusion from this summary is that the presence of additional ground states significantly reduces the scattering rate in molecular systems compared with effective two-level systems.

5.3.1 Radiation pressure force in a two-level system

A rigorous derivation of the radiation pressure force is available in chapter 3 of ref. [208], however it can be intuitively derived from Newton's 2*nd* law:

$$F = -\frac{dp}{dt} \tag{5.1}$$

The force (F) from scattering photons from the light field is the change in momentum from scattering a single photon ($\hbar k$) multiplied by the scattering rate (R_{sc}):

$$F = \hbar k \, R_{sc} \tag{5.2}$$

The scattering rate in a two-level system as rest is [209]:

$$R_{SC} = \frac{\gamma}{2} \frac{s_0}{1 + s_0 + 4(\delta/\gamma)^2} \tag{5.3}$$

Where we have introduced the several parameters — the saturation parameter s_0, the decay rate due to spontaneous emission $\gamma = 1/\tau$ (τ is the lifetime of the excited state), the Rabi frequency Ω, and the detuning from resonance δ.

The saturation parameter and saturation intensity for a two-level system are defined below. These are useful experimental parameters when comparing different species of atoms and molecules.

$$s_0 = \frac{I}{I_{sat}} \tag{5.4}$$

$$I_{sat} \equiv \frac{\pi hc}{3\lambda^3 \tau} \tag{5.5}$$

The Rabi frequency quantifies the strength of the coupling in a two-level system and how it relates to the light field (E_0). It is also the rate at which population is excited from the ground state to the excited state when the light field is on resonance. It is defined as:

$$\Omega \equiv \frac{eE_0}{\hbar} \langle e | \vec{d} | g \rangle \tag{5.6}$$

Where $\langle e|$ and $|g\rangle$ denote excited and ground states respectively. Incorporating Eq. 5.3 into Eq. 5.2 we arrive at:

$$F = \frac{\hbar k \gamma}{2} \frac{s_0}{1 + s_0 + 4(\delta/\gamma)^2} \tag{5.7}$$

For large laser powers (s » 1) the fraction on the right approaches 1 and the maximum force is limited only by the inherent spontaneous emission rate of the transition.

5.3.2 Radiation force in a multilevel system

In CaOH, the inverted angular momentum structure ($J'' \rightarrow J' = J'' + 1$) of the rotationally closed cycling transition couples multiple ground states to multiple excited states. The state multiplicity can be accounted for with minor changes to the expressions describing the two-level system. Modifying the expressions for scattering rate, saturation parameter, and saturation intensity as shown in ref. [203] permits accurate modeling of diatomic systems (e.g.

SrF and CaF). The expression for scattering rate in a multilevel system is

$$R_{sc} = \gamma \frac{n_e}{(n_g + n_e) + 2\sum_{j=1}^{n_g}(1 + 4\Delta_j^2/\gamma^2) I_{s,j}/I_j} \tag{5.8}$$

where I_j is the intensity of light addressing transition j and $I_{s,j}$ is the saturation intensity. Under the assumption that the scattering rate is dominated by the main cycling transition, and all transitions are driven with the same intensity, equally divided between transitions, this expressions simplifies to:

$$R_{sc}(\delta) = \frac{\gamma_{eff}}{2} \frac{s_{eff}}{1 + s_{eff} + 4(\delta/\gamma)^2} \tag{5.9}$$

Where γ_{eff} and s_{eff} are defined as:

$$\gamma_{eff} = \frac{2n_e}{n_g + n+_e} \gamma \tag{5.10}$$

$$s_{eff} = \frac{2(n_g + n_e)}{n_g^2} \frac{I}{Is} \tag{5.11}$$

The modified definition for s_{eff} leads to a modified saturation intensity given by:

$$I_{sat,eff} = \frac{2(n_g + n_e)}{n_g^2} I_{sat} \tag{5.12}$$

These expressions simplify to the expressions for a two level system if $n_e = n_g = 1$. The above framework is general to all multilevel systems, for CaOH in particular the unresolved hyperfine levels must be taken into account in order to satisfy the assumption that all levels are driven with the same intensity. For the main cycling transition of CaOH $n_e = 4$ and $n_g = 12$. If additional vibrational states are coupled to the same excited state, the number

of ground states must be increased to reflect the additional states. It should be clear that from these expressions that when compared to an atomic transition, multilevel systems have a significantly reduced scattering rate, which corresponds to a lower radiation pressure force. This reduced scattering rate also leads to reduced damping forces for laser cooling and magneto-optical trapping.

5.4 Scattering rate measurement

To fully characterize the photon cycling in CaOH, not only do we demonstrate that we can recover population lost to higher order vibrational states but we also want to confirm that we can cycle photons rapidly. The photon scattering rate controls how quickly one can manipulate the momentum of a molecular sample. This is particularly significant for laser slowing where the photon cycling rate defines the required slowing distance. In this section we measure the scattering rate in two ways. Both tests require knowledge of the molecular beam velocity distribution, which we have measured as described in section Section 4.7. These measurements are described below.

5.4.1 Experimental configuration

The first measurement relies on measuring the deflection of the molecular beam due to radiation pressure force. In the interaction region, deflection lasers are applied to impart momentum on the molecular beam, as the beam propagates to the detection region this momentum is mapped on to the spatial extend of the molecular beam. The cleanup region has minimal effect on the momentum of the molecular beam, but allows us to apply vibrational repumpers lasers to optically pump molecules into states that are addressed by the detection light. In the detection region we image the molecular beam on an emccd camera. To extract an average

deflection, we fit the beam to a Gaussian distribution and note the fit center. The vibrational states addressed in the interaction, clean up and detection region are indicated in the experimental configuration diagram in Figure 5.5.

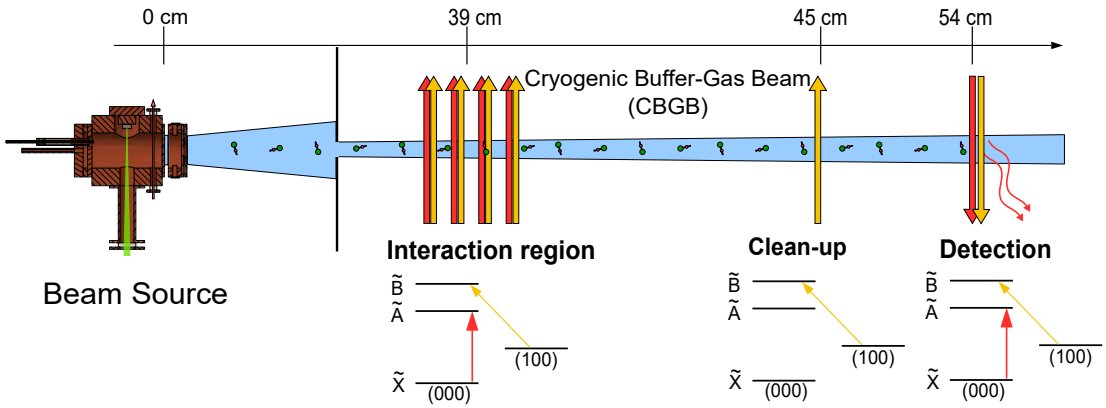

Figure 5.5: Deflection experimental apparatus.

We calibrate the deflection by measuring the deflection using only the main cycling laser. Based on the measured Franck-Condon factors [150], this deflection corresponds to scattering ∼22 photons. The results of this deflection measurement are summarized in Figure 5.6. The integrated beam profiles are shown on the left with an arrow indicating the direction of deflection, these profiles have been normalized for comparison. The number of photons scattered in each case as a function of interaction length is shown on the right with a fitted line corresponding to a scattering rate of 1.5×10^{6} s^{-1} superimposed on the data. As more photons are scattered, some molecules are lost to higher vibrational states that are not repumped, this results in the change in signal to noise seen on the beam profiles.

The second measurement only requires the detection region. We image the laser induced fluorescence as a function of distance. To ensure a flat laser intensity across the field of view, we expand the detection laser before aperture it to 12.4 mm x 11.4 mm. As the molecules scatter photons, they are optically pumped into excited vibrational states with branching ratios

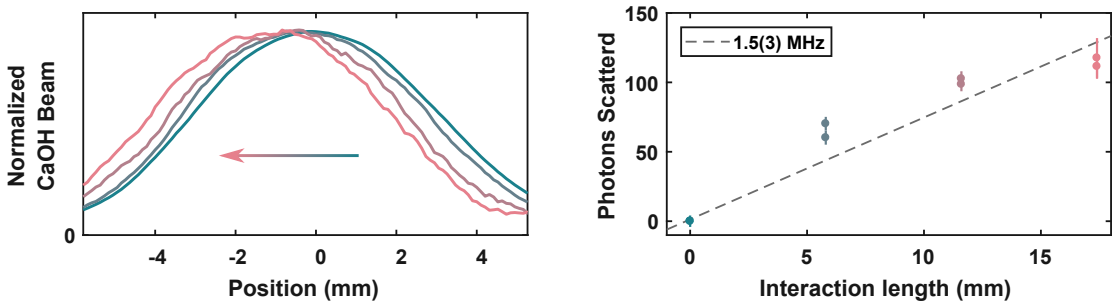

Figure 5.6: (left) Normalized integrated CaOH beam profiles that have been deflected, Arrow indicates direction of deflection and color indicates the length of interaction with the deflection lasers as shown in the right panel.(right) Extracted deflection vs interaction distance, fitted line corresponding to a scattering rate of 1.5×10^6 s^{-1} is superimposed on the data.

defined by the Franck-Condon factors. This exponential decay can be observed in the spatial fluorescence distribution. The length scale of this exponential decay is extracted from a fit to the data, and in combination with knowledge of the beam velocity the scattering rate can be extracted. We measured the scattering rate when only the main cycling laser is applied and when both the main and 1^{st} repumper are applied, the results are shown in Figure 5.7. For this data the beam velocity is measure to be $\sim$ 210 m/s, this leads to extracted scattering rates consistent with the deflection measurement of $\sim 1.5\times10^6$ s^{-1}.

The resulting scattering rate is a factor of $\sim$ 6 below the maximum scattering rate expected for the CaOH system based on the lifetime of the excited $\widetilde{\text{A}}$ state. We attribute this lowered scattering rate to imperfect remixing of dark states, noting that the measured scattering rate is consistent to scattering rates achieved in similar diatomic systems [14, 123].

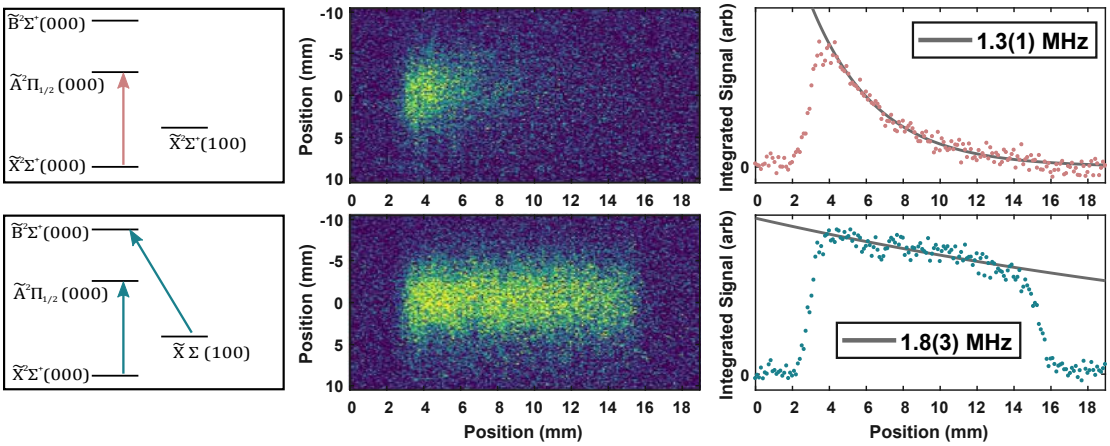

Figure 5.7: (left) Lasers present in the detection region. (center) EMCCD image of laser induced fluorescence from CaOH molecules. (right) Integrated fluorescence as a function of distance, exponential fits are labeled with the extracted scattering rate based on known Franck-Condon factors [150].

6

Unexpected vibrational branching and Franck-Condon factor measurements

In the process of building a photon cycling scheme for CaOH molecules, we determined that our experimental measurements indicated an unexpected loss of molecules that exceeded estimates based on calculations and previous measured Franck-Condon factors [150]. This was particularly insidious as the magnitude of loss was similar to the experimental error in many of our measurements. This chapter will present the measurements that indicated an unexpected loss of molecules, identification of the loss channel, and a mechanism that explains the loss. Once we had identified the mechanism responsible for the loss, we conducted mea-

surements of vibrational branching ratios in our photon cycling scheme.

6.1 Evidence for molecular population loss

The evidence that indicated we were experiencing unexpected molecular loss is based on depletion-revival measurements taken with different repumping lasers. These depletion-revival measurements are an extension of the work described in Section 5.2, but conducted with higher order repumpers. In short, there are three experimental sections where lasers interact with molecular beam. In the first section, molecules cycle photons and are optically pumped into higher vibrational states. Next, vibrational repumpers are applied to recover lost population. Finally, detection lasers are applied and the molecular population is measured. To understand the expected results one must know the expected branching ratios based on measured and calculated Franck-Condon factors.

6.1.1 Measured and calculated Franck-Condon factors

The Franck-Condon factors of CaOH's excited $\widetilde{\mathrm{A}}(000)$ and $\widetilde{\mathrm{B}}(000)$ states have been measured previously with dispersed fluorescence techniques [150]. The data available from these measurements has a noise floor at $\sim 2\times10^{-3}$ level. Below this level, we rely on the Sharp-Rosenstock GF matrix method to calculate Franck-Condon factors for CaOH [167, 210]. Table 6.1 summarizes the measured and calculated Franck-Condon factors for the $\widetilde{\mathrm{A}}(000)$ state and the $\widetilde{\mathrm{B}}(000)$ state of CaOH.

Table 6.1: Calculated and observed Franck-Condon factors for CaOH from excited electronic states.

	Excited State : $\widetilde{A}(000)$		
Ground State $\widetilde{X}$	Calculated FCF[1]	Calculated VBR	Observed VBR [150]
(000)	0.9521	0.9570	0.957 ± 0.002
(100)	0.0459	0.0410	0.043 ± 0.002
(200)	1.8×10^{-3}	1.3×10^{-3}	2×10^{-3}
(001)	2×10^{-5}	7×10^{-6}	-
(02^00)	3×10^{-4}	3×10^{-4}	$3^{+1}_{-2}\times10^{-3}$
(02^20)	-	-	-
(01^10)	-	$[2\times10^{-4}]^2$	-
(300)	5×10^{-5}	4×10^{-5}	-
(12^00)	1.5×10^{-5}	1×10^{-5}	-
(12^20)	-	-	-

	Excited State : $\widetilde{B}(000)$		
Ground State $\widetilde{X}$	Calculated FCF[1]	Calculated VBR	Observed VBR [150]
(000)	0.9711	0.9742	0.975 ± 0.001
(100)	0.0270	0.0244	0.022 ± 0.001
(200)	1.5×10^{-4}	1.3×10^{-4}	-
(001)	5×10^{-6}	3×10^{-6}	-
(02^00)	1.3×10^{-3}	1.2×10^{-3}	-
(02^20)	-	-	-
(01^10)	-	-	$.003 \pm 0.001$
(300)	2×10^{-8}	5×10^{-8}	-
(12^00)	3×10^{-4}	3×10^{-4}	-
(12^20)	-	-	-

[1] These calculations use the Sharp-Rosenstock Method [210], which obey the nominal vibrational angular momentum selection rule ($\Delta l = 0$) [137].
[2] Prediction described in Section 6.2.1

6.1.2 Markov chain analysis

The laser cooling scheme proposed for CaOH in Section 2.5.2 and shown again in Figure 6.1 attempts to maximize scattering rate by avoiding, where feasible, Λ-type systems linking mul-

tiple ground states to the same excited state. As discussed in Section 5.3.2 Λ-type systems increase the number of ground states and decrease the maximum scattering rate attainable for the system. As a result, the branching ratios from our laser cooling scheme do not correspond directly to the vibrational branching ratio from a single electronic state but rather a weighted combination all excited states used in the laser cooling scheme. In order to model the population transfer in this system we use a Markov chain as detailed below.

Beginning with a population vector $\vec{P}_0$ where each entry represents the population in a vibrational state in the $\widetilde{\mathrm{X}}$ electronic manifold:

$$\vec{P}_0 = \begin{bmatrix} P_{(000)} \\ P_{(100)} \\ P_{(200)} \\ P_{(001)} \\ P_{(02^00)} \\ \cdots \\ P_{(v_1v_2^lv_3)} \end{bmatrix} \tag{6.1}$$

The change in population cause by scattering a photon can be represented with a matrix **S** where each column of **S** ($\mathbf{S}_i$) is comprised of the vibrational branching ratios (VBRs) of the excited state that is coupled to the vibrational state in the i^{th} index. In our example, we will look at $\mathbf{S}_1$ where the $\widetilde{\mathrm{X}}(000)$ state is coupled to the $\widetilde{\mathrm{A}}(000)$ state with the Frank-Condon factors listed in Table 6.1 using the partial vibrational state map presented in Eq. 6.1:

$$S_1 = \begin{bmatrix} 0.0957 \\ 0.043 \\ 1.3 \times 10^{-3} \\ 7 \times 10^{-6} \\ 3 \times 10^{-3} \\ \cdots \\ VBR_{\widetilde{\mathrm{A}}(000)\rightarrow\widetilde{\mathrm{X}}(v_1 v_2^l v_3)} \end{bmatrix} \tag{6.2}$$

With this formalism the population change from a photon scattering event maps population $\vec{P}_0$ to $\vec{P}_1$ by multiplication with matrix **S**

$$\vec{P}_1 = \mathbf{S}\vec{P}_0 \tag{6.3}$$

and by extension the effect of n scattering events can be modeled as

$$\vec{P}_n = \mathbf{S}^n\vec{P}_0 \tag{6.4}$$

The columns of **S** must be sum to 1 to preserve the population in the system. This model can be modified to include decay pathways outside of the $\widetilde{\mathrm{X}}$ manifold with additional indices. Additionally, if a state is not repumped, the corresponding column of S can reflect how it evolves. For example, if a state not addressed and the population accumulates in that state, the corresponding column of **S** is simply a 1 on the diagonal entry and 0's elsewhere.

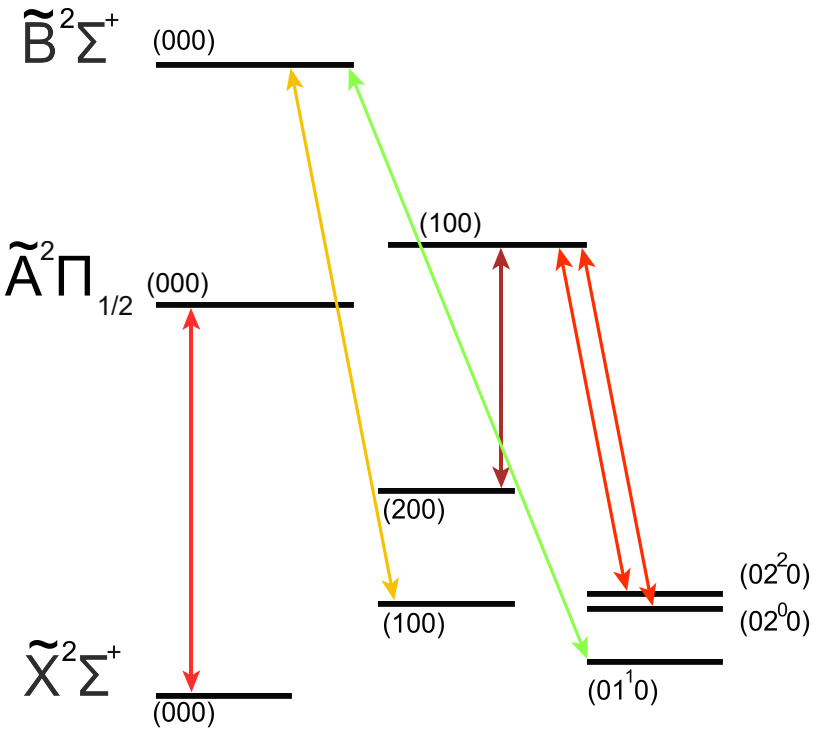

Figure 6.1: Laser cooling Scheme for CaOH

6.1.3 Depletion-revival measurements

The experimental efforts that revealed an additional loss mechanism consist of a series of depletion-revival tests. In these experiments, molecular population was optically pumped into higher vibrational states using photon cycling with the main and 1^{st} repumping lasers. Higher vibrational repumpers were added in the cleanup region to recover this lost population. A schematic of the experimental setup is shown in Figure 6.2. The data for these measurements was collected by alternating measurements of the unperturbed molecular beam with measurements of the depleted and revived signal in order to normalize against ablation fluctuations. The data is further complicated by the non-negligible natural population present in the excited vibrational modes and imperfect optical pumping. Ultimately, interleaving four

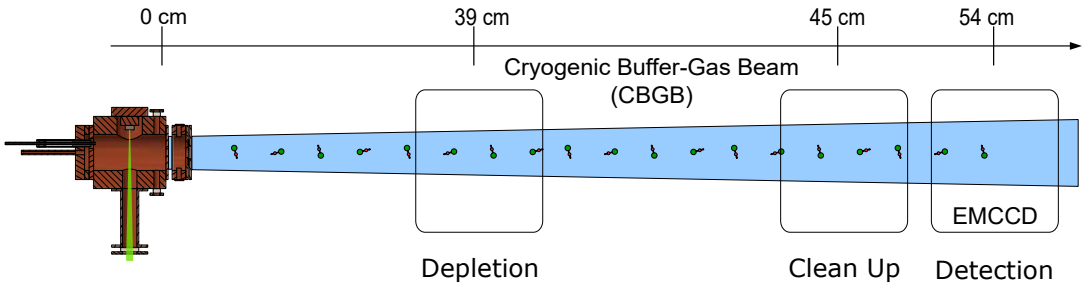

Figure 6.2: Generic depletion-revival experimental configuration.

different experimental conditions allowed us to correct for these complications and extract the percentage of recovered population. These conditions are indicated below

(A) Only Detection Light

(B) Detection Light and Cleanup Light

(C) Depletion Light and Detection Light

(D) Depletion, Cleanup and Detection light

The population measured in these configurations allows us to extract the population optically pumped into higher vibrational states (**(A)-(C)**), the natural population of the higher vibrational states (**(B)-(A)**) all while normalizing against ablation fluctuations. The reported quantity, the recovered population percentage is

$$\text{Recovered Percentage} = \frac{\textbf{(D) - (C) - (B)}}{\textbf{(A) - (C)}} \tag{6.5}$$

This recovered population can be compared to the prediction from the Markov chain model to determine if the branching ratios predicted from Franck-Condon factors are correct. The first test that indicated we had missing population involved the following laser configuration:

Depletion	Cleanup	Detection
$\widetilde{X}^2\Sigma^+(000) \rightarrow \widetilde{A}^2\Pi_{1/2}(000)$	$\widetilde{X}^2\Sigma^+(100) \rightarrow \widetilde{B}^2\Sigma^+(000)$	$\widetilde{X}^2\Sigma^+(000) \rightarrow \widetilde{A}^2\Pi_{1/2}(000)$
$\widetilde{X}^2\Sigma^+(100) \rightarrow \widetilde{B}^2\Sigma^+(000)$	$\widetilde{X}^2\Sigma^+(200) \rightarrow \widetilde{A}^2\Pi_{1/2}(100)$	$\widetilde{X}^2\Sigma^+(100) \rightarrow \widetilde{B}^2\Sigma^+(000)$
	$\widetilde{X}^2\Sigma^+(02^00) \rightarrow \widetilde{A}^2\Pi_{1/2}(100)$	

The results of this depletion-revival test are presented in Figure 6.3 as a function of laser power. The clear saturation at $\sim$ 70% is substantially below the expected Markov limit at 95 %. Some disagreement with the Markov limit was expected as the branching ratio to $\widetilde{X}(01^10)$ was underestimated in the Markov model. In the Markov model, the branching ratio to $\widetilde{X}(01^10)$ is a second order process, where molecules decay to $\widetilde{X}(100)$ and as they are repumped through the $\widetilde{B}(000)$ state, they decay to $\widetilde{X}(01^10)$. As described in Section 6.2.1, there would be some decay directly from the $\widetilde{A}(000)$ state not accounted for in the Markov model. However, this was estimated to be a small fraction of the discrepancy in our data.

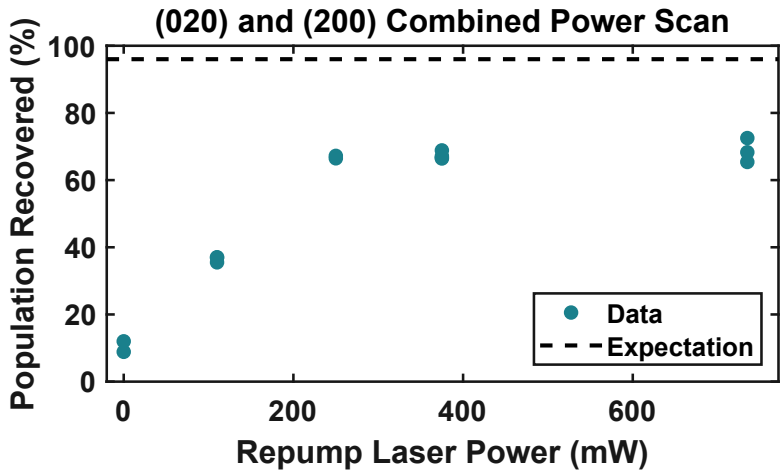

Figure 6.3: Incomplete population recovery with (200) and (02^00) repumpers.

In order to determine if decay to $\widetilde{X}(01^10)$ was responsible for the missing population, we identified the $\widetilde{X}^2\Sigma^+(01^10) \rightarrow \widetilde{B}^2\Sigma^+(000)$ as described in greater detail in Appendix D. With

this repumping transition, it was found that 7(1)% of the population was decaying to this state which left 18% of the population unaccounted for. For reference, this level of missing population indicated a branching ratio similar to the branching ratio to the $\widetilde{\mathrm{X}}(200)$ state. Several hypotheses could explain the loss of population.

- Rotational branching to N=3.
- An issue with repumping through the $\widetilde{\mathrm{A}}^2\Pi_{1/2}(100)$ state.
- An issue with repumping through the $\widetilde{\mathrm{B}}2\Sigma^+(000)$ state.
- Vibrational branching to a higher vibrational state.

If we had misidentified the $P(N'' = 1)$ branch with the $Q(N'' = 1)$ branch in one of our repumping transitions, we would expect to see some decay to $\widetilde{\mathrm{X}}(000)(N = 3)$. For this test we monitored the population of the $\widetilde{\mathrm{X}}(000)(N = 3)$ state, with and without photon cycling. The results, depicted in Figure 6.4, indicated no significant increase in N=3 population. This verified that our repumping transitions have all been correctly identified.

Our second hypothesis was that there was an issue repumping through the $\widetilde{\mathrm{A}}^2\Pi_{1/2}(100)$ state. In CaOH, the bending vibrational mode frequency that is approximately 1/2 of the Ca-O streching mode frequency. In all electronic states this leads to a series of energy levels that are closely spaced. Vibrational states of the same vibronic symmetry interact via Fermi-resonances, or avoided crossings between these vibrational states [211]. This has been well studied in CaOH [212, 146, 213], and the $\widetilde{\mathrm{A}}^2\Pi_{1/2}(100)$ state is strongly perturbed by a Fermi-resonance with the $\widetilde{\mathrm{A}}^2\Pi_{1/2}(020)$ state [146]. In fact, the $\widetilde{\mathrm{A}}^2\Pi_{1/2}(100)$ state state was chosen as the electronic state used to repump the $\widetilde{\mathrm{X}}(02^00)$ state because the Fermi-resonance leads to intensity borrowing from the $\widetilde{\mathrm{A}}^2\Pi_{1/2}(02^00)$ state that results in a stronger repumping transition. However, when the repumping lasers were tuned to the $\widetilde{\mathrm{A}}^2\Pi_{1/2}(000)$ transition directly repumping the higher vibrational states, we did not see any increase in recovered population.

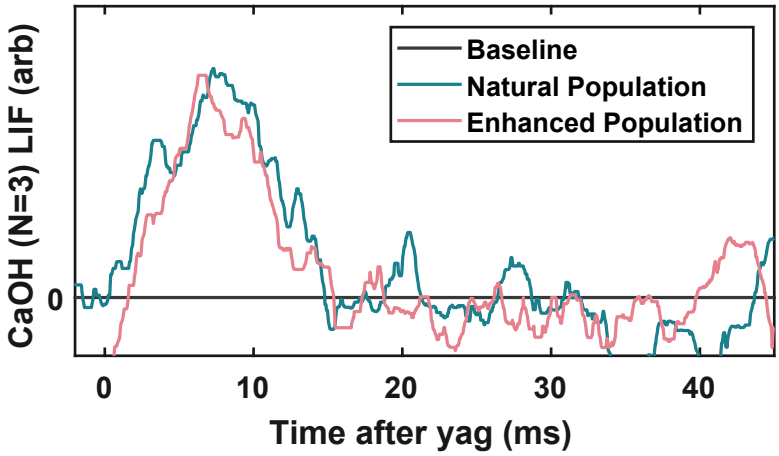

Figure 6.4: Testing for population accumulation in the N=3 rotational state of CaOH. The data is consistent with no buildup due to photon cycling. The increased noise of this signal is related to the low natural population of N=3. This verifies that our repumping lasers address the rotationally closed P(N"=1) line

We concluded that the $\widetilde{A}^2\Pi_{1/2}(100)$ was performing as expected. We also eliminated issues potentially arising from the $\widetilde{B}^2\Sigma^+(000)$ state.

We concluded that the unexpected loss was occurring from the $\widetilde{A}^2\Pi_{1/2}(000)$ state and conducted careful depletion-revival tests using only the main and 1^{st} repumper with the lasers applied as indicated below:

Depletion	**Cleanup**	**Detection**
$\widetilde{X}^2\Sigma^+(000) \rightarrow \widetilde{A}^2\Pi_{1/2}(000)$	$\widetilde{X}^2\Sigma^+(100) \rightarrow \widetilde{B}^2\Sigma^+(000)$	$\widetilde{X}^2\Sigma^+(000) \rightarrow \widetilde{A}^2\Pi_{1/2}(000)$
		$\widetilde{X}^2\Sigma^+(100) \rightarrow \widetilde{B}^2\Sigma^+(000)$

The results, depicted in Figure 6.5, show the repumped fraction is consistently below the limit predicted by the Markov analysis. These results support the conclusion that the loss was occurring from the $\widetilde{A}^2\Pi_{1/2}(000)$ state.

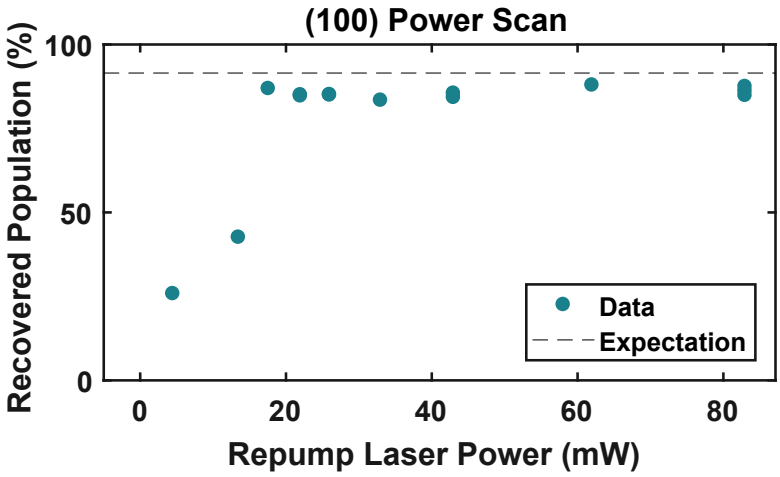

Figure 6.5: Population recovered after cycling photons with only the main $\widetilde{X}^2\Sigma^+(000) \rightarrow \widetilde{A}^2\Pi_{1/2}(000)$ transition. The level of experimental error can be inferred by scatter in data points when the recovered population is saturated.

6.2 Determination of loss pathway and loss mechanism

After spectroscopy to identify higher vibrational states, we conducted a series of tests to determine if any of those states were populated though photon cycling. The results, shown in Figure 6.6, clearly indicate that the $\widetilde{X}(02^20)$ state was being populated by the photon cycling process.

6.2.1 Vibrational selection rules

Vibrational branching to the $\widetilde{X}(02^20)$ state in CaOH was unexpected given the selection rules that apply to vibrational angular momentum and the lack of observations in the literature. Electronic transitions in CaOH have a nominal selection rule $\Delta l = 0$, that originates from the separation of electronic and vibrational wave functions in the Born-Oppenheimer approximation [137]. This separation forbids the exchange of electronic angular momentum with vibra-

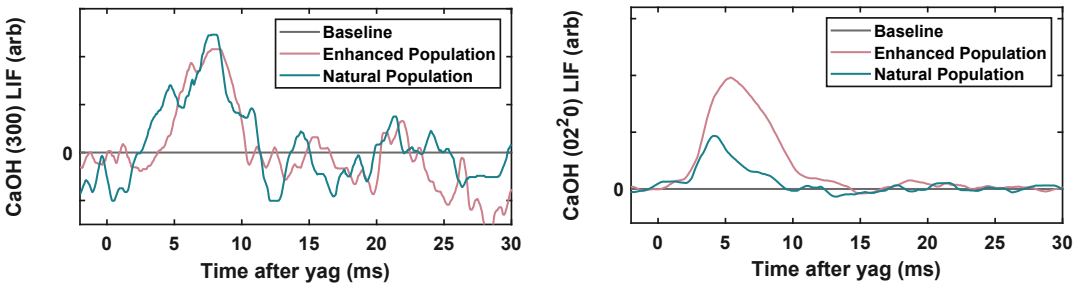

Figure 6.6: (left) CaOH $\widetilde{X}(300)$ state population with and without enhancement due to photon cycling. No significant enhancement is seen. (right) CaOH $\widetilde{X}(02^20)$ state population with and without enhancement due to photon cycling. The clear enhancement in population indicates that this channel is significantly populated by photon cycling. This unexpected branching is consistent with all of the unexpected loss in our system.

tional angular momentum. However, decay violating this selection rule with $\Delta l = 1$ has been previously observed in CaOH [150] as well as other triatomic molecules (SrOH and BaOH) [214]. We observe both $\widetilde{A}^2\Pi^+_{1/2}(000) \rightarrow \widetilde{X}^2\Sigma^+(01^10)$, and $\widetilde{A}^2\Pi^+_{1/2}(000) \rightarrow \widetilde{X}^2\Sigma^+(02^20)$ transitions in CaOH. The mechanism that has been proposed to explain the $\Delta l = 1$ transitions is an interaction between the $\widetilde{B}^2\Sigma^+(01^10)$ and the $\widetilde{A}^2\Pi^+_{1/2}(000)$ state leading to intensity borrowing. This mixing is due to a second-order effect combining the Renner-Teller interaction and the spin-orbit interaction. The Renner-Teller term in the Hamiltonian is given by Eq. 6.6 [215].

$$H_{RT} = V_{11}\left(Q_+e^{-i\theta} + Q_-e^{+i\theta}\right) + V_{22}\left(Q_+^2e^{-2i\theta} + Q_-^2e^{+2i\theta}\right) + \cdots \tag{6.6}$$

The first term is the dipolar term which mixes states with $\Delta v_2 = \pm 1$, $\Delta l = \pm 1$, $\Delta\Lambda = \pm 1$, and $\Delta K = \pm 0$, while the second term is the quadrupolar term which mixes states with $\Delta v_2 = \pm$, $\Delta l = \pm 2$, $\Delta\Lambda = \pm 2$, and $\Delta K = \pm 0$. The effect of the dipolar term is described in detail in appendix C of Ivan's thesis [167], we will not replicate that derivation here. The decay probability from $\widetilde{A}^2\Pi^+_{1/2}(000) \rightarrow \widetilde{X}^2\Sigma^+(01^10)$ is estimated by the expression [167]

$$P_{(000)-(01^10)} \propto \frac{2(\langle \widetilde{\mathrm{A}}|H_{RT}|\widetilde{\mathrm{B}}\rangle \langle \widetilde{\mathrm{B}}|H_{SO}|\widetilde{\mathrm{A}}\rangle)^2}{(\omega_2 E_{\widetilde{\mathrm{A}}-\widetilde{\mathrm{B}}})^{@}} \tag{6.7}$$

$$P_{(000)-(01^10)} \propto \frac{4\Delta g_L A_{SO}^2}{w_2^2} \tag{6.8}$$

Where $\Delta g_L = -g_k/\omega_2$ [216]. The spectroscopically measured values of $g_K = 0.594$ cm^{-1}, $A_{SO} = 66.8$ cm^{-1}, and $\omega_2 = 354.4$ cm^{-1} lead to an estimated decay probability of:

$$P_{(000)-(01^10)} \approx 2.4 \times 10^{-4} \tag{6.9}$$

Which is consistent with experimental observations.

6.2.2 $\widetilde{\mathbf{A}}^2\Pi^+_{1/2}(000) \rightarrow \widetilde{\mathbf{X}}^2\Sigma^+(02^20)$ decay

The observed decay to the $\widetilde{\mathrm{X}}^2\Sigma^+(02^20)$ state is attributed to direct coupling of the $\widetilde{\mathrm{A}}^2\Pi^+_{1/2}(000)$ state to the $\widetilde{\mathrm{A}}^2\Pi^+_{1/2}(02^20)$ state by the quadrupolar term in the Renner-Teller Hamiltonian. The $Q^2_\pm$ operators act as follows:

$$\begin{aligned}
\langle v_2+2, l\pm 2|Q^2_\pm|v_2, l\rangle &= \frac{1}{\sqrt{2\gamma_2}}\sqrt{(v_2 \pm l+2)(v2 \pm l+4)} \\
\langle v_2, l\pm 2|Q^2_\pm|v_2, l\rangle &= \frac{1}{\sqrt{2\gamma_2}}\sqrt{(v_2 \mp l)(v2 \pm l+2)} \\
\langle v_2-2, l\pm 2|Q^2_\pm|v_2, l\rangle &= \frac{1}{\sqrt{2\gamma_2}}\sqrt{(v_2 \mp l)(v2 \mp l-2)}
\end{aligned} \tag{6.10}$$

For these expressions:

$$\gamma_2 = \frac{2\pi c}{\hbar}\omega_2 \tag{6.11}$$

This operator can only couple states of the same K, within the $\widetilde{\mathrm{A}}$ manifold. Because Λ is a signed value, it can couple states:

$$|\Lambda = \pm 1, l = 0\rangle \Longleftrightarrow |\Lambda = \mp 1, l = 2\rangle \tag{6.12}$$

We need to evaluate V_{22} to estimate this coupling strength. Using Eq. 2.4.27 from Hirota [215]:

$$\langle V_{22}\rangle = \varepsilon^{(1)}\omega_2\gamma_2 \tag{6.13}$$

The parameter $\varepsilon\omega_2$ has been measured spectroscopically in CaOH ($\varepsilon\omega_2$ = 36 cm^{-1}), this term is expected to be dominate by the 1st-order contribution ($\varepsilon^{(1)}\omega_2$) but other terms may provide significant corrections. The 2nd-order term can be related to another spectroscopic parameter as follows:

$$\varepsilon^{(2)}\omega_2 = -\frac{1}{2\gamma_2}\frac{1}{hc}\sum_{\Sigma',\Delta'}\frac{(-1)^S|\,\langle\widetilde{\mathrm{A}}\Pi|V_{11}e^{i\theta}|\Lambda'\rangle\,|^2(1+\frac{hc\omega_2}{\Delta E^2})}{\Delta E} \tag{6.14}$$

This summation can also be found in the definition of g_K:

$$g_K = \frac{\omega_2}{4\gamma_2}sum_{\Sigma',\Delta'}\frac{(-1)^S|\,\langle\widetilde{\mathrm{A}}\Pi|V_{11}e^{i\theta}|\Lambda'\rangle\,|^2}{\Delta E} \tag{6.15}$$

The $\widetilde{\mathrm{B}}$ state should dominate this summation due to its proximity to the $\widetilde{\mathrm{A}}$ state.

$$\varepsilon^{(2)}\omega_2 \approx -\frac{2g_k\Delta E_{\widetilde{\mathrm{B}}-\widetilde{\mathrm{A}}}}{\omega_2} \tag{6.16}$$

In CaOH $\varepsilon\omega_2$ = -36.26 cm^{-1} and g_K = 0.594 cm^{-1} [153][1]. We estimate that $\varepsilon^{(2)}\omega_2 \approx$ -6

[1]Please note that the value of g_K in ref. [146] was assigned in error

cm^{-1}, and $\varepsilon^{(1)}\omega_2 \approx 30\ cm^{-1}$. Applying 1^{st}-order perturbation theory we find

$$\begin{aligned}
|\widetilde{A}(000)\rangle &\approx |\widetilde{A}(000)\rangle + |\widetilde{A}(02^20)\rangle \frac{\langle \widetilde{A}(02^20)|H_{RT}|\widetilde{A}(000)\rangle}{E_{020} - E_{000}} \\
&\approx |\widetilde{A}(000)\rangle + |\widetilde{A}(02^20)\rangle \frac{\sqrt{2}(-30\ cm^{-1})}{730\ cm^{-1}} \\
&\approx |\widetilde{A}(000)\rangle - 0.05\,|\widetilde{A}(02^20)\rangle
\end{aligned} \tag{6.17}$$

From this work we can conclude that the vibrational branching ratio to the $\widetilde{X}(02^20)$ state is estimated to be $\sim 2\times 10^{-3}$, which is an order of magnitude above experimental observations.

6.3 Franck-Condon factor measurements

To extract the number of photons scattered during experiments, we commonly measure the population remaining after cycling photons which can be related to a photon number by modeling loss with the Franck-Condon factors. By the work described previously in this chapter, we have found that our calculated Franck-Condon factors are not sufficiently accurate to apply this technique. Previous measurements [150] were not sensitive to the vibrational decays of interest. This section will describe measurements of the vibrational branching ratios of the laser cooling scheme proposed in Section 2.5.2 and shown in Figure 6.1.

Two measurements are used to ascertain the vibrational branching ratios of our system. First, we will perform deflection by applying lasers addressing the $\widetilde{X}^2\Sigma^+(000) \rightarrow \widetilde{A}^2\Pi_{1/2}(000)$ and $\widetilde{X}^2\Sigma^+(000) \rightarrow \widetilde{B}^2\sigma^+(000)$ transitions. We will use the measured deflection to extract the number of photons scattered. A simultaneous measurement of the depletion of molecular population allows us to extract the effective vibrational branching ratio (VBR) of this combined system. Secondly, we optically pump molecules into excited vibrational states using the

same photon cycling scheme and measure the increase in population in each vibrational state directly. The increase in population in each vibrational state and the population lost to the states outside the system is proportional to the vibrational branching ratios of this laser cooling scheme.

6.3.1 Experimental apparatus

CaOH molecules are produced using a cryogenic buffer gas source [88, 179] as depicted in Figure 6.7 and described in detail in Section 4.7. Hot calcium atoms are produced by laser ablation of a metallic calcium target inside of a copper cell held at $\sim$ 2 K while flowing 6 standard cubic centimeters per minute (SCCM) of helium buffer gas. We simultaneously flow a small amount ($\sim$ 0.01 SCCM) of methanol vapor into the cell through a thermally isolated capillary at $\sim$ 250 K. Methanol molecules react with calcium atoms to produce CaOH. The CaOH molecules rapidly cool via collisions with the helium buffer gas. This produces CaOH at densities of $\sim 10^{10}$ cm^{-3} in a single rotational state, as measured by laser absorption in the cell. The cold CaOH molecules are entrained in the buffer gas flow and extracted from a two-stage cell into a cryogenic buffer-gas beam (CBGB) with a mean forward velocity of v_f $\sim$150 m/s and a transverse velocity spread of $v_\perp$ $\sim$20 m/s [88]. The CBGB is collimated by a 3 mm square aperture located 35.5 cm from the exit of the buffer-gas cell, resulting in a transverse temperature $T_\perp \sim 10$ mK. Collimation allows us to observe the deflection of the molecular beam and ensure we address all molecules with the applied laser light.

After exiting the aperture, the collimated molecular beam enters the interaction region containing the main and 1st repumping laser. The combined laser light, with a $\frac{1}{e^2}$ beam diameter of 12 mm makes between 0 and 3 passes through the interaction region propagating in the same direction. The main laser cooling light is linearly polarized and polarization is rapidly

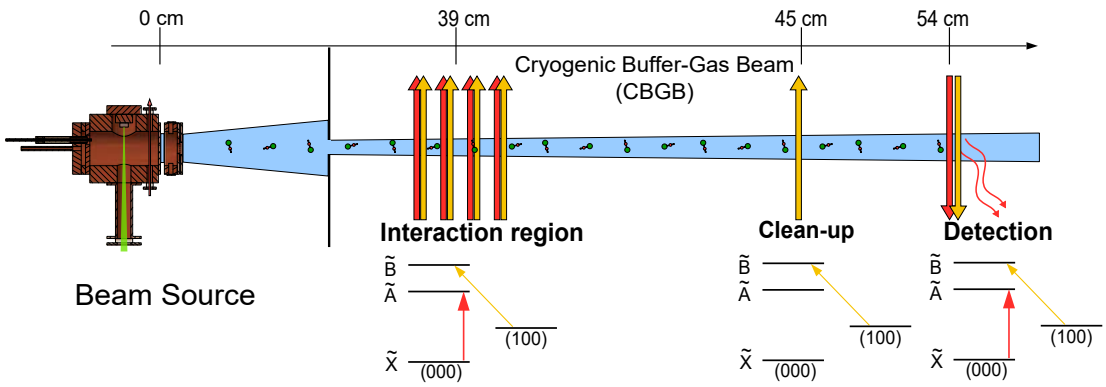

Figure 6.7: Experimental configuration for deflection with $\widetilde{X}^2\Sigma^+(000) \rightarrow \widetilde{A}^2\Pi_{1/2}(000)$ and $\widetilde{X}^2\Sigma^+(000) \rightarrow \widetilde{B}^2\Sigma^+(000)$ transitions.

switched using a voltage-variable waveplate (Pockels cell) to destabilize dark states.

Following the interaction region the $\widetilde{X}^2\Sigma^+(100) \rightarrow \widetilde{B}^2\Sigma^+(000)$ repumping laser is applied to recover population to ensure consistent detection efficiency. The momentum imparted by the lasers in the interaction region causes the molecular beam to be deflected relative to an unperturbed beam. The molecules are then excited with lasers addressing the $\widetilde{X}^2\Sigma^+(000) \rightarrow \widetilde{B}^2\Sigma^+(000)$ and $\widetilde{X}^2\Sigma^+(100) \rightarrow \widetilde{B}^2\Sigma^+(000)$ transitions. The resulting laser-induced fluorescence is imaged onto an EMCCD camera. The collection efficiency of the imaging system is measured to be constant over the region occupied by the molecules. The resulting image is integrated along the direction of molecule propagation to produce a spatial beam profile, which we fit to a Gaussian distribution. We parameterize the deflection using the center of the Gaussian fit. All data is collected with the lasers tuned to resonance.

Vibrational branching ratio to (000) and (100)

The population remaining after deflection can be modeled as follows:

$$P_f = P_i(p)^{\bar{n}} \tag{6.18}$$

Where $\bar{n}$ is the number of photons scattered, P_i is the initial molecular population, P_f if the final molecular population, and p is the vibrational branching ratio of the system. We can extract the number of photons scattered by the molecules by measuring the deflection when only the main cycling laser $\widetilde{X}^2\Sigma^+(000) \rightarrow \widetilde{A}^2\Pi_{1/2}(000)$ is applied. The number of photons scattered is modeled as a Bernoulli sequence where the average number of photons scattered by the main cooling transition is $\frac{1}{1-p}$ where p is the VBR to the $\widetilde{X}(000)$ state [126]. From previous measurements [150], scaled to account for unobserved decay pathways[2], we determine that the the VBR from $\widetilde{A}(000) \rightarrow \widetilde{X}(000) = 0.9539(21)$ corresponding to $\bar{n} = 21.7 \pm 1$ photons scattered per molecule when only the $\widetilde{X}(000)$ state is addressed. The deflection resulting from 21.7 photons is used to convert the deflection, given by the shift in the center of Gaussian fit, into a number of photons scattered $\bar{n}$. We simultaneously measure the ratio of initial population to final population and extract the VBR from the following relation

$$Log(\frac{P_f}{P_i}) = (\bar{n})(log(p)) \tag{6.19}$$

Figure 6.8 combines the results of multiple deflection measurements, indicating the vibrational branching ratio of the indicated laser cooling scheme to both the $\widetilde{X}(000)$ and $\widetilde{X}(100)$ states is 0.9968(5).

One systematic error in this measurement is a Doppler shift introduced by the velocity imparted during deflection relative to the detection light. This small shift reduces the scattering rate for highly deflected molecules, reducing the apparent population remaining after manip-

[2] In ref. [150] the VBRs to $\widetilde{X}(000)$ and $\widetilde{X}(100)$ sum to 1, given the known decay to higher vibrational states this is unphysical. We scale the published VBR's to the measured value determined in this work to determine the VBR from $\widetilde{A}(000) \rightarrow \widetilde{X}(000)$. (e.g. 0.957 (.9968) =0.9539(21))

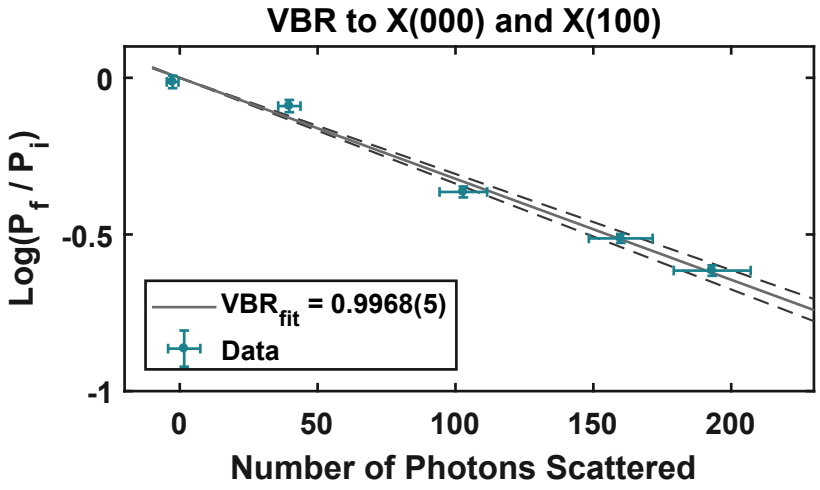

Figure 6.8: Log($\frac{P_f}{P_i}$) vs Number of Photons scattered. The error in X is dominated by the uncertainty in photons scattered for the calibration measurement, that is the uncertainty in the VBR from $\widetilde{\mathrm{A}}(000) \rightarrow \widetilde{\mathrm{X}}(000)$. The grey line indicates the results of a linear fit with the dashed lines indicating uncertainty in the fit. The results indicate the VBR out of the (000) + (100) system to be 0.9968(5).

ulation. We compensate for this effect by multiplying the magnitude of remaining population by a normalization factor that consists of the ratio between the predicted scattering rate (modeled by Eq. 5.9) and the scattering rate on resonance. Power broadening reduces this effect, but it remains a significant source of experimental error.

Vibrational branching ratio to (200), ($02^0$0), ($02^2$0), and ($01^1$0)

In order to measure the vibrational branching ratios to higher vibrational states, we measure the population directly. The photon cycling lasers addressing the $\widetilde{\mathrm{X}}^2\Sigma^+(000) \rightarrow \widetilde{\mathrm{B}}^2\Sigma^+(000)$ and $\widetilde{\mathrm{X}}^2\Sigma^+(100) \rightarrow \widetilde{\mathrm{B}}^2\Sigma^+(000)$ transitions are retroreflected between two mirrors for a total of $\sim$ 12 cm of interaction distance. This interaction length optically pumps nearly all (87.9(7)%) of the molecular population to higher vibrational states. The measured VBR to the $\widetilde{\mathrm{X}}(000)$ and $\widetilde{\mathrm{X}}(100)$ states allows us to determine that this level of population loss is consistent with scattering 660^{+120}_{-70} photons in the interaction region. By applying different combinations of

Table 6.2: Summary of optical pumping measurements and vibrational branching ratios to each vibrational state addressed in this work. The population lost to higher vibrational states is captured by the heading "other".

Laser Transitions in Cleanup Region	Vibrational States Repumped	Repumped Fraction (%)	VBR
$\widetilde{X}(200) \rightarrow \widetilde{A}(100)$	$\widetilde{X}(200)$	27(2)	$9(2)\times10^{-4}$
$\widetilde{X}(02^00) \rightarrow \widetilde{A}(100)$	$\widetilde{X}(02^00)$	36(1)	$1.3(2)\times10^{-3}$
$\widetilde{X}(02^20) \rightarrow \widetilde{A}(100)$	$\widetilde{X}(02^20)$	9(1)	$3.1(5)\times10^{-4}$
$\widetilde{X}(01^10) \rightarrow \widetilde{B}(000)$	$\widetilde{X}(01^10)$	7(1)	$2.4(4)\times10^{-4}$
$\widetilde{X}(200) \rightarrow \widetilde{A}(100)$ $\widetilde{X}(02^00) \rightarrow \widetilde{A}(100)$ $\widetilde{X}(02^20) \rightarrow \widetilde{A}(100)$ $\widetilde{X}(01^10) \rightarrow \widetilde{B}(000)$	$\widetilde{X}(200)$ $\widetilde{X}(02^00)$ $\widetilde{X}(02^20)$ $\widetilde{X}(01^10)$	87(1)	0.99955(7)
	Other	13(1)	$4.5(7)^{-4}$

repumping lasers in the clean-up region, we can selectively repump molecules from one or all of the higher vibrational states of interest. The results of these optical pumping measurements are shown in Table 6.2.

The decay probability from our photon cycling scheme must be equal to 1. The measured VBR to $\widetilde{X}(000)$ and $\widetilde{X}(100)$ accounts for 0.9968(5). We assign the remaining $3.2(5)\times10^{-3}$ to the vibrational states in accordance to ratio of their repumped fraction also shown in Table 6.2. These measurements are in agreement with previous results in the literature [150], and we hope to replicate dispersed laser fluorescence measurements in CaOH to confirm these results. Some of the population is not recovered and we attribute this to loss to higher vibrational states indicated as other.

These measurements were conducted to determine the number of photons scattered during

application of magneto-optical forces as described in the next chapter. These measurements indicate that the laser cooling scheme presented in Figure 6.1 will allow 2200^{+400}_{-300} photons to be scattered per molecules. Calculations of Franck-Condon factors indicate that the next vibrational states that will require repumping will be $\widetilde{\mathrm{X}}(300)$, $\widetilde{\mathrm{X}}(12^{0}0)$, and $\widetilde{\mathrm{X}}(02^{2}0)$ states. The transitions $\widetilde{\mathrm{X}}(300) \rightarrow \widetilde{\mathrm{A}}(100)$, $\widetilde{\mathrm{X}}(12^{0}0) \rightarrow \widetilde{\mathrm{A}}(100)$, and $\widetilde{\mathrm{X}}(12^{2}0) \rightarrow \widetilde{\mathrm{A}}(100)$ have all been found (see Appendix D). Predictions estimate the addition of those three repumpers, will allow for a photon budget in excess of 10,000 photons which will enable optical slowing and a robust MOT of CaOH.

7

1D Magneto-optical trapping of CaOH

In this chapter, we demonstrate radio frequency (RF) magneto-optical (MO) cooling and compression (1D MOT) of a beam of the polyatomic molecule $^{40}Ca^{16}OH$, which is an archetypal example of the broader class of MOR molecules. In doing so, we realize a cycling scheme capable of scattering $\sim 10^3$ photons. We characterize the MO forces applied here by extracting force constants and damping rates. A concomitant on-axis increase in molecular density is observed. This demonstration of MO cooling establishes a route towards "deep" laser cooling (10-100 μK) and optical trapping for numerous species of polyatomic molecules. This chapter will describe the operational principles of a MOT, the complications that arise in molecular systems, and present the first instance where magneto-optical forces are applied to polyatomic molecules.

7.1 MOT operation

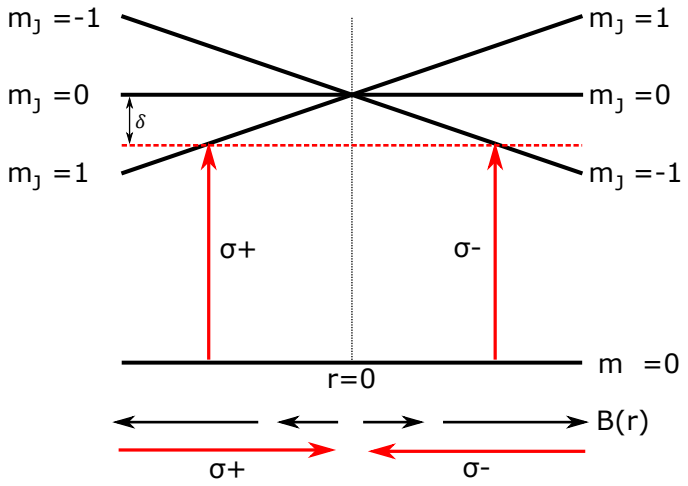

Figure 7.1: Schematic illustration of the setup and working principles of a magneto-optical trap. The magnitude of the magnetic field (B(r)) increases away from a field minimum located at r=0. The counter propagating lasers are detuned by δ as illustrated on the energy diagram above. These lasers become resonant if a particle has a sufficient Doppler shift, or if the magnetic field Zeeman shifts the particles onto resonance.

A magneto-optical trap (MOT) is a powerful tool used ubiquitously in atomic physics that combines a spatially varying magnetic field and 3 orthogonal pairs of counter-propagating laser beams to provide both a cooling and trapping force [217]. A quadrupole magnetic field is created by a pair of anti-Helmholtz coils. The magnetic field induces an increasing Zeeman shift as particles move away from the trap center and, with the correct choice of polarization, the orthogonal laser beams will preferentially scatter photons providing a restoring force. This is shown for the simple case of a J=0 to J=1 transitions illustrated in Figure 7.1. Near the trap center, the magnetic field splits the excited state into three magnetic sublevels with $m_J = -1,\ 0,\ +1$, while the ground state is unaffected. Red-detuned counter-propagating lasers with opposite polarizations, σ^+ and σ^-, are applied. Due to angular momentum conservation,

σ^+ light only couples states from $m_J{}'' = 0 \iff m_J{}' = 1$ while σ^- light only couples states from $m_J{}'' = 0 \iff m_J{}' = -1$. This ensures that with an appropriate choice of polarizations, any particle that is located away from the trap center scatters photons preferentially from the laser beam that propagates towards the trap center,and thus the particle experiences a restoring force. In tandem, the Doppler shift causes a particle with a non-zero velocity to scatter photons from a counter propagating laser leading to a damping force.

The combination of these two effects gives rise to a force profile described by the following expression for F_{MOT} that is derived from the scattering force [209]:

$$F_{scattering}(\delta) = \hbar k \frac{\gamma_{eff}}{2} \frac{s_eff}{1 + s_{eff} + 4(\delta/\gamma)^2} \tag{7.1}$$

The scattering force is applied from both directions and is a function of effective detuning $\delta = w - kv - (w_0 + \mathrm{B}z)$ where v is the velocity of the particle and z is the displacement from the center of the MOT.

$$F_{MOT} = F_{scattering}(w - kv - (w_0 + \beta z)) - F_{scattering}(w + kv - (w_0 - \beta z)) \tag{7.2}$$

This force is commonly linearized and parametrized as follows

$$F_{MOT} \approx -\alpha v - \frac{\alpha \mathrm{B}}{k} z \tag{7.3}$$

α is an effective damping constant and β is a Zeeman shift. These parameters are defined as follows [209]

$$\alpha = \frac{-8\hbar k^2 s\delta}{\gamma(1 + s + \frac{4\delta^2}{\gamma^2})} \tag{7.4}$$

$$\beta = \frac{g\mu_B}{\hbar}\frac{dB}{dz} \tag{7.5}$$

The capture velocity of a MOT is dependant on the rate at which a particle may scatter photons and the diameter (D) of the laser beams. This gives an estimate of how much kinetic energy may be removed as a particle traverses the trap [209].

$$\frac{1}{2}mv_c^2 = \frac{\hbar k\gamma}{2}D \tag{7.6}$$

$$v_c = \sqrt{\frac{\hbar k\gamma D}{m}} \tag{7.7}$$

We have measured the scattering rate in CaOH to be $\gamma \sim$2 MHz. Assuming 1 cm laser beams, the estimated maximum capture velocity of a MOT is 6 m/s.

As particles are trapped in a MOT, they are subject to a cooling force that saturates when it matches the random walk in velocity caused by emitting photons in the presence of cooling light. This is known as the Doppler limit which is given in Eq. 7.8 [209].

$$T_D = \frac{\hbar\Gamma}{k_B} \tag{7.8}$$

where Γ is the scattering rate of the cooling light. Given the parameters of CaOH we anticipate a Doppler temperature of $\sim$150 μK.

7.1.1 Type I vs Type II MOT

Type I and type II MOTs, schematically depicted in Figure 7.2, distinguish MOTs based on the angular momentum structure used for the photon cycling transition. The J"=0 to J'=1 MOT

described in the previous section is a type I MOT, which is typical of atomic MOTs. In molecular systems, to ensure rotational closure, photon cycling transitions have an inverted angular momentum structure (J"= J '+1), resulting in more ground states then excited state. A MOT made this type of transition is known as a type II MOT. For any polarization scheme there exist ground states that are dark to the excitation light. If nothing is done to destabilize these dark states, all of the molecular population rapidly accumulates in these dark states and is no longer subjected to the MOT force [218].

One solution, used in diatomic species [21, 203, 23], is to simultaneously switch both the laser polarization and the sign of the magnetic field gradient during cooling, which evolves magnetic dark states into bright states. This technique is known as an RF or AC MOT. This switching must occur at frequencies similar to the scattering rate in order to be effective.

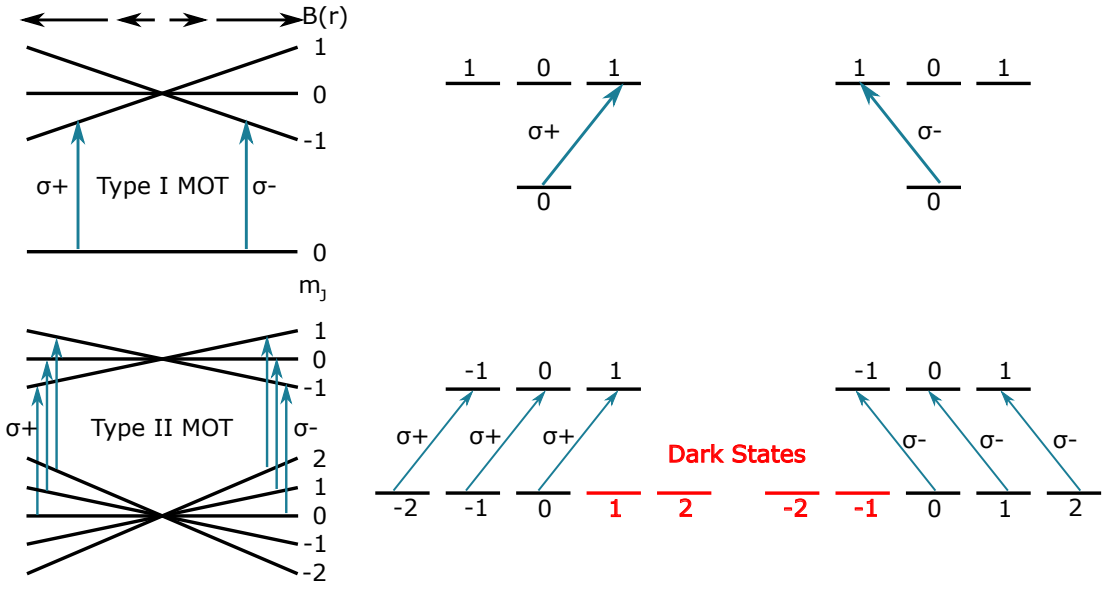

Figure 7.2: Schematic illustration of type I and type II MOT angular momentum structures. Note the existence of "dark states" in the type II mot configuration which do not couple to the excitation light.

7.2 Photon cycling scheme in CaOH

Effective MO cooling and compression requires scattering many photons without losing population to states that do not couple to the laser light ("dark states"). Establishing such a cycling transition in molecules requires closing both vibrational and rotational degrees of freedom, as depicted in Figure 7.3. Vibrational decay is not governed by rigorous selection rules but instead by wavefunction overlap, which is quantified by Franck-Condon factors (FCFs). CaOH is an example of a broad class of polyatomic molecules that have been identified as promising candidates for laser cooling due to their diagonal FCFs and strong electronic transitions [18, 150]. The main laser cooling transition in CaOH is the $\widetilde{X}^2\Sigma^+(000) \rightarrow \widetilde{A}^2\Pi_{1/2}(000)$ transition with a natural linewidth of $2\pi \times 6.4$ MHz at 626 nm [178]. The highly diagonal FCFs of the $\widetilde{A}^2\Pi_{1/2}(000)$ state suppress spontaneous decay to higher vibrational states during a single scattering event; nonetheless, significant optical pumping into excited vibrational states can occur when many photons are scattered. CaOH has three vibrational modes: a symmetric stretch, a doubly degenerate bend, and an antisymmetric stretch. These vibrational modes are labeled with four quantum numbers $(v_1, v_2{}^l, v_3)$, where v_1, v_2, and v_3 indicate the number of quanta in the symmetric stretching mode, the bending mode, and the antisymmetric stretching mode, respectively. l labels the nuclear orbital angular momentum in the bending mode and takes values of $l = -v_2, -v_2 + 2, ..., v_2$ [137]. Five repumping lasers, listed in Table 7.1, are used to establish a quasi-closed cycling scheme and recover population in these states, as depicted in Figure 7.3. Branching ratios within this cycling scheme are reported in Chapter 6.

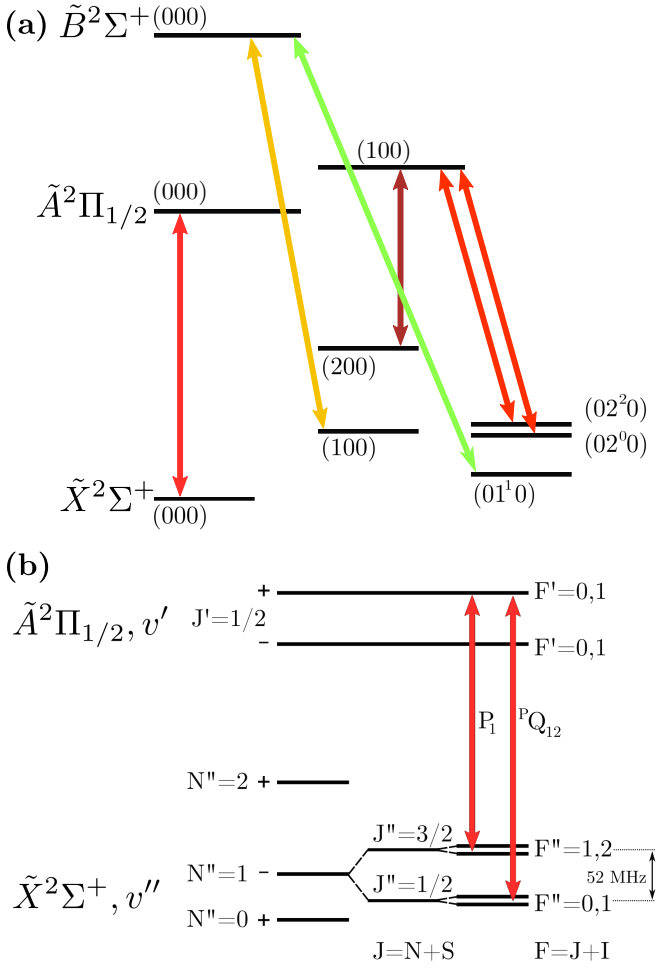

Figure 7.3: (a) Laser cooling scheme for CaOH. The vibrational structure depicted here indicates all levels that are addressed with lasers in order to limit the branching ratio to other vibrational states to 4.5×10^{-4}. (b) Rotational structure of CaOH illustrating the 52 MHz spin-rotation splitting in the electronic ground state as well as the unresolved hyperfine structure (1.5 MHz and 7 kHz in the $J'' = \frac{3}{2}$ and $J'' = \frac{1}{2}$ states respectively [142]). The $\widetilde{X}^2\Sigma^+(v_1''v_2''v_3'') \rightarrow \widetilde{A}^2\Pi_{1/2}(v_1'v_2'v_3')$ $P_1(J'' = \frac{3}{2})$ and ${}^PQ_{12}(J'' = \frac{1}{2})$ rotationally closed transitions are shown [126]. The parity of the ground states is indicated by the sign to the right of the N'' value while the parity of the excited states is indicated to the right of the J' value. The rotational structure of the $\widetilde{B}^2\Sigma^+(000)$ state is analogous to that of the $\widetilde{X}^2\Sigma^+$ states and is not pictured. Rotational closure on repumping lines through this state is achieved by driving $P_1(J'' = \frac{3}{2})$ and ${}^PQ_{12}(J'' = \frac{1}{2})$ transitions to the $\widetilde{B}^2\Sigma^+(N' = 0, J' = \frac{1}{2}, +)$ state. The level diagrams are not to scale.

Table 7.1: Optical transitions and corresponding wavelengths driven to form a quasi-closed cycling transition in CaOH. The $\widetilde{X}^2\Sigma^+(000) \rightarrow \widetilde{A}^2\Pi_{1/2}(000)$ transition is the main cooling line while the other five frequencies correspond to vibrational repumping lasers.

Transition			Wavelength (nm)
$\widetilde{X}^2\Sigma^+(000)$	$\rightarrow$	$\widetilde{A}^2\Pi_{1/2}(000)$	626.4
$\widetilde{X}^2\Sigma^+(100)$	$\rightarrow$	$\widetilde{B}^2\Sigma^+(000)$	574.3
$\widetilde{X}^2\Sigma^+(200)$	$\rightarrow$	$\widetilde{A}^2\Pi_{1/2}(100)$	650.4
$\widetilde{X}^2\Sigma^+(02^00)$	$\rightarrow$	$\widetilde{A}^2\Pi_{1/2}(100)$	629.0
$\widetilde{X}^2\Sigma^+(02^20)$	$\rightarrow$	$\widetilde{A}^2\Pi_{1/2}(100)$	630.0
$\widetilde{X}^2\Sigma^+(01^10)$	$\rightarrow$	$\widetilde{B}^2\Sigma^+(000)$	566.0

Notably, both the $\widetilde{X}^2\Sigma^+(01^10)$ and $\widetilde{X}^2\Sigma^+(02^20)$ states need to be repumped. As discussed in Section 6.2.1 Decays to these states are nominally forbidden by an approximate $\Delta l = 0$ selection rule that originates from the separation of electronic and vibrational degrees of freedom in the Born-Oppenheimer approximation. The breakdown of this selection rule has been observed previously for $\Delta l = 1$ transitions in CaOH (and other similar systems) and is attributed to a second order process involving Renner-Teller mixing and spin-orbit coupling leading to intensity borrowing via the $\widetilde{B}^2\Sigma^+(01^10)$ state [214, 150, 215]. Decay to the $\widetilde{X}^2\Sigma^+(02^20)$ stateis attributed to a similar mechanism that relies on the mixing of vibrational states within the $\widetilde{A}^2\Pi_{1/2}$ manifold (see Section 6.2.1). The previous chapter details our measurement of the branching ratio out of this cycling scheme to be $4.5(7) \times 10^{-4}$, which is predicted to be dominated by decay to the $\widetilde{X}^2\Sigma^+(12^00)$, $\widetilde{X}^2\Sigma^+(12^20)$, and $\widetilde{X}^2\Sigma^+(300)$ vibrational states.

To avoid populating rotational dark states, each laser beam (main and all repumpers) con-

tains two frequency components separated by the spin-rotation (SR) splitting of 52 MHz[1] depicted in Figure 7.3 (b). The hyperfine splitting is below the natural linewidth of the main cooling transition and does not require additional frequency sidebands [142]. This type of transition ($J \rightarrow J' = J - 1$) causes rapid optical pumping into magnetic dark states, significantly reducing the cooling and confining forces in molecular MOTs [218]. We address this by simultaneously switching both the laser polarization and the sign of the magnetic field gradient during cooling, which evolves magnetic dark states into bright states, as previously demonstrated in diatomic systems [21, 203, 23].

7.3 CaOH Zeeman structure

Because the Landé g-factor of the $\widetilde{A}^2\Pi_{1/2}(J' = \frac{1}{2})$ state in CaOH, $g_J^{(A)} \approx -0.021$, is more than an order of magnitude smaller than the g-factors of the $\widetilde{X}^2\Sigma^+(J'' = \frac{1}{2}, \frac{3}{2})$ states, we rely on the Zeeman shift of the lower states to apply significant magneto-optical forces. The Zeeman structure of both electronic states is shown in Figure 7.4. We label states in the $|J, m_J\rangle$ basis as hyperfine structure is significantly mixed at very small fields, making m_J a good quantum number. At low fields $\lesssim$ 5 G the Zeeman shifts in the ground state are approximately linear with g-factors $g_{J=1/2}^{(X)} = -2/3$ and $g_{J=3/2}^{(X)} = +2/3$, but deviate from linearity at fields $\gtrsim$ 10 G due to the relatively small spin-rotation splitting of 52 MHz. Because the lower ($J'' = 1/2$) manifold has a negative g-factor while the upper ($J'' = 3/2$) manifold has a positive g-factor, the laser polarizations used to apply MO restoring forces have opposite handedness for the two manifolds, as depicted in Fig 7.4. The $J \rightarrow J - 1$ nature of this transition leads to rapid optical pumping of population into magnetic dark states. As described in the

[1] 52 MHz is the SR splitting in states without vibrational angular momentum. For $\widetilde{X}^2\Sigma^+(01^10)$ the SR splitting is only 26 MHz as described in Appendix D. In $\widetilde{X}^2\Sigma^+(02^20)$ only the J=3/2 SR component of the state is populated during photon cycling thus no SR is required.

main text, we remix these dark states by switching the sign of the magnetic field in conjunction with the handedness of the polarization. This switching occurs at $\sim 10^6$ s^{-1} which is on the order of our scattering rate.

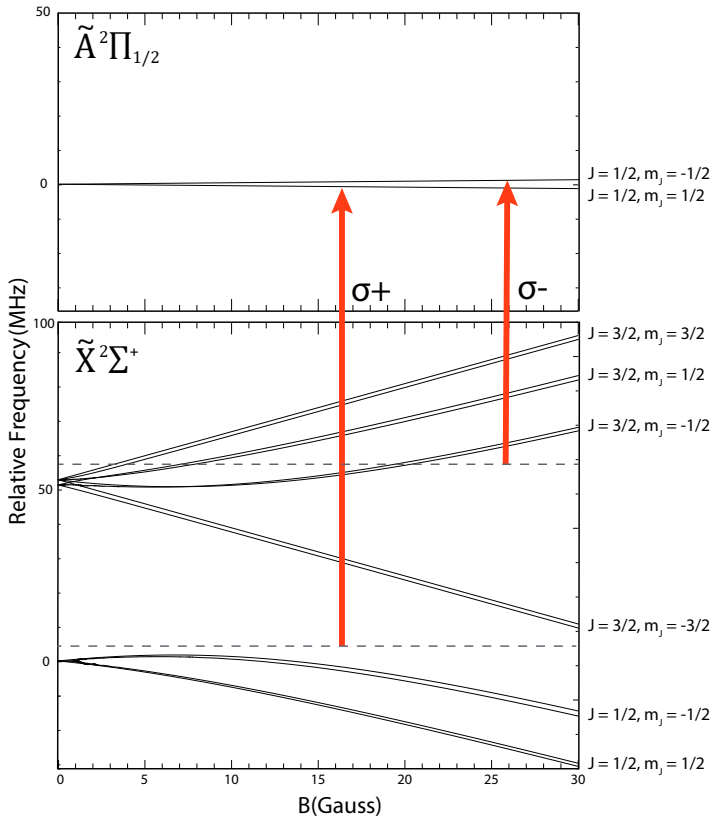

Figure 7.4: Plot of the calculated Zeeman shift of the ground and excited states of CaOH. The much smaller g-factor in the excited state is accentuated by the identical scale of the top and bottom panels.

7.4 Experimental apparatus

CaOH molecules are produced using a cryogenic buffer gas source [88, 179] as depicted in Figure 7.5. Hot calcium atoms are produced by laser ablation of a metallic calcium target inside of a copper cell held at ~ 2 K while flowing 6 standard cubic centimeters per minute

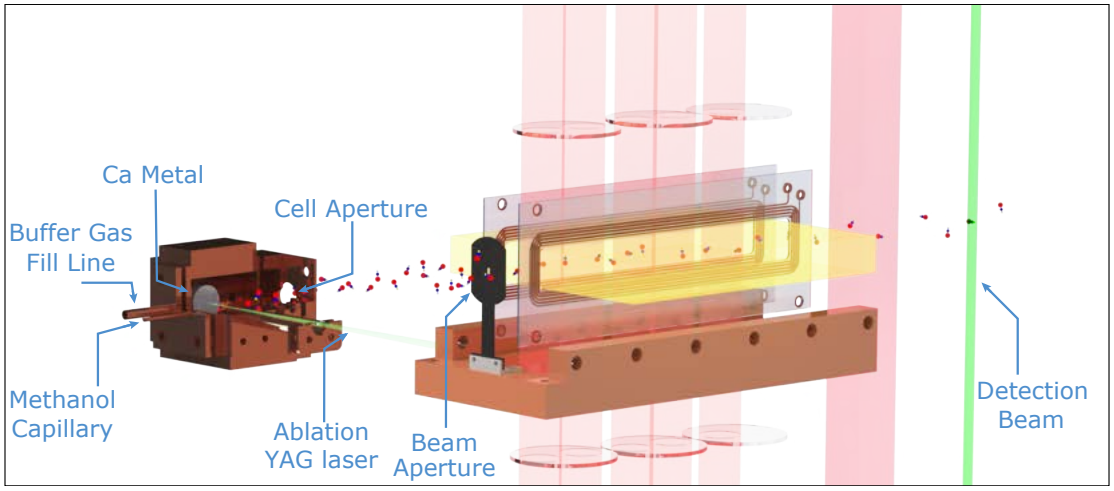

Figure 7.5: A rendering of the experimental apparatus. On the far left is the two-stage buffer-gas beam source, depicted in cut-away view for clarity. 35.5 cm from the exit of the buffer-gas cell, the molecular beam is collimated by a 3 mm square beam aperture. 39 cm from the cell, the molecules enter the interaction region where they are addressed with light from the main MO cooling beams in the vertical direction. Co-propagating vertically are the (100), (200) and $(02^{0}0)$ repumping lasers. The $(02^{2}0)$ and $(01^{1}0)$ repumping light is multipassed in the horizontal direction and extends beyond the MO region. A separate vertically multipassed region containing (100) and $(02^{0}0)$ repumping light lies after the magnetic field coils and serves to recover population from excited vibrational states. Finally, the molecules encounter a detection beam of smaller cross-section than the cooling and repumping light, and the resulting laser-induced fluorescence is collected and imaged onto an EMCCD.

(SCCM) of helium buffer gas. We simultaneously flow a small amount ($\sim$ 0.01 SCCM) of methanol vapor into the cell through a thermally isolated capillary at $\sim$ 250 K. Methanol molecules react with calcium atoms to produce CaOH. The CaOH molecules rapidly cool via collisions with the helium buffer gas. This produces CaOH at densities of $\sim 10^{10}$ cm^{-3} in a single rotational state, as measured by laser absorption in the cell. The cold CaOH molecules are entrained in the buffer gas flow and extracted from a two-stage cell into a cryogenic buffer-gas beam (CBGB) with a mean forward velocity of v_f $\sim$100 m/s and a transverse velocity spread of $v_\perp$ $\sim$20 m/s [88]. The CBGB is collimated by a 3 mm square aperture located 35.5 cm from the exit of the buffer-gas cell, resulting in a transverse temperature $T_\perp \sim 8.4$ mK.

After exiting the aperture, the collimated molecular beam enters the interaction region con-

taining six distinct wavelengths of light (main plus five repumpers). The combined laser light, with a beam diameter of 25 mm, makes 5 round trip passes through the interaction region as well as through a pair of $\lambda/4$ waveplates for 12.5 cm of total interaction length. The main laser cooling light is circularly polarized and retroreflected in a $\sigma^+ - \sigma^-$ configuration. The handedness of the polarization is rapidly switched using a voltage-variable waveplate (Pockels cell). A quadrupole magnetic field is generated with a pair of in-vacuum anti-Helmholtz coils and sinusoidally driven at the same frequency as the laser polarization switching with a controllable phase offset.

Following the interaction region, where MO cooling and compression take place, repumping lasers are applied to recover population from excited vibrational states. The molecules expand ballistically while propagating to the detection region, mapping the momentum distribution onto the spatial extent of the molecular beam. The molecules are then excited with lasers addressing the $\widetilde{X}^2\Sigma^+(000) \rightarrow \widetilde{B}^2\Sigma^+(000)$ and $\widetilde{X}^2\Sigma^+(100) \rightarrow \widetilde{B}^2\Sigma^+(000)$ lines with the resulting laser-induced fluorescence imaged onto an EMCCD camera. The collection efficiency of the imaging system is measured to be constant over the region occupied by the molecules. The resulting image is integrated along the direction of molecule propagation to produce a spatial beam profile, which we fit to a Gaussian distribution. We parameterize the width of the molecular beam by the standard deviation of the Gaussian fit. MO cooling and compression are seen as a narrowing of this width, as shown in Figure 7.6. The main cooling laser intensity was 1.6 mW/cm^2 for the data in Figure 7.6 and 3.3 mW/cm^2 for the data in Figure 7.8. All data were collected with an RF switching frequency of 530 kHz, a detuning of -7 MHz, and an RF voltage applied to the coils corresponding to a root-mean-square magnetic field gradient of 17 Gauss/cm.

The RF magnetic field is generated by a pair of in-vacuum coils. These coils consist of 8 turns of copper with dimensions 21 mm $\times$ 164 mm directly bonded to an aluminum ni-

tride substrate for thermal stability. The coils are mounted with a spacing of 23 mm. These coils are connected to independent resonant circuits outside the vacuum chamber which are driven by two radio frequency amplifiers. The inductance of the coils themselves is $\sim 15\ \mu$H. The resonant tank circuits are designed to maximize the transfer of RF power from the amplifiers to the coils. They consist of two vacuum variable, high power capacitors (150-1500 pF, 4 kV and 70-1600 pF, 3 kV) in parallel with high power ceramic capacitors. One of the capacitors (C_T) is used to tune the resonance frequency while the other (C_M) is tuned to achieve impedance matching with the amplifier. For operation at 530 kHz, the nominal values of the capacitances are $C_M \approx 1000$ pF and $C_T \approx 6000$ pF. We employ fast electro-mechanical relays in order to switch the field on and off in ~ 10 ms while withstanding high RF powers.

The magnitude and phase of the current through the MOT coils is monitored in situ by AC current probes. Under typical conditions the coils are driven at 530 kHz with $I_{rms} = 9.6$ A that corresponds to a magnetic field gradient of $B_{rms} = 17$ Gauss/cm. These coils are operated at a duty cycle of 10% to avoid heating and subsequent outgassing as seen in similar experiments [14].

7.5 Results

Figure 7.7 shows the width of the molecular beam as a function of applied main cooling laser intensity. The effect of the magneto-optical forces saturates at approximately 1.6 mW/cm^2. We attribute the saturation to a combination of sub-Doppler heating and overfocusing of the molecular beam. At higher laser intensities the observed molecular beam width does not decrease further while the photon scattering rate nonetheless increases, resulting in a loss of population to unaddressed vibrational states. These two competing effects lead to a maximum enhancement of on-axis beam brightness at a laser intensity of 1.6 mW/cm^2.

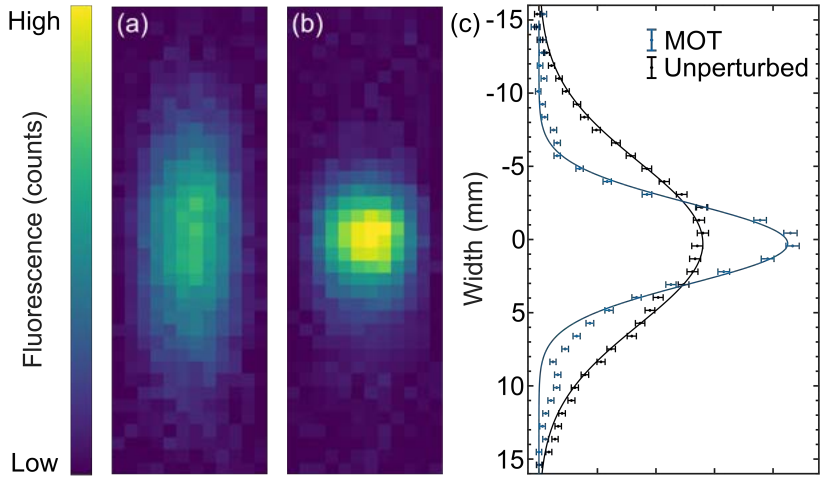

Figure 7.6: Raw images of the molecular beam taken for (a) unperturbed CaOH molecules and (b) under 1D MOT conditions. The molecular beam propagates from left to right in these images, while the cooling and detection light propagates in the vertical direction. (c) Horizontally integrated molecular beam profiles indicating cooling and on-axis density enhancement. Solid lines are fits to a Gaussian profile. These beam profiles have not been rescaled. The area of the MO compression trace is 78% of the unperturbed beam. Using the measured branching ratio out of our photon cycling scheme, this corresponds to ~ 550 photons scattered. At this laser intensity, on-axis beam brightness is optimized. At higher intensities, we observe saturation of the cooling and compression effects, while the concomitant additional photon scattering leads to population loss to unaddressed vibrational states.

In order to differentiate Doppler and MO effects, we scan the phase of the polarization switching relative to the magnetic field gradient switching, as shown in Figure 7.8. The greatest compression of the beam occurs at a phase of 0 degrees and corresponds to the MOT configuration, while at a phase of 180 degrees we see expansion of the beam, corresponding to the anti-MOT. The observed phase dependence is a clear signature of the application of MO forces in addition to the effects of Doppler cooling alone, represented by the gray shaded region in the figure. By measuring the loss of molecules to vibrational dark states as a function of cooling light intensity and by comparing to the known branching ratios of repumped vibrational levels, we are able to determine the number of photons scattered by the cooling process. We find that we can scatter up to 920^{+170}_{-120} photons during the cooling process, limited primar-

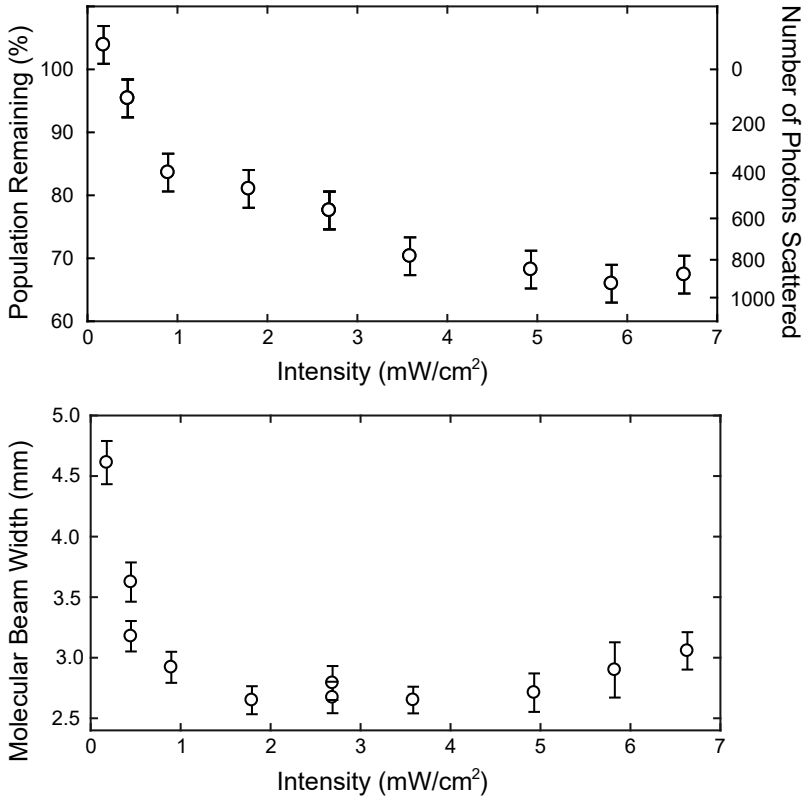

Figure 7.7: Molecular beam width vs. power for the 1D MOT configuration. The main cooling laser was detuned -7 MHz and all repumping lasers were on resonance.

ily by interaction time.

As a means of characterizing our system we use a Monte Carlo simulation to model molecular propagation and cooling dynamics. We model the Doppler cooling and magneto-optical forces in our system using a rate-equation model similar to that described in [203]. As shown in [30], for a generic molecule with N_g ground states coupled to N_e excited states, and under the assumption that all excited states undergo spontaneous decay at the same rate Γ, the scattering rate can be expressed as

$$R_{\mathrm{sc}} = \Gamma \frac{N_e}{(N_g + N_e) + 2\sum_{j=1}^{N_g}(1 + 4\Delta_j^2/\Gamma^2) I_{\mathrm{sat},j}/I_j} \tag{7.9}$$

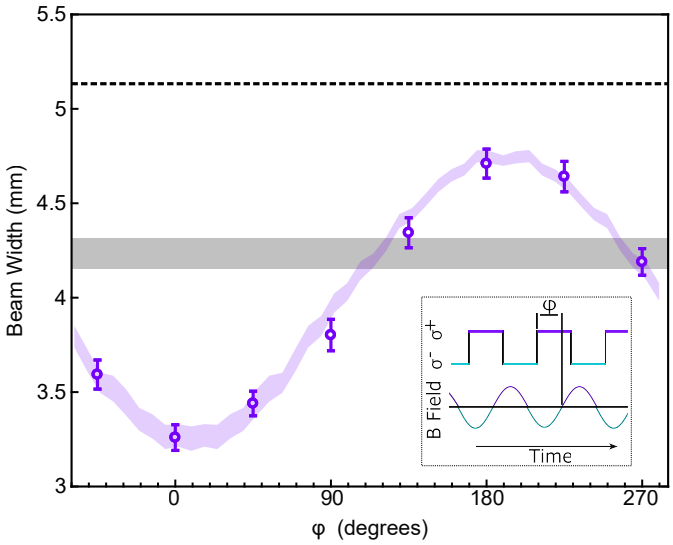

Figure 7.8: Molecular beam width as a function of phase offset (φ) between the polarization switching of cooling light and the oscillating magnetic field (see inset). The dashed black line indicates the width of the unperturbed beam, the shaded grey region indicates the measured width and associated error of the Doppler cooled beam without an applied magnetic field, and the shaded purple region indicates Monte Carlo simulation results for the full MO configuration. Clear compression at 0 phase corresponds to the MOT configuration, where the laser polarization provides a spatially confining force. At 180 degrees there is expansion of the beam, corresponding to the anti-MOT configuration. The main cooling light is detuned -7 MHz from resonance while all repumping lasers remain resonant. Error bars represent one standard deviation of the fitted Gaussian beam width.

where the sum is over all ground states j, I_j is the laser intensity addressing the jth state, Δ_j is its detuning, and $I_{\mathrm{sat},j} = \pi hc\Gamma/(3\lambda_j^3)$ is the corresponding two-level saturation intensity. Here h is the Planck constant, c is the speed of light, and λ_j is the wavelength of the jth transition. In the case of CaOH, the $\widetilde{X}^2\Sigma^+(000)$ ground state has $N_g = 12$ hyperfine components and the $\widetilde{A}^2\Pi_{1/2}(000)$ excited state has $N_e = 4$ hyperfine states, $\Gamma = 2\pi \times 6.4$ MHz, and $\lambda = 626$ nm.

We further simplify this model by noting that all saturation intensities are approximately equal, $I_{\mathrm{sat},j} \equiv I_{\mathrm{sat}} = \pi hc\Gamma/(3\lambda^3)$, and that all transitions are equally detuned, $\Delta_j \equiv \Delta$. This latter condition arises because the two SR components in the ground state are individually addressed by splitting the laser into two frequencies with an acousto-optic modulator (AOM),

and the laser is then globally detuned from resonance. The hyperfine splitting is small enough to be ignored at this level of approximation. Under these additional assumptions, the scattering rate due to a single laser simplifies to an effective two-level expression,

$$R_{\mathrm{sc}}(\Delta) = \frac{\Gamma_{\mathrm{eff}}}{2} \frac{s_{\mathrm{eff}}}{1 + s'_{\mathrm{eff}} + 4\Delta^2/\Gamma^2} \tag{7.10}$$

where

$$\Gamma_{\mathrm{eff}} = \frac{2N_e}{N_g + N_e}\Gamma \tag{7.11}$$

is the effective scattering rate and

$$\begin{aligned} s_{\mathrm{eff}} &= \frac{N_g + N_e}{2I_{\mathrm{sat}}} \left(\frac{N_g^{(1/2)}}{I_{1/2}} + \frac{N_g^{(3/2)}}{I_{3/2}}\right)^{-1} \\ &\approx \frac{N_g + N_e}{2N_g} \frac{(I/2)}{I_{\mathrm{sat}}} \end{aligned} \tag{7.12}$$

is the effective saturation parameter. Here we assume that the total laser intensity addressing all $N_g^{(1/2)} = 4$ states in the $J'' = 1/2$ ground-state manifold is $I_{1/2}$, and light with intensity $I_{3/2}$ addresses the $J'' = 3/2$ manifold with $N_g^{(3/2)} = 8$ states 52 MHz away. Because of this large frequency separation, there is no cross talk between the two spin-rotation components. The approximation in Eq. 7.12 assumes the total laser intensity I is balanced between the two SR components and bears out the intuition that each state should be approximately resonant with half the total laser intensity in this case. The quantity $s'_{\mathrm{eff}} \equiv I'/I_{\mathrm{sat}}$ in the denominator of Eq. 7.10 reflects the total intensity $I' > I$ of *all* cooling lasers and is included to account for saturation effects. In an n-dimensional cooling scheme s'_{eff} would equal $2ns_{\mathrm{eff}}$.

We implement a Monte Carlo simulation of the MO forces in our CaOH beam by propa-

gating $\sim 10^4$ molecules though a force field defined by the standard 1D expression $F_{\mathrm{MO}} = \hbar k[R_{\mathrm{sc}}(\Delta_1) - R_{\mathrm{sc}}(\Delta_2)]$, where $k = 2\pi/\lambda$ and the detunings $\Delta_{1,2}$ account for laser detuning δ_0 as well as Doppler and Zeeman shifts. The Zeeman shifts, in particular, are given by $\mu_{\mathrm{eff}} A' r/\hbar$, where r is the radial distance from the magnetic field origin, $A' = (2\sqrt{2}/\pi) A_{\mathrm{rms}} \cos\varphi$ is the time-averaged magnetic field gradient, A_{rms} is the sinusoidal rms gradient applied in the experiment, and φ is the phase offset between the oscillating gradient and laser polarization. μ_{eff} is the effective transition magnetic moment averaged over all 12 ground states (the excited state has negligible Zeeman shift); we estimate it as $\mu_{\mathrm{eff}} \approx \mu_B/2$ by solving multi-level rate equations [218] for the steady-state population of each ground state. To account for the radial symmetry of the field gradient we project the polarization of each cooling laser onto the local quantization axis of every molecule and treat σ^-, π, and σ^+ polarization components as driving effective transitions with negative, zero, and positive magnetic moment, respectively.

The spatial and velocity distribution of the molecules incident on the cooling region is determined by initializing $\sim 10^6$ molecules with a Gaussian spatial distribution of radial extent $\sigma_r \sim 8$mm and transverse temperature $T \sim 1$K at the output of the buffer gas cell. They ballistically propagate with Gaussian forward velocity distribution $v_f \sim 100 \pm 35$ m/s through the 3x3 mm beam aperture 35.5 mm downstream, after which only $\sim 0.1\%$ of the molecules remain, with a transverse temperature $T \sim 8.4$mK. Cooling forces are applied over a 12.5 cm length by five spatially separated, 25 mm diameter laser beams with uniform intensity. After cooling, the molecules ballistically propagate to the detection region, where their transverse spatial and velocity distributions are fit to Gaussians to extract beam width and temperature.

In order to fit the simulation to our data, we scale the overall MO force by making the replacement $\Gamma_{\mathrm{eff}} \to \Gamma'_{\mathrm{eff}} \equiv \zeta\Gamma_{\mathrm{eff}}$ in the above equations, and we also take μ_{eff} as a fit parameter. All other constants are held fixed at the values used in the experiment. For optimal experimental parameters of $I = 1.6$ mW/cm^2, $\delta_0 = -7$ MHz, and $A_{\mathrm{rms}} = 17$ G/cm, we find that our

simulation fits the data when $\zeta \approx 0.21$ and $\mu_{\text{eff}} \approx 0.53\mu_B$. This value of μ_{eff} is in line with that predicted from multi-level rate equations as described above, and suggests that our spatial MO forces are approximately optimal. The factor of ~ 5 reduction in overall cooling rate parametrized by ζ, meanwhile, is in line with similar imperfections previously quoted for a MOT of diatomic molecules [23, 202, 21, 205].

To extract the damping rate and MO oscillation frequency we linearize the applied force to find $F_{\text{MO}} \approx -\alpha v - \kappa r$, where v and r are the velocity and position of the molecules with respect to the magnetic field origin and the force constants are

$$\alpha = -\frac{8\hbar k^2 s_{\text{eff}} \Gamma'_{\text{eff}} \delta_0}{\Gamma^2 (1 + s'_{\text{eff}} + 4\delta_0^2/\Gamma^2)^2} \tag{7.13}$$

$$\kappa = \frac{\mu_{\text{eff}} A' \alpha}{\hbar k} = \frac{2\sqrt{2}}{\pi} \frac{\mu_{\text{eff}} A_{\text{rms}} \alpha}{\hbar k} \cos\varphi \tag{7.14}$$

where δ_0 is the cooling laser detuning. Substituting the results of the fit described above yields a damping constant $\beta = \alpha/m \approx 400\ \text{s}^{-1}$ and a MO frequency $\omega = \sqrt{\kappa/m} \approx 2\pi \times 90$ Hz, as quoted in the main text. Here m is the mass of CaOH.

To estimate the capture velocity of a 3D MOT we use the full MO force profile described above with ζ and μ_{eff} fit to our data and use the same experimental parameters as in the fit. From this force profile, we numerically integrate the 1D equations of motion for a single molecule entering the 3D MOT along the molecular beam axis with variable initial velocity. The capture velocity is determined by finding the maximum initial velocity at which the molecular trajectory turns around (i.e. reaches negative forward velocity) before exiting the MOT volume defined by the cooling beams. We assume a 3D MOT beam diameter of 20 mm and uniform intensity. This results in an estimated on-axis capture velocity of $\lesssim 7$ m/s. Monte Carlo simulations performed in other work [147] suggest that this value will be reduced by a factor of ~ 2 when averaged over all molecules, which in general enter the 3D MOT away

from the central axis and experience different magnetic field and laser intensity profiles.

By fitting the final velocity distribution of the molecular cloud after propagation through the simulated cooling region, we extract transverse beam temperatures. After Doppler cooling alone we find $T = 3.1(1)$ mK (from an initial temperature of $T = 8.4(2)$ mK); with MO cooling and compression the temperature is further reduced to $T = 1.4(1)$ mK. The simulated MOT force is then used to extract an on-axis capture velocity of $\sim$ 7 m/s for a 3D MOT of CaOH, which is similar to that measured in diatomic molecules [108].

8

Outlook and future work

The recent progress and development of new platforms using laser cooled diatomic molecules to load magnetic traps [101, 100] and optical tweezers [72] serve as a roadmap of the techniques that may be applied to CaOH. Ultimately, the scientific goals of this work are to study the fundamental collisional properties of CaOH or develop a quantum simulation platform using laser-cooled polyatomic molecules to study unconventional quantum behavior [63] or implement a quantum computation platform using molecular qubits [71]. Progress towards these scientific goals necessitates the cooling and phase-space compression given by the realization of a full 3D MOT.

The work described in Chapter 7, enabled us to predict the capture velocity of a 3D MOT of CaOH to be $\sim$7 m/s. The velocity profile of the molecular beam in Section 4.7 has a mean

forward velocity of ∼100 m/s and a slow tail that extends to ∼50m/s, indicating that slowing must be applied in order to load a 3D MOT. A variety of slowing techniques have been proposed for molecules using combinations of electric and magnetic fields (e.g. modified Zeeman slower [121], optical Stark deceleration [219] , Zeeman deceleration [220], moving magnetic traps [117], whitelight slowing [123], chirped slowing [125], Zeeman-Sisyphus [120], and cryofuge [119]). The simplest technique to implement, whitelight slowing, uses radiation pressure force to decelerate molecules and is described below.

8.1 Whitelight slowing

Whitelight slowing uses an overdriven electro-optic modulator (EOM) to broaden a single frequency laser to address the molecular sub-structure (hyperfine and spin-rotation) and the change in Doppler shift as molecules are slowed to rest. The frequency of the EOM is chosen such that adjacent sidebands are spaced by less than the natural linewidth of the optical transition ($2\pi\times6.25$ MHz for CaOH). All optical frequencies used in the photon cycling scheme must be similarly broadened to prevent loss to dark vibrational states. The width of the frequency broadening determines the maximum velocity class that will be effectively slowed by this technique; however, additional broadening lowers the available laser intensity per unit frequency which reduces the scattering rate and lowers the deceleration of the molecules.

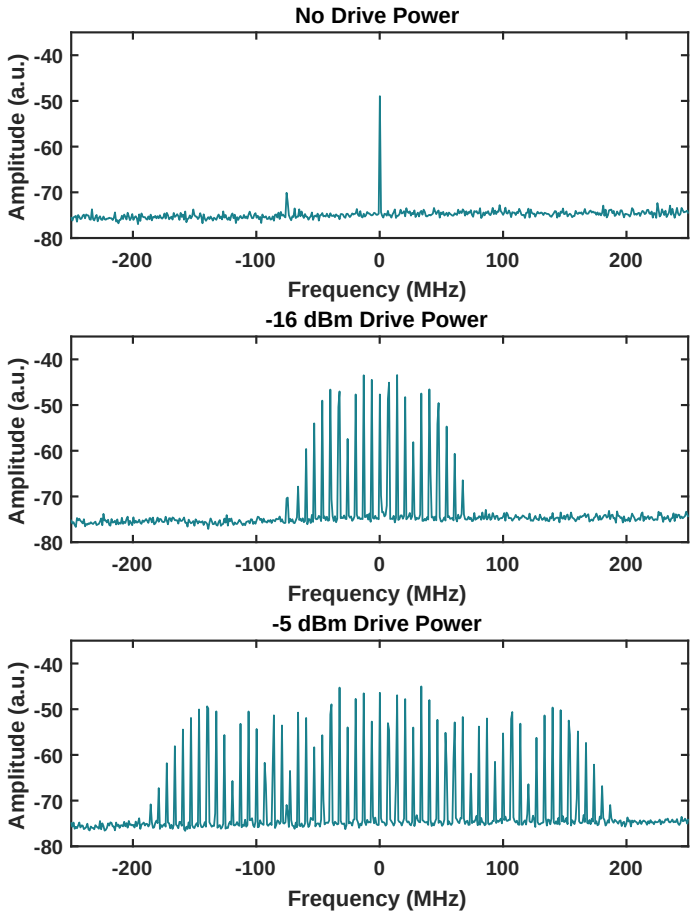

Figure 8.1: Frequency broadening of the whitelight EOM, under no drive (top), -16 dBM drive power (center), and -5 dBM drive power (bottom). The sidebands are spaced by 6.6 MHz for this configuration. adjusting the resonance condition to lower frequencies may be required for optimal whitelight slowing.

Figure 8.1 shows the spectrum of frequency sidebands produced by the overdriven EOM at several drive powers. The EOM crystal is Mg doped lithium niobate with dimensions of

1 mm x 1 mm x 6 cm, with two sides coated with Au and Cu electrodes to make electrical connections and apply a uniform electric field. In order to achieve high voltages to increase the modulation depth, this EOM is incorporated into a tunable resonant circuit with a Q = 250 at 6.53 MHZ. Operation at lower frequencies reduces the Q of the circuit (Q = 80 at 3.17 MHz).

Given a distribution of molecules with the velocity profile measured in Section 4.7, we must scatter $\sim 10^4$ photons to bring molecules at the peak of the velocity distribution to rest. The laser cooling scheme implemented to demonstrate a 1D magneto-optical trap allows scattering 2200^{+400}_{-300} photons with $\frac{1}{e}$ molecules remaining. Additional repumping lasers are required to increase the photon budget. GF matrix calculations employing the Sharp-Rosenstock approach [167, 210], are used to estimate higher order Franck-Condon factors. These calculations indicate that the next most significant vibrational decays occur to the $\widetilde{X}(300)$, $\widetilde{X}(12^00)$, and $\widetilde{X}(12^20)$ states. The hybrid $\widetilde{X}(12^00)$ and $\widetilde{X}(12^20)$ states have not been observed in the literature, and are highly perturbed by Fermi resonances with nearby vibrational states with the same symmetry. This pertrubation complicates spectroscopy and increases the vibrational branching to these states. Nevertheless, we have identified the repumping transitions that will enable us to recover molecular population lost to these vibrational states (see Appendix D for details). The laser cooling scheme proposed in Figure 8.2 is predicted to be closed to 10^{-5} level extending the photon budget to allow both laser slowing and the observation of a 3D MOT of CaOH molecules.

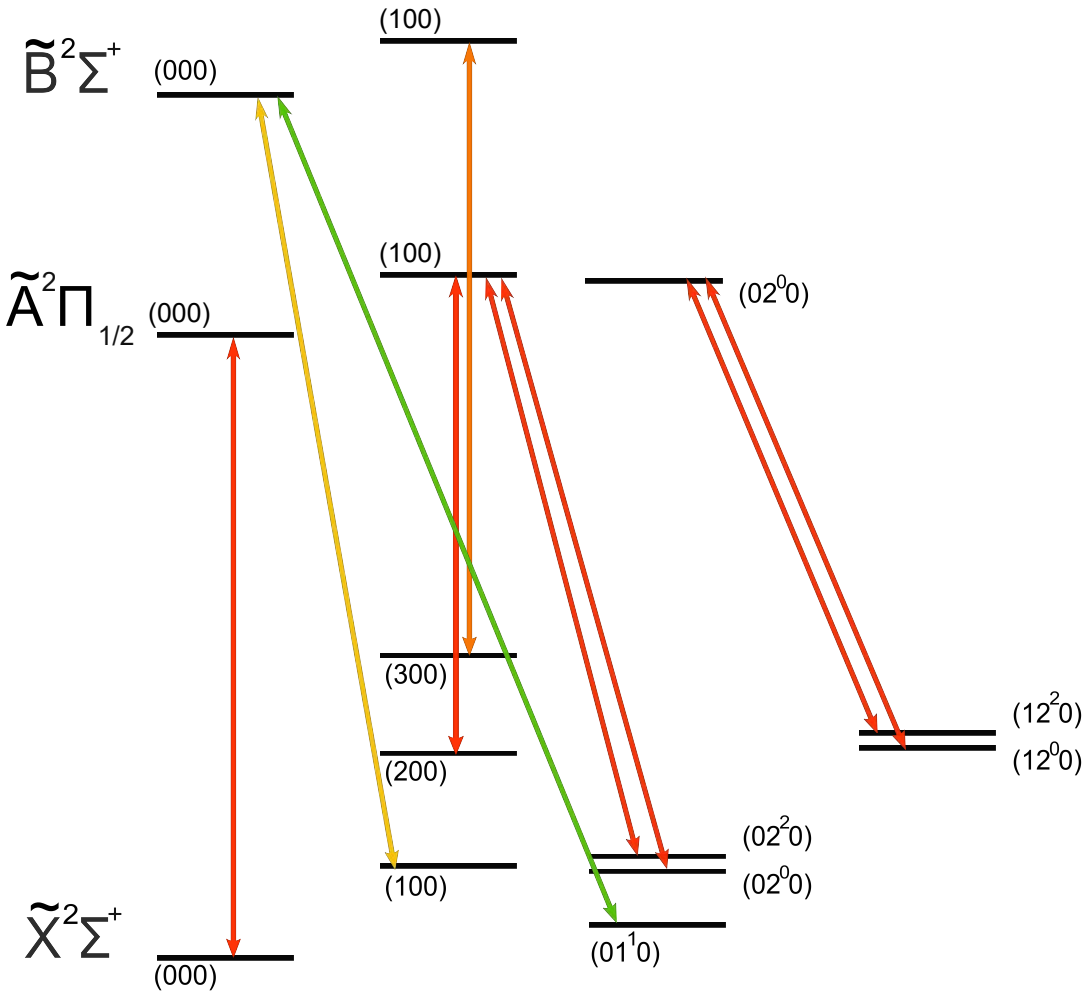

Figure 8.2: Proposed slowing and 3D MOT photon cycling scheme for CaOH. All transitions have been identified. The vibrational branching ratio out of this scheme is predicted to be on the order of 10^{-5}.

8.2 Detecting a 3D MOT

Extending our one dimensional results to a full 3D MOT should be a straightforward process provided sufficient numbers of molecules are effectively slowed below the capture velocity. The approach is to replicate the rf-MOT coil design used to trap CaF molecules [14]. Previous experience within the Doyle group, and the wider community, indicates that scattered light

is likely to obscure the signal from trapped molecules. As a result, we are taking a series of significant steps to reduce background scattered light. We have had the inside of our MOT chamber optically blackened with Acktar Magic Black to reduce scattered light as depicted in Figure 8.3.

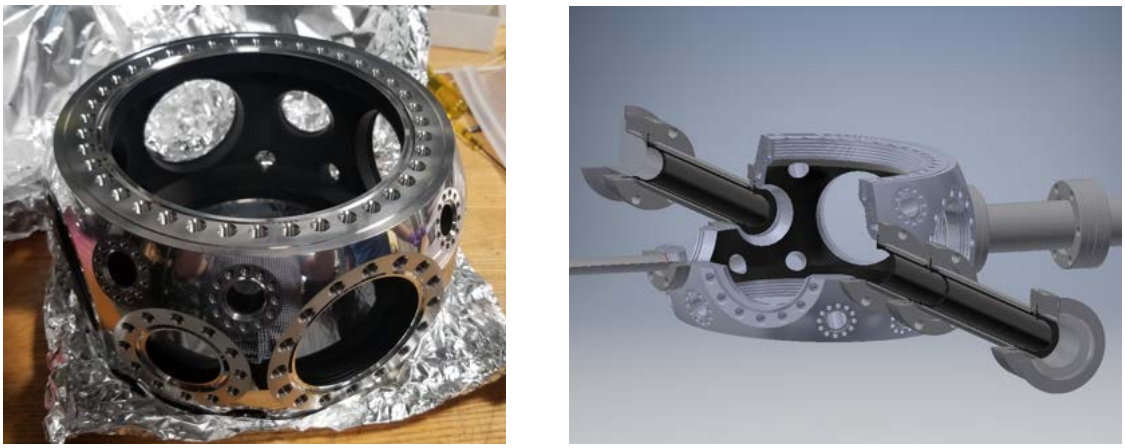

Figure 8.3: (left) Image of the Acktar Magic black coated vacuum chamber. (right) Machine drawing of the blackened vacuum chamber with blackened copper tubes and razor edge baffles.

In addition, custom antireflection coated vacuum windows are in production as the bulk of scattered light results from stray reflections off of the windows as well as diffuse scatter from contaminants or defects on the window surfaces. These windows replicate the design described in chapter 5 of ref. [14]. Copper tubes, with black cupric oxide surfaces [221] combined with razor-edge baffles, will also be implemented to further reduce scattered light. The in-vacuum rf-MOT coils will also be blackened with a vacuum compatible commercial paint (MH2200 paint from Alion formerly ECP2200 [222]). These techniques should be sufficient to detect and optimize a MOT of CaOH.

8.3 Methods to increase beam brightness

While not critical to the future work suggested above, increasing molecular beam brightness would accelerate the realization of a 3D MOT and allow rapid optimization of the experiment. Here I propose several techniques that may offer modest increases in molecule number, that may be implemented in parallel to slowing efforts.

The use of a magnetic lens to enhance on-axis density of molecules has been used in previous work to increase the number of molecules in a conservative trap [89]. This principle can be extended to the CaOH experiment. Trajectory simulations using magnetic fields generated by permanent magnets estimate a gain of $\sim$ 4x relative to an unfocused beam. If placed sufficiently close to the exit of the cell, this lens enables molecules to be simultaneously focused and slowed, working in tandem with whitelight slowing.

A simple alternative to the magnetic lens would be a short region of Sisyphus cooling near the exit of the cell. This technique has been demonstrated in systems similar to CaOH [20, 148, 32, 70]. The relative ease with which magnetically assisted Sisyphus cooling can be applied coupled with the rapid cooling that can be achieved with a small number of photons makes this a promising technique for increasing molecular beam flux. The major limitation of Sisyphus cooling is the capture velocity, typically $v_{Sis} \approx 1$ m/s. While the capture velocity of Sisyphus cooling is considered low, it exceeds the transverse velocity of the subset of molecules that will be slowed and trapped by a 3D MOT ($\approx$ 0.5m/s). Monte Carlo modeling of Sisyphus cooling indicates that there is a factor of $\sim$4-10 gain in molecule number available through application of 2D Sisyphus forces at the exit of the cell. Similarly, it may be possible to limit losses due to transverse plumbing with regions of transverse Sisyphus cooling during the application of whitelight slowing.

Rotational state measurements of our molecular beam indicate that there is significant pop-

ulation in the $\widetilde{\mathrm{X}}(000)(N=0)$ state. Rotational pumping into the $\widetilde{\mathrm{X}}(000)(N=1)$ rotational state can be accomplished with a simplified version of the technique used to brighten beams of ThO in the ACME eEDM measurement [223]. Microwaves at 20.05 GHz may couple the $(N=0, J=1/2)$ manifold to the $(N=1, J=3/2)$ manifold with simultaneous optical pumping into $(N=1, J=1/2)$ manifold through the $\widetilde{\mathrm{A}}(000)(J=1/2)$ state. The earth's magnetic field will provide remixing between M_J sublevels. Given the measured thermal distribution of our molecular beam, a 3-5 fold gain in molecule number is possible. Care should be taken such that the microwaves do not inadvertently couple the $(N=0)$ and $(N=1)$ states during application of the slowing light. If necessary a modest electric field may be applied to provide a spatially selective Stark shift so that the microwaves only couple molecules within region with an electric field.

8.4 Conclusions

Following magneto-optical trapping, sub-Doppler cooling will likely be required before loading the molecules into a optical dipole trap. Grey molasses cooling and Λ-enhanced sub-Doppler cooling are well understood and have been applied to diatomic species [109, 218, 205, 224, 225, 226, 227, 228, 229]. A trapped sample of CaOH molecules in a single rotational state will usher in a new frontier of quantum control over complex molecules. As discussed in Chapter 1, samples such as these could be used to construct novel quantum information [63, 230] or simulation [71] platforms, perform more stringent tests of the standard model [31], or exert quantum control over chemical processes [231, 232]. Alternatively, one could use the laser cooling techniques developed for CaOH and apply them to MOR species with larger pseudohalogen functional groups such as $CaOCH_3$. Magnetically assisted Sysiphus cooling has already been applied to $CaOCH_3$ [70], which is the first step on the road to full

laser cooling. While the vibrational complexity of these molecules is daunting, with straightforward extensions of laser cooling techniques demonstrated in this work one could imagine trapped ultracold samples of symmetric top or even chiral species, with full quantum control, and the power of optical detection.

A

626 nm laser system: Sum frequency generation

Solid state laser systems combined with nonlinear crystals form a powerful tool and can generate high power laser light across the optical spectrum. Several nonlinear techniques generate the laser light used in this work, including second harmonic generation (SHG) and sum frequency generation (SFG). While the SHG is incorporated as part of commercial laser systems, the SFG is used as part of an in-house laser system. This appendix will review the theory of nonlinear frequency mixing and describe setup and performance of the SFG laser system.

A.1 Theory of nonlinear frequency mixing

Nonlinear frequency mixing is a phenomenon that occurs in response to a light field interacting with the material through which it propagates. In order to describe this phenomenon we use the following relation between the polarization of the material $P(t)$ and the electric field of the incident light $E(t)$. While these properties in reality vectors, for the following treatment we will be using them as scalars[1].

$$P(t) = \varepsilon_0 \chi^{(1)} E(t) \tag{A.1}$$

Here ε_0 is the permittivity of free space and $\chi^{(1)}$ is the linear susceptibility, a property of the material. This material property is a tensor property that depends on the structure (if any) of the nonlinear material. This is a relatively simple relation and in order to describe nonlinear effects we use the full power series in $E(t)$.

$$P(t) = \varepsilon_0 \chi^{(1)} E(t) + \varepsilon_0 \chi^{(2)} E^2(t) + \varepsilon_0 \chi^{(3)} E^3(t) + \cdots \tag{A.2}$$

Where $\chi^{(2)}$ and $\chi^{(3)}$ are the second and third-order nonlinear optical susceptibilities, respectively.

Now let us examine the polarization as two electric fields with two distinct frequencies are present in the material. The electric field is represented as plane waves.

$$E(t) = E_1 e^{-i\omega_1 t} + E_2 e^{-i\omega_2 t} + c.c. \tag{A.3}$$

[1] For a more complete treatment please consult ref. [233].

We now collect terms that are associated with second order processes.

$$P^{(2)}(t) = \varepsilon_0\chi^{(2)}(E_1^2e^{-2i\omega_1 t} + E_2^2e^{-2i\omega_2 t} + 2E_1^*E_2e^{-i(\omega_1+\omega_2)t} + 2E_1E_2^*e^{-i(\omega_1-\omega_2)t} + c.c) + 2\varepsilon_0\chi^{(2)}(E_1E_1^* + E_2E_2^*) \tag{A.4}$$

Grouping terms by frequency dependence helps identify the types of nonlinear frequency mixing that may occur in this system. We will restrict this list to second harmonic generation (SHG) and sum frequency generation (SFG) terms.

$$\begin{aligned} P^{(2)}(2\omega_1) &= \varepsilon_0\chi^{(2)}E_1^2e^{-2i\omega_1 t} + c.c \qquad (SHG) \\ P^{(2)}(2\omega_2) &= \varepsilon_0\chi^{(2)}E_2^2e^{-2i\omega_2 t} + c.c \qquad (SHG) \\ P^{(2)}(\omega_1+\omega_2) &= 2\varepsilon_0\chi^{(2)}E_1E_2e^{-i(\omega_1+\omega_2)t} + c.c \qquad (SFG) \end{aligned} \tag{A.5}$$

These processes must conserve both energy and momentum to occur. While conservation of energy is apparent given the relations $E = h\omega$ and $\omega_3 = \omega_1 + \omega_2$ or $\omega_3 = 2\omega_1$. Instantaneous conservation of momentum is not sufficient to generate high power light. The phase of the instantaneously generated light must be matched to the phase of the previously generated light as it propagates through the crystal in order for it to be amplified. It requires care to engineer an environment that allows this phase matching to occur. As a result, typically only one of the above processes occurs efficiently in a given system.

As light propagates through a crystal the momentum ($\vec{p}$) of the light is related to the wavevector ($\vec{k}$) which incorporates the index of refraction (a function of wavelength and temperature) as follows:

$$\vec{p} = \hbar\vec{k} \tag{A.6}$$

given conservation of momentum we arrive at the following expression:

$$\begin{aligned} \vec{p_3} &= \vec{p_1} + \vec{p_2} \\ \vec{k_3} &= \vec{k_1} + \vec{k_2} \\ \Delta k &= \vec{k_1} + \vec{k_2} - \vec{k_3} \end{aligned} \tag{A.7}$$

Conservation of momentum leads to a conservation of wavevector and we have introduced Δk which is known as the wavevector mismatch. Δk can be related to the intensity of the generated field as it exits a nonlinear material [233].

$$I_3 = \frac{8 d_{eff}^2 \omega_3^4 I_1 I_2}{n_1 n_2 n_3 \varepsilon_0 c^2} (L^2 \mathrm{sinc}^2(\Delta k L/2)) \tag{A.8}$$

Here L is the length of the nonlinear material, n is the index of refraction for the indicated frequency, d_{eff} accounts for crystal orientation and represents the effective nonlinear optical susceptibility ($\chi^{(2)}$ is a tensor as a material may have different optical susceptibilities for a given crystal axis). The functional form of $\mathrm{sinc}^2(\Delta k L/2)$ is shown in Figure A.1. $\Delta k = 0$ is known as perfect phase matching. There is a loss in conversion efficiency as the the wavevector mismatch grows. Intuitively, energy flows from the pumping light fields (ω_1 and ω_2) into the generated light field (ω_3) but this energy flow is reversed when the generated light is out of phase with the pump fields. The degree to which the phase must be matched is set by the length of the nonlinear material $L \approx 1/\Delta k$.

A.2 Quasi-phase matching

There a variety of methods used to phase match a nonlinear crystal [234, 235, 236, 237] many of these techniques are susceptible to small deviations in alignment or strongly dependent on

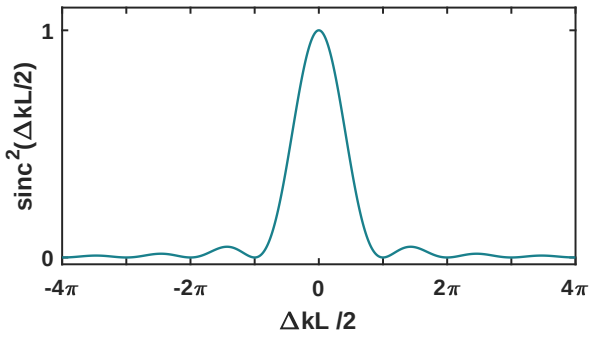

Figure A.1: The effect of wavevector mismatch on SHG or SFG efficiency

choice of nonlinear medium. Quasi-phase matching (QPM), the technique used for our SFG and SHG systems, relies on canceling out any accumulated phase mismatch by alternating domains within the nonlinear material [238]. This technique is primarily limited by fabrication technology which is rapidly improving. QPM is not based on birefringence so that any polarization may be used and the crystal may be oriented to make use of the largest component of the nonlinear susceptibilities tensor. Single pass conversion has been shown efficiently across a wide range of optical wavelengths [239, 240, 241, 242, 243].

In more detail, in a nonlinear material where the direction of the crystal axis is periodically inverted (periodically poled) one can compensate for the phase accumulated by the generated photons every polling period. Reversing the crystal axis changes the sign of the nonlinear optical susceptibility, this is equivalent to adding π to the phase of the generated photons. In such a system the phase matching condition requires the generated photons to accumulate a phase of pi every polling period. This effect can be seen in figure Figure A.2, which compares the intensity of light produced with perfect phase matching, quasi-phase matching, and no phase matching.

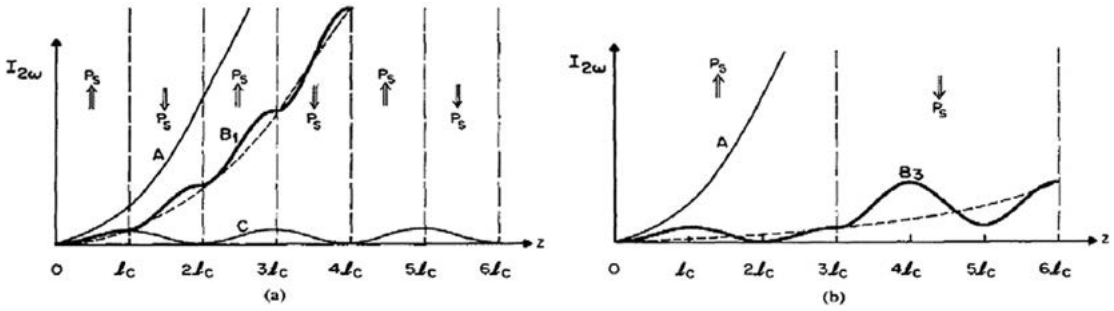

Figure A.2: (left) Comparison of perfect phase matching (A), Quasi-phase matching (B_1) and no phase matching (C). Material polarization is indicated by arrows labeled P_s. (right) comparison of quasi phase matching conditions of 3^{rd} order. A indicates 1^{st} order quasi phase matching and B_3 indicates 3^{rd} order, here phase matching occurs every m^{th} polling period. Image is reproduced from ref. [238]

This polling structure can be described as a change in d_{eff}, the effective nonlinear susceptibility as:

$$d_m = \frac{2d_{eff}\sin(\pi D)}{m\pi} \tag{A.9}$$

Where D is the duty cycling of the poling, and m is an odd integer. For the optimum QPM condition the d_m is reduced by a constant factor of $2/\pi$. The QPM condition can be applied over longer length scales at reduced efficiency as m increase. In large part this small reduction in d_m is offset by the ability to use materials with much larger natural nonlinear susceptibility. The effect of imperfections and fabrication techniques can be found here ref. [238].

A.3 Nonlinear crystal properties

There a number of materials commonly used for nonlinear applications. Common examples include lithium niobate (LN), magnesium oxide doped lithium niobate (MgO:LN), lithium tantalate (LT), potassium titanul phosphate (KTP), Beta barium borate (BBO), and Lithium triborate (LBO). From an end user perspective these materials differ primarily in the magnitude

Table A.1: Nonlinear susceptibility for common nonlinear materials [244]

Material:	MgO:LN	KTP	LBO	BBO
d_{eff}:	14pm/V	3.4 pm/V	2.5 pm/V	0.85pm/V

of the nonlinear susceptibility, damage threshold and mechanism by which damage occurs. The d_{eff} of commonly used materials summarized in Table A.1 [244].

Given the dramatic difference in nonlinear susceptibility it is clear that MgO:LN offers some substantial advantages over the other material for efficient nonlinear conversion. While doping LN with MgO provides a 4 orders of magnitude increase in the resistance to photorefractive damage [245], MgO:LN remains prone to photo-induced changes in the material properties, including changes in index of refraction [246] as well as changes in its absorption properties. Changes in the absorption properties are a larger concern and MgO:LN is susceptible to green-induced infrared absorption (GRIIRA) which can locally heat a crystal causing it to break [247]. This is a known issue at 532 nm but does not limit production of 626 nm light. While MgO:LN appropriate for most requirements, KTP can be used when visible light in the crystal is in the green. KTP is resistant to photorefractive damage but is susceptible to the formation of color centers when irradiated by visible light [238].

A.4 626 nm SFG system

Our 626 nm SFG system is modeled off of the system reported in [240]. We use two fiber amplifiers at 1053 nm and 1546 respectively from IPG Photonics that are seeded with NP Photonics seed lasers. These lasers are combined on a dichroic mirror (Thorlabs DMLP1180) before being focused through a 50 mm lens (Thorlabs LA4148-C) into a magnesium oxide

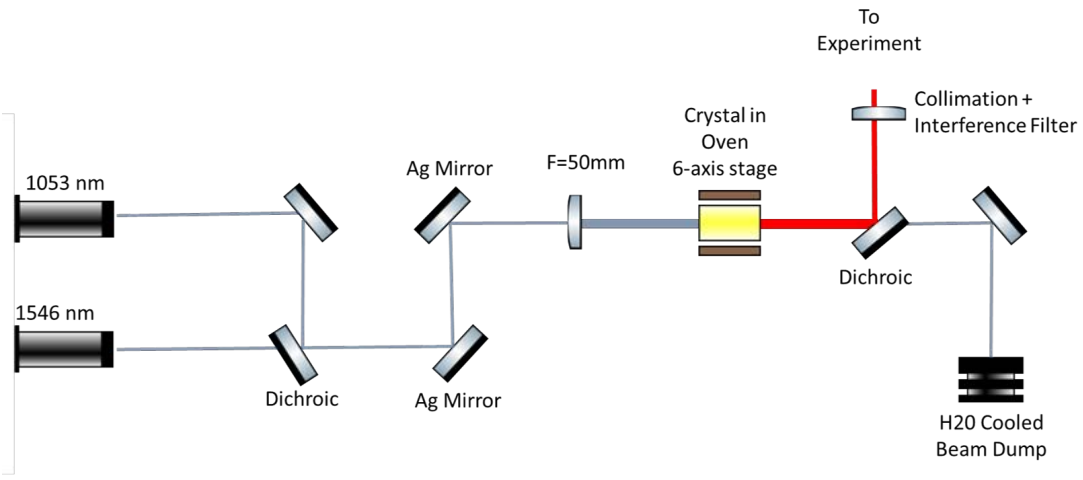

Figure A.3: Schematic diagram of the 626 nm SFG system. This image uses uses a vector graphics library created by Alexander Franzen.

doped lithium niobate crystal (Covesion MSFG637-0.5-40). The longest off-the-shelf crystal was chosen to increase conversion efficiency given the quadratic increase in SFG intensity with crystal length (Eq. A.8). We use the 11.75 μm polling period at $\sim$ 34 degrees C. We define the efficiency per unit length of our conversion :

$$\eta_{SFG} = \frac{P_{626}}{P_{1053} P_{1546} l_c} \tag{A.10}$$

The highest recorded output of this system is 7.8 Watts of 626 nm output power with 11 W (1053 nm) and 9 W (1546 nm) for an efficiency of 2.0% $W^{-1}cm^{-1}$. The highest efficiency of this system (5.1 % $W^{-1}cm^{-1}$) is comparable to the literature values [240, 243] and occurs at low input power. The loss in efficiency at higher powers is attributed to local heating of the SFG crystal which modifies Δk, lowering conversion efficiency.

A.4.1 Initial alignment

Pump laser focus

In order to reach these efficiencies a number of parameters must be carefully controlled. First, the focus of the laser beams strongly affects the optimum performance of this system. Boyd et. al. conducted a theoretical study of a Gaussian beam propagating through a nonlinear medium and concluded that the optimum conversion efficiency occurs when the ratio of confocal parameter to crystal length is equal to 2.85 [248]. Experimental sources in the literature indicate that small deviations from this value may further increase conversion efficiency [240, 243]. Given our 40 mm crystal length this means that optimum conversion occurs when the Rayleigh range of our lasers is 7.0 mm. In order to choose an appropriate lens we need to know the beam size of our pump lasers. In the absence of a ccd camera that was sensitive to both 1053 and 1546 nm light we conducted a razor blade beam waist measurement [249]. In this measurement the beam is slowly blocked with a razor blade mounted on a micrometer translation stage, the power transmitted past the razor is recorded and the resulting power vs. distance curve can be used to extract the beam width. The 1546 nm laser has a beam width of 1.32 mm and the 1053 nm laser has a beam width of 1.06 mm, consistent with the specifications from the vendors. This measurement is presented in figure Figure A.4.

Given these beam widths and the desired Rayleigh range, a lens focal length of 75 mm was identified as the optimum starting point. The system was tested with 100 mm, 75 mm and 50 mm lenses at low powers. There was a 10% increase in efficiency with the 50 mm lens which was selected for alignment at higher power.

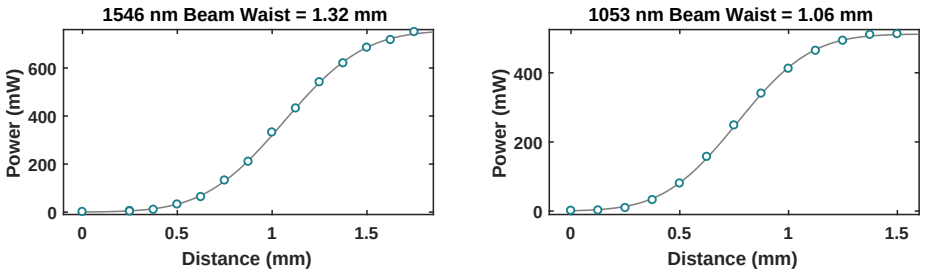

Figure A.4: Results of the razor blade beam width measurement for our 1053 nm and 1546 nm pump beams.

A.4.2 Coarse alignment and temperature tuning

Initial alignment of the crystal is straightforward as some SHG occurs regardless of the crystal temperature and at low pump powers (50 mW/beam) enough visible light is generated to see with the naked eye. SHG is most sensitive to the overlap of the pump beams. It is sufficient to overlap the pump beams over a $\sim$ 1 m lever arm using standard IR viewer cards. After ensuring that the combined beams are reasonably level with the optics table you can place the lens. Given the degrees of freedom available on our crystal mount we then align the lens to the combined beams by placing the lens such that the expanded beam is not substantially deflected, indicating the combined IR beams are reasonably close to the optical axis of the lens. Finally the crystal may be placed such that the beams are focused to the center of the crystal. By observing the beam shape of the transmitted IR light it is possible to coarsely align the crystal and produce visible light.

Once visible SHG light is present, the quasi-phase matching condition can be adjusted. Fine tuning for the phase matching condition given a fabricated periodically polled crystal structure is done with temperature. Within a material, the refractive index is a function of the wavelength of light and temperature. This means that light at different wavelengths travels at slightly different speeds through a given material, resulting in a change in the relative phase

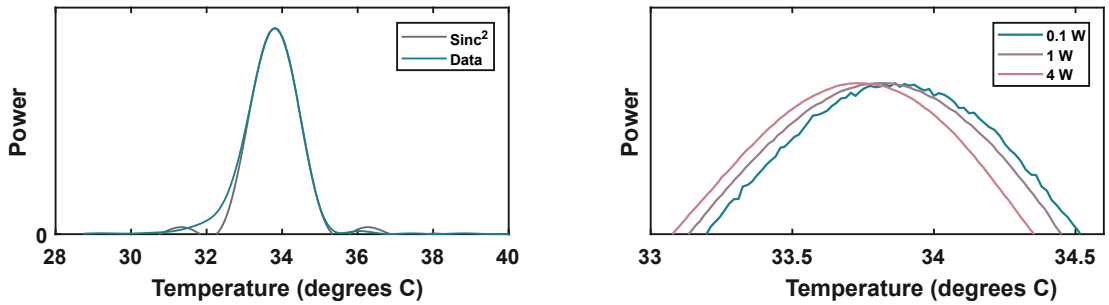

Figure A.5: (left) A single temperature vs. power curve with a fit to a sinc^2 overlaid. This data was taken by heating the crystal above the optimum conversion temperature and turning off the oven. Monitoring the SFG production as the crystal cooled to ambient temperatures. The deviation from the sinc^2 curve is typical for data collected in this manner and is likely due to the temperature gradients within the crystal. A more robust but time consuming measurement could be conducted where the crystal is left to thermalize at a series of temperature set points. (right) Expanded view of normalized SFG power vs. temperature at several powers. As the pump power is increased there we see a clear shift in the optimum towards lower temperatures. We attribute this to local heating within the crystal. This also leads to a loss of conversion efficiency for high pump powers. A crystal mount with better thermal conductivity to the crystal may improve performance of this system.

of different wavelengths of light. For given wavelengths, the temperature of the crystal may be scanned to tune to the phase matching condition $\Delta k = 0$) this effect is shown in figure Figure A.5. The optimum temperature value changes crystal to crystal as it compensates for small variations in the manufacturing process.

If this signal does not qualitatively match the functional form of $P(T) \propto \text{sinc}^2(T - T_{optimal})$ it is likely that there is an issue with alignment, since the angle of the pump beams through the crystal also changes the QPM condition. For instance, a common signature of misalignment is if there are two peaks that are equally efficient for conversion as temperature is scanned. Additionally, as the pump power is increased the optimum crystal temperature decreases. This indicates that there must be some local heating within the crystal due to the pump lasers and the oven temperature can be decreased to compensate for it.

A.5 Alignment procedure

We have empirically found that as the pump laser power is increased there is a change in beam pointing that we attribute to thermal lensing. Attempting to optimize the SFG system at low powers followed by jumping to high powers causes the alignment to shift substantially. In the past this has led to beam walking at high power which ultimately lead to misalignment of the pump lasers and destruction of a crystal. In response to this event a more cautious alignment procedure was developed. The system is aligned at low powers and the power is increased in steps (typically 50 mW, 1 W, 2 W, 4 W, full power), where the system undergoes alignment every time the power is increased. Following Eq. A.8 the expected performance of the system is expected to be proportional to both of the input pump powers:

$$P_{SFG} \propto P_{1053}\, P_{1546}\, \mathrm{sinc}^2(T - T_{optimal}) \tag{A.11}$$

The output of the system vs. pump power is shown in Figure A.6 and at low pump powers the performance is well described by the expected quadratic growth. For the fine alignment, it is important to not only monitor output power, but also to monitor the output beam shape. We have found that optimizing for power may result in optimize light produced due to a reflection off of the side of the periodically polled track within the crystal. This is especially insidious at low pump laser powers. This phenomenon is attributed to constructive interference of the pump lasers with its own reflection resulting in an increase in converted light. It is also important to realize that as the pump laser is steered through the nonlinear crystal the QPM condition will change slightly, possibly changing the optimum temperature of the crystal. With these considerations a detailed final alignment procedure is as follows:

SFG Alignment Procedure

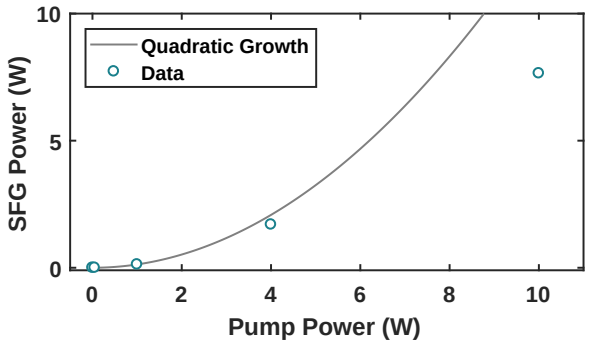

Figure A.6: SFG power vs. the input pump power(of a single pump beam). The pump laser powers are set to be equal. The expected quadratic performance describes the system well at low powers but at high pump powers we observe a loss of efficiency. We attribute this in large part to local heating within the crystal preventing the QPM condition to be met throughout the crystal. This could also be due to thermal lensing changing the focus of the pump lasers.

1. Read Section A.6.
2. Ensure the system is coarsely aligned as described in Section A.4.2
3. Optimize SFG as a function of the crystal temperature. The functional form should be $\propto \text{sinc}^2(T)$.
4. **ONLY at pump powers $\leq$ 1 W**
   (a) Walk the crystal angle(pitch, roll, and yaw) and relevant position (x,y) to optimize power, maintaining beam quality.
   (b) Ensure that the long crystal axis is parallel to the pump beam propagation
   (c) There will be "backward" propagating SFG light due to reflections off of crystal faces, align this light to the pump beam sources
   (d) Check alignment by looking for "symmetry" in misalignment when the pump light exits the periodically polled track.

5. Optimize SFG temperature again.
6. Carefully walk the overlap between the pump beams.
7. Carefully walk the beam position and pointing into the lens.
8. Optimize focus.
9. Carefully walk the overlap between the pump beams.
10. Carefully walk the beam position and pointing into the lens.
11. If this is the first attempt repeat steps 3 through 9.
12. Increase pump laser power. And repeat steps 3 through 9 as appropriate.
13. After alignment, The system should be maintained periodically by repeating alignment procedure at high powers.

A.6 Tips and tricks

- When aligning at high power monitor the crystal temperature. If this increases rapidly turn off pump lasers and repeat alignment at lower powers.
- As pump power increases, we have empirically found that the optimal focus location shifts towards the input facet of the crystal. At full power we observe the maximum converted light when the focus is approximately 1/3 into the crystal.
- As pump power increases the optimal temperature decreases.
- Proper alignment should transmit $\geq$ 97% of pump power limited only by the AR coating on the crystal.
- Proper alignment should maintain Gaussian beam profiles of pump beams with an aspect ratio (x:y) of no worse than 1:1.5
- Proper alignment should not cause continuous heating of the crystal. (the temperature should increase momentarily as the pumps are turned on)

- All crystals will be slightly different – efficiencies and optimal temperatures will vary.
- SFG alignment will influence pointing downstream. Compensate after alignment.

B

Cryogenic engineering references and techniques

B.1 Cryogenic references

The following references are excellent compilations of the cryogenic properties of commonly used materials in beam box design and best practices for cryogenic design.

- Lakeshore cryogenic reference tables (thermal conductivity, length contraction)
- NIST material properties database (thermal conductivity, specific heat, length contraction)

- Experimental Techniques for Low Temperature Design [162] (Everything you may need and more)
- Ref. [250] (outgassing of superinsulation).
- Nick's Sorb Write up
- Refs [163, 164, 251, 252] (charcoal sorbs)

B.2 Cryogenic heaters

There are a number of commercially produced cryogenic heaters that work well. However these heaters are expensive and typically come with few resistance options. It is best practice to use thin copper leads to power heaters which are poorly suited to large amount of current. As a result we often fabricate our own heaters with high resistances. This section will detail the creation of small $\sim$ 1 kΩ heaters, similar to what we use to heat the copper fill line and do diagnostic tests of the cooling capacity of our cryogenic system. These heaters are typically limited to $\leq$2 Watts. For larger heaters, commercial options are available and a robust custom option is described in ref. [253]. The process of making these heaters is described below.

A single heater requires the following materials:

- 1 Thin film resistor
- Two copper leads with PTFE (or other vacuum compatible) insulation $\sim$ 34 AWG
- electronic connector (Digikey ED10287-ND and mate ED10269-ND)
- Copper 10100 lug or mount
- 1 cm^2 vacuum compatible insulation (e.g. thin Kapton, fiberglass, cigarette paper)

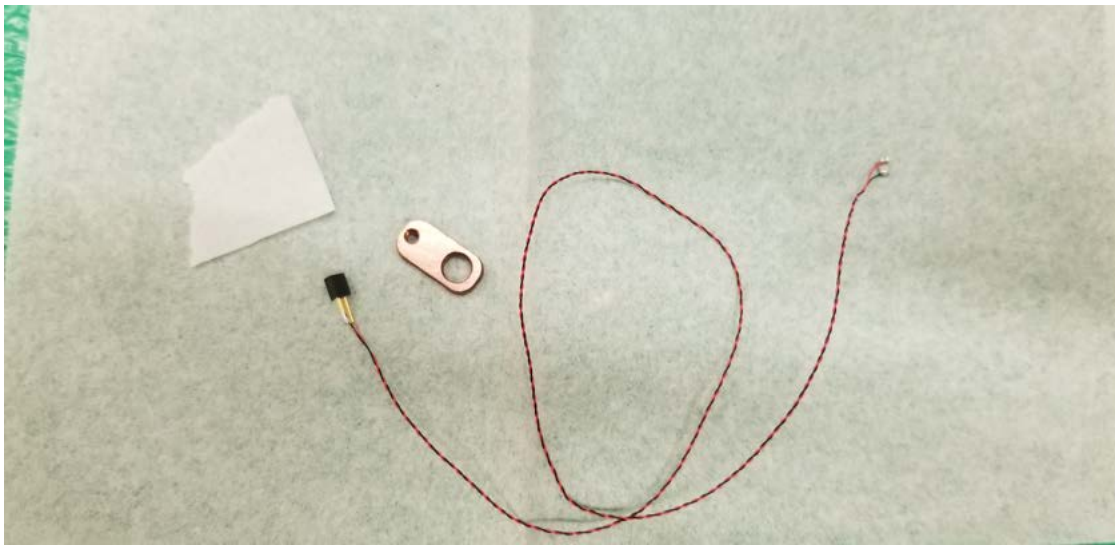

Figure B.1: Assembled components for a small cryogenic heater.

Thin film resistors are used because the resistance does not significantly change as the resistor is cooled to cryogenic temperatures. Typically we use small packages (1206 to 2512) that can be completely encapsulated in vacuum compatible epoxy to prevent out-gassing of materials. We standardize the cryogenic connectors throughout our experiment for modularity and these connectors have demonstrated successful performance after many temperature cycles.

- Solder the copper leads to the resistor and the electronic connector. Flux free solder is best for vacuum considerations.
- Prepare the copper mount by sanding it up to 600 grit for thermal contact and cleaned for vacuum.
- Mix a small batch of Stycast 2850 with catalyst 24LV and degas the epoxy twice to remove trapped air. This is accomplished with a small roughing pump and the epoxy is left under vacuum for $\sim$ 5 minutes.
- Apply a small amount of Stycast to the surface of the copper mount and cover with a thin layer of electrical insulation. The epoxy ensures good thermal contact and the insulation prevents a short.
- Apply a small amount of epoxy to the surface of the insulator and place the resistor on top. Use a syringe or small rod to place additional epoxy on top of the resistor taking

Figure B.2: (left) Copper mount with epoxy and electrical insulator. (center) The resistor is fully encased in epoxy. (right) The electrical connection has been strain relieved with epoxy.

care to cover any exposed electrical connections.

- Apply epoxy to the electrical connector to reinforce and insulate the solder joint on the electrical connector.
- Let cure for 24 hours.
- When the epoxy has cured, check the electrical connections to ensure the curing process did not damage the solder joints.

B.3 Wire heat sinking

Heat sinking wires for thermometers, heaters, and other diagnostic tools can be crucial to managing parasitic heat loads on cryogenic surfaces. Effective heat sinking for wires can be problematic as wires are typically coated with an electrical insulator with a correspondingly poor thermal conductivity. In addition, the surface to surface thermal contact is often proportional to the force holding the surfaces together, clamping the small wires used in cryogenic applications with sufficient force for good thermal conductivity often damages the wire.

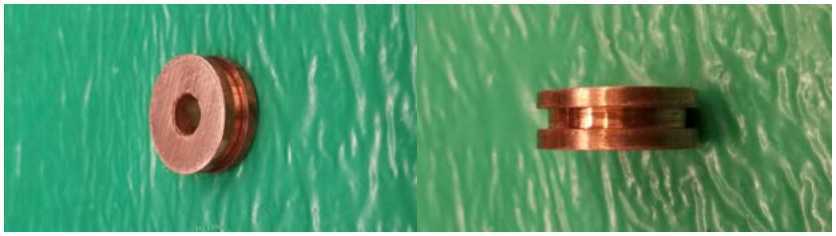

Figure B.3: Copper bobbin used for a wire heat sink. Center hole is a 10-32 screw hole, outer diameter is non-critical. The channel cut in the side makes it easy to wrap and epoxy the wire.

Figure B.4: Applying Stycast epoxy to a wire heat sink. (left) apply a small dot of epoxy to secure the wire. The ends of the wire are tensioned with tape. (right) The channel in the bobbin is flooded with epoxy to ensure a large surface area for thermal contact. The bobbin is elevated to ensure that the Stycast does not adhere to the working surface.

One effective method for effectively heat sinking wires is described below. It relies on encasing the wires in a matrix of thermally conductive epoxy (Stycast 2850 with catalyst 24LV) and thereby providing a large surface area to allow heat transfer from the wire to the cryogenic surface. These bobbins (Figure B.3) can be made easily on a lathe. The groove in the center of the bobbin holds the wire in place as it is wrapped around the bobbin.

Wrap ∼12 linear inches of wire around the copper bobbin before applying the Stycast epoxy. Copper wire is used to ensure good thermal conductivity. Applying epoxy is generally easier to accomplish in two steps depicted below in Figure B.4. First, apply a small dot of epoxy to secure the wire. once it sets, you can flood the channel with epoxy without the wire unraveling. The ends of the heat sink can be connectorized for either thermometers or heaters. The entire bobbin can be attached to a cryogenic surface through the center hole.

B.4 Flexible heat links

In order to thermally connect sensitive equipment and to prevent over constraining support structures within the cryogenic environment we use flexible heat links made of copper wire rope. The copper wire rope is from Cooner wire (part number NER7710836B-OFE) it is 2/0 AWG consisting of 5292 strands of 36 AWG wire for a total nominal diameter of 0.483 inches and an effective cross section of 0.1 inches^2 (0.67 cm^2). This wire is special ordered to be comprised of Cu10100 for high thermal conductivity.

> **Tip : Ordering New Wire**
>
> When ordering this wire it is critical to specify bare wire without any coating. Industry standard comes with a tin coating, this will interfere with the welding process.

In order to anchor the wire rope onto solid surfaces we connectorize the ends. While compressing the wire works to some extent, we have found welding the wire braid to connectors provides better thermal conductivity. The process is straightforward, although slightly modified from the procedures used in previous experiments [163].

- Begin by creating the connectors you want to attach.

> **Tip : Leave Room for Welding!**
>
> Remember the welded surface will not be flat. Figure B.5 demonstrates connectors with the thermal contact surface offset by 1/8” from the welding surface. Use 0.5” holes to accommodate 0.483” nominal diameter copper braid. Leave 3/8” from mounting holes to the weld features.

- String the connectors onto the copper braid before cutting the copper wire to length. This is often the most time consuming part of this process. If making multiple heat links, string all connectors (pay attention to orientation) before cutting the copper wire.
- Once connectors are on the copper braid, cut to length leaving $\sim$1 ” excess length per heat link.

- This excess copper can be removed after the first connection has been welded. With care a tolerance of $\leq$ 1/4" is reasonable on the length of copper braid.
- In preparation for welding, ensure $\sim$ 1/4" to 3/8" of braid extends above the welding surface.

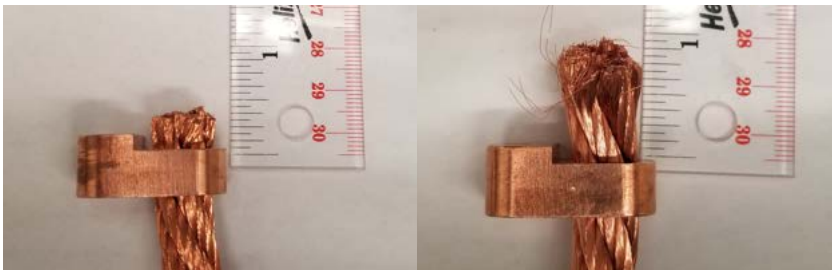

Figure B.5: (left appropriate level of excess copper braid for a compact weld finish. (right) After the first connector is welded, the second end can be trimmed to length. Note the 1/8" offset from the weld surface to the thermal connection surface.

- The weld is easily formed with a TIG welder set to DC(-) and $\sim$ 150 amps.
- Do not sit with legs or feet below the weld location. Molten copper may fall through the welding table. Thankfully my experience only resulted in some damage to a pair of sneakers.
- Following Figure B.6 from left to right. Arrange the connector in the vice such that it extends above the edges of the vice. The copper braid should hang freely.

Figure B.6: (left) Copper lug arranged to be welded. The connector is slightly above the surface of the vise so that the welding arc does not form to the vice. (center) Step 1, the copper braid has been melted into a solid mass. (right) The solid copper braid has been melted into the surface of the copper connector.

- First, apply the arc to the excess copper braid, melting the top into a solid mass of copper (center of Figure B.6). Full arc power can be used for this process.
- As the molten top of the copper braid nears the connector, begin to apply the arc to the connector attempting to join the molten braid to the connector.
- Once the molten copper braid joins the connector, use the TIG pedal to reduce the applied current and walk the weld puddle around the connector to ensure good penetration.
- The weld process will severely oxidize the copper braid, this oxide layer can be removed with an acid cleaning bath such as Citranox. (See Figure B.7)
- The surfaces making thermal contact should be refinished before use.

Figure B.7: The oxide formed during the welding process has been removed with an acid (typically Citranox) bath. This heat link is ready for installation.

We use Cu10100 for this process for high thermal conductivity. Welding will induce stresses in the material reducing the residual resistivity ratio. Annealing the welded braid would im-

prove thermal conductivity, however there are several difficulties when attempting to anneal these flexible heat links as described in ref. [163]. It is not necessary to anneal these flexible heat links before use.

B.5 Charcoal sorb creation

The charcoal adsorption pumps ("sorbs") used to maintain vacuum pressures in our experiment are made in house. There has been significant work done to study and characterize they pumping properties of charcoal [164, 251, 252]. The results of these studies indicate that charcoal made from coconut husks, with a grain size of 8-32 mesh has the best properties for our applications. This charcoal is epoxied onto copper 10100 plates in order to maintain temperatures. The process is described in ref. [163], and is presented in detail below.

> **Tip : Use New Charcoal!**
>
> The date when the charcoal was first exposed to atmosphere should be noted on the container. Do not use charcoal older than 1 year.

- Begin by preparing the copper plate for thermal contact and cleaning it for vacuum. If the sorb is double sided prepare both sides.
- Using Kapton tape (5 mil tape thickness is best), cover any areas of the copper plate where you do not want any charcoal sorb.
- Roughen the surface of the copper with low grit ($\leq$ 180) sandpaper wherever you will be applying epoxy.
- Mix a large batch of Stycast 2850 with catalyst 24LV and degas the epoxy twice to remove trapped air. This is accomplished with a small roughing pump and the epoxy is left under vacuum for $\sim$ 5 minutes.
- Paint the epoxy onto the roughened copper surface with a small brush. The layer of epoxy should be thick enough so that copper is not be visible through the epoxy.

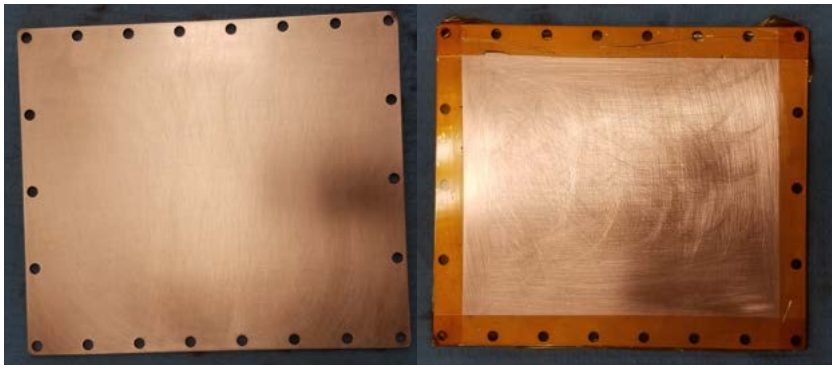

Figure B.8: (left) All copper surfaces have been sanded to high grit in preparation for good thermal contact. (right) Kapton tape has been used to mask thermal contact surface. The remaining copper has been roughened for better epoxy adhesion.

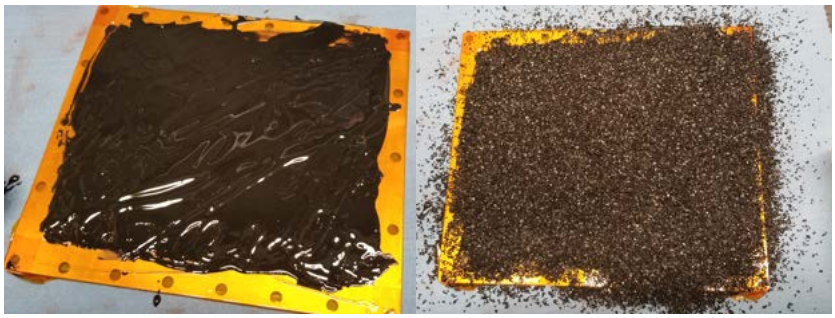

Figure B.9: (left) Stycast 2850 has been applied to the copper surface, no copper is exposed through the epoxy layer. (right) Charcoal has been dumped onto the epoxy coated surface, the weight of charcoal will ensure proper immersion in the epoxy.

- Pour coconut charcoal onto the epoxied surface to a depth of $\sim$ 1 cm. **Do not press the charcoal into the epoxy**.
- Let the epoxy cure for 24 hours.
- When the epoxy has cured, turn the sorb over and give it a sharp tap to dislodge any loose charcoal.
- Repeat with the opposite side.

C

Recirculating 1K system

As described in Chapter 3 the source of molecules is designed and built around a PT415 pulse tube in combination with a recirculating helium system that maintains consistent cooling capacity at temperatures as low as 1.6 Kelvin. This system allows continuous operation at low temperatures without the need for liquid cryogens. This section describes technical details of the recirculating He system and the issues we resolved in order to operate it reliably.

C.1 System as purchased

The following is a brief description of how the system operates when we consider a full cool down-warm up cycle from 300 K to 1 K and back to 300 K. Figure C.1 labels the components

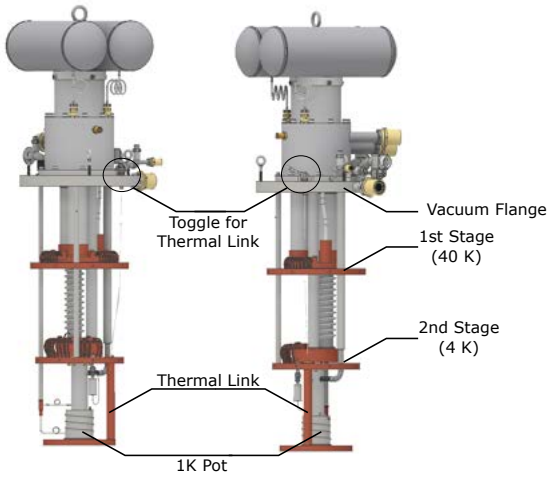

Figure C.1: Schematic diagram of the Cryomech PT415 with 1K system with important features labeled.

of the 1K system and Figure C.2 schematically illustrates the recirculating helium system. The recirculating 1K system does not provide active cooling until helium gas is liquefying on the 4K stage of the pulse tube and filling the 1K pot. In order to cool the 1K pot from room temperature a thermal link is made with the 4K stage of the pulse tube. This thermal link is made of a copper rod attached to a spring and a cable. When the cable is slack, the spring pushes the copper rod onto the 1K plate. In order to make good thermal contact the end of the copper rod that contacts the 1K plate is covered with indium. To break thermal contact the cable can be tensioned with a toggle compressing the spring and disconnecting the copper rod from the 1K plate. The vacuum feed through that allows the cable to be tensioned relies on a dynamic o-ring seal, meaning the o-ring moves along the sealing surface while maintaining a vacuum seal.

When the system is cold, helium is liquefied by the 4K stage and fills the 1K pot. The system pumps the He out of the 1K pot reducing the temperature of evaporation and providing evaporative cooling. In a stable state, there must be sufficient He in the 1K pot such that transient heat loads do not cause the pot to run dry. Experimentally we determined that a mini-

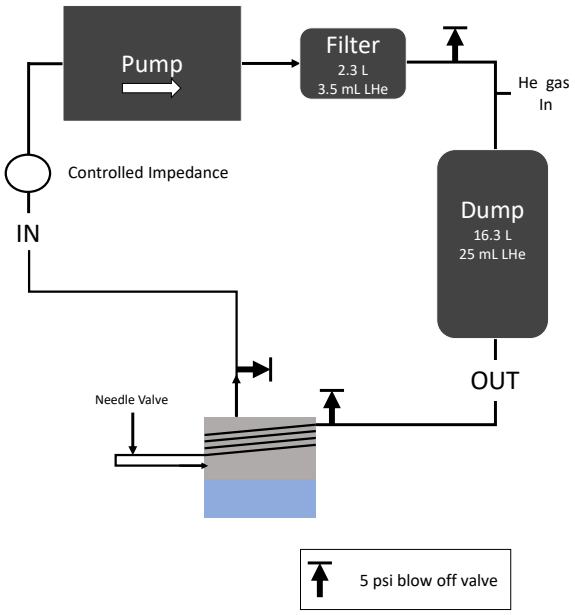

Figure C.2: Schematic diagram of the recirculating 1K system as received from Cryomech

mum of 75mL of liquid He is required for the system to operate as specified. Typically we operate with 100 mL of liquid He. This corresponds to the 1K pot being approximately half full. In addition it should be noted that the volume of the system is not large enough to contain the room temperature gas equivalent of 75 mL of liquid helium therefore, when the system is cold additional He gas must be added. This has the unfortunate side effect that the relief valves (blow off valves) on the system will open to vent excess gas every time the system returns to room temperature. Relief valves do not reseal every time they are activated. When we received this system, this was one of several issues that needed to be addressed for reliable operation:

- The dynamic o-ring for the thermal link feed through did not make a vacuum seal.

- The thermal link does not always make good thermal contact dramatically increasing cool down time.
- The He gas in the system arrived contaminated.
- Several components of the system arrived damaged with leaks
- Thermal cycling of the system required activation of blow off valves. Blow off do not always reseal.

Our group uses three of these systems and while each system had at least one major issue, the feedback provided to Cryomech seems to be improving quality control and design of these systems.

C.2 Modifications

Some of the issues we experienced were the result of low quality control and simple to address. For instance, the first issue we discovered was that as the thermal link is toggled the dynamic o-ring did not maintain a vacuum seal. This was resolved by removing the toggling mechanism, refinishing the sealing surface, and replacing the o-ring. While this was sufficient for our needs, a dynamic o-ring seal is not reliable. Past experience indicates that Viton fluroelastomer o-rings breakdown on the $\sim$3 year time scale and begin to fail. A much more robust method to resolve this issue would be to use a welded bellows to allow translation with a vacuum tight seal.

After the vacuum issue was resolved, we determined that the He system was contaminated. We made a series of modifications that allowed us to evacuate the system, leak check, and electronically log pressures in the system. We found that within the system, a number of vacuum connections had not been made properly and several vacuum bellows provided by Cryomech had significant leaks. This contributed to contamination to this system. We also added

a large volume (dump) to the system so that as the system came to room temperature the large volume of He gas could be accommodate without activating the relief valves. In addition fixing leaks, we added a liquid nitrogen cold trap to actively remove contamination from the system during operating. The cold trap was critical for operation while debugging the system. After identifying and removing all sources of contamination we operate without the cold trap. A full diagram of the modifications made to our system is shown in Figure C.3.

While our system has not had issues with the thermal link making good thermal contact, another system used in our group has repeatedly had issues. At the time of writing, they have redesigned the thermal link such that the thermal contact will be made by a ball-in-cone connection, at the time of writing the new thermal link has not been tested.

C.3 Suggestions for new systems

The modifications shown in Figure C.3 were made iteratively and some are a legacy of a previous configuration. While many of the modifications remain useful for diagnostic purposes, for a new system I would recommend the following changes in order of importance:

- **The addition of a pump out port** — The ability to evacuate the recirculating 1K system is absolutely critical. It is required for leak checking the system as well as removing contamination.
- **Pressure monitoring at the inlet and outlet of the pump (P6 and P1)** — We have found that monitoring the pressures in these locations has facilitated diagnose of a number of issues with the system including: clogs due to contamination freezing within the cryogenic section, excessive heat loads due to inadvertent thermal shorts, and identifying when a blow off valve may have activated.
- **The inclusion of a "dump"** — The dump serves two purposes. First, it prevents the blow off valves from activating when the system warms up to room temperature. Second, by recovering helium as outlined in Section C.4.2 contamination can be trapped

in the cold sections of the pulse tube and pumped out as the system warms up to room temperature.(It should be noted that as an alternative one could simply evacuate the system during warm up and replace the helium gas.)

C.4 Procedures

C.4.1 Liquefy helium and begin circulating

The purpose of this procedure is to load a known amount of helium into the 1K system. The starting configuration assumes that the 1K system is evacuated and that some helium is stored in Dump 1. This procedure does not make use of the cold trap. The following valves are assumed to be closed. v1, v3, v4, v6, v15, v8, v10, v20, v11, v13, and v15. These valves are not used during normal operation of our 1K system.

Initial Conditions — Helium is being stored in Dump 1 and the system is being evacuated with an external pump attached to v19. The pump in the 1K system is always on. The thermal link is down connecting the 1K and 4K stages of the pulse tube.

Open valves — v19,v7,v17,v16,v12,v9,v21

Closed valves — v5,v2,v18

Procedure

1. Ensure that the system is in the appropriate starting condition.
2. Close the valves v19,v7
3. Open v2,v18
4. Note pressure at p3 - We will be adding He until the pressure is 800-850 Torr
5. While monitoring p3, open v0 until the pressure reaches the desired level.

6. Close v0, v18.
7. Ensure the 1K system is cold.
    - The 2nd stage of the pulse tube should be below 4 K.
    - The 1st stage of the pulse tube should be below 40 K.
    - For our system the bottom of the 40K Shields should be below 60 K.
    - The 1K pot should be below 8K
    - All heaters should be off.
8. Monitor p1, we do not want to exceed 800 Torr.
9. While carefully monitoring p1, partially open v5.
    - Adjust v5 to maintain p1 pressure between 650-800 Torr
    - All temperatures should increase.
    - The 1K pot temperature will increase a few Kelvin. This is normal.
    - The 1K pot temperature should sharply decrease to below 4K.
    - The 1K pot temperature should then slowly rise to 4.2 K.
    - Wait until v5 is fully open and p1 is below 450 Torr.
10. Now we will begin to circulate.
11. Apply tension to the thermal link to remove the thermal connection.
12. Monitor p1, we do not want to exceed 800 Torr.
13. While monitoring p1, slowly open v16.
14. When v16 is fully open, begin heating the hot fill line.
15. System will come to equilibrium after $\sim$30 minutes.

C.4.2 Helium recovery and warm up

The purpose of this procedure is to recover a majority of the helium used in the operation of the 1K system. By recovering the He while the pulse tube is operational, we ensure that any contaminants are trapped in cold sections of the pulse tube and removed from the system. The following valves are assumed to be closed. v1, v3, v4, v6, v15, v8, v10, v20, v11, v13, and v15. These valves are not used during normal operation of our 1K system.

Initial Conditions–We begin by assuming that the system is actively circulating He. The re-circulating pump is on and the thermal link is disconnected.

Open valves — v2,v5,v17,v16,v12,v9,v21

Closed valves — v7,v18,v19

Procedure

1. Ensure that the system is in the appropriate starting condition.
2. Open v7.
3. Close v5, v12.
4. Apply a heat load to the 1K pot (250 mW).
5. Monitor the 1K pot temperature, when it jumps several Kelvin the pot is empty.
6. Turn off 1K heat load.
7. Turn on external pump connected to v19.
8. When p3 saturates, close v2, open v19 pumping out the system.
9. The contaminant free He is now stored in the dump.
10. Open v12.
11. Prepare the system for full warm up.
    - Close gate vale.

- Spin down and valve off all turbo pumps on beam box.
- Turn off all ion gauges.

12. Turn off PT415.
13. Wait until the sorbs reach 12 K, when the trapped He will be released.
14. Use a roughing pump to pump the helium out of the beam box.
15. Allow the beam box to come to room temperature.

    - This can be expedited with heaters on the radiation shields
    - A modest pressure of He gas (100 mTorr) will add conductive heat load.
    - Continue to evacuate the 1K system during warm up to remove potential contamination.

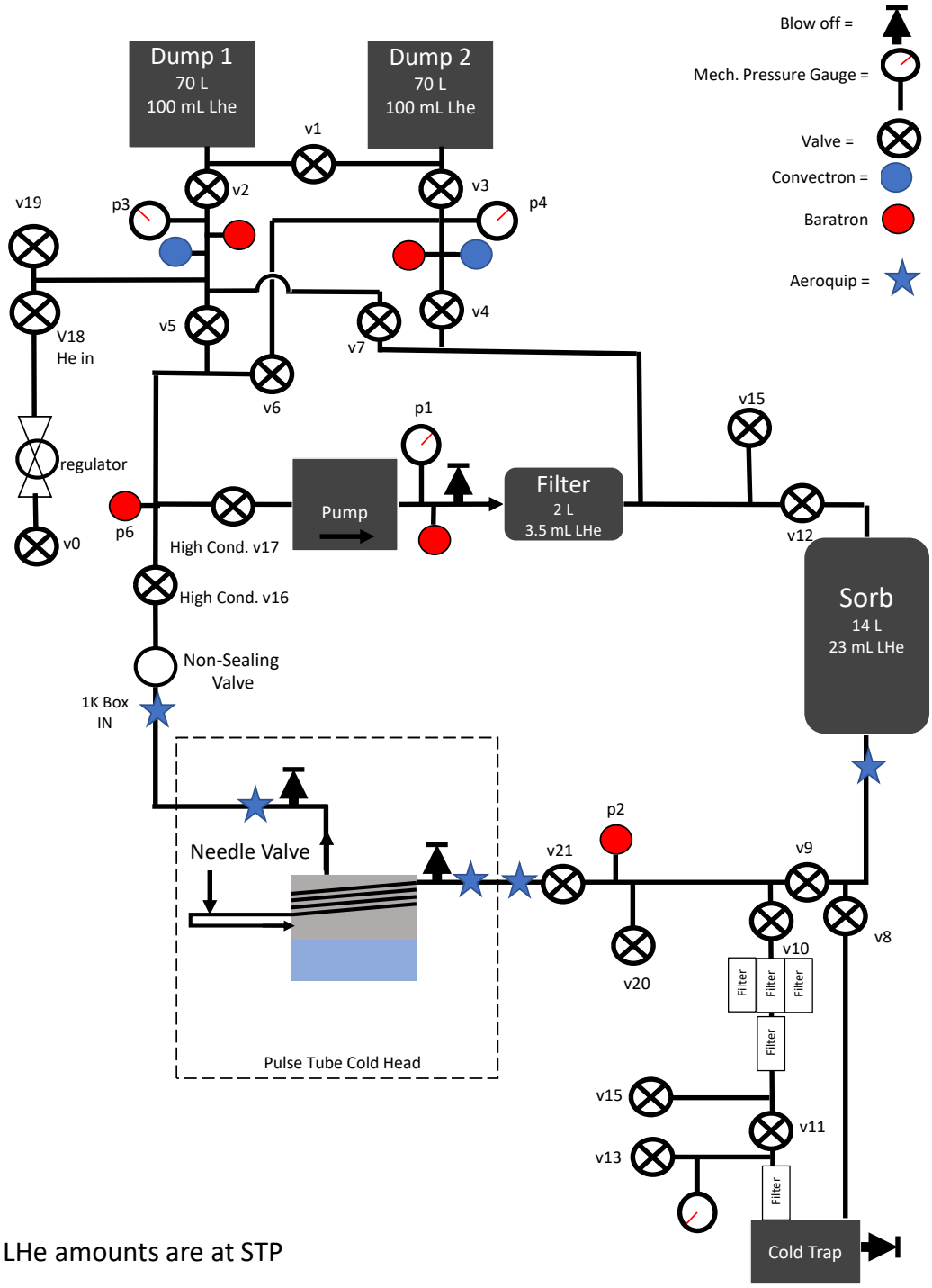

Figure C.3: Schematic diagram of our recirculating 1K system after extensive modification

D

CaOH spectroscopy

This appendix will list the vibrational spectroscopy performed during the course of this work. It will also summarize the techniques used to perform the spectroscopy. Typically, this spectroscopy is conducted using background free photon counting techniques where the detected spontaneously emitted photons can be optically filtered from the applied laser light. This is usually combined with optical pumping techniques to enhance the molecular population in the state of interest.

D.1 Repumper spectroscopy

D.1.1 $\widetilde{\mathrm{X}}(100) \rightarrow \widetilde{\mathrm{B}}(000)$

The $\widetilde{\mathrm{X}}(100) \rightarrow \widetilde{\mathrm{B}}(000)$ transition depicted in Figure D.1 was found by optically pumping molecules into the $\widetilde{\mathrm{X}}(100)$ state with the following laser scheme:

Optical Pumping Lasers

$$\widetilde{\mathrm{X}}(000) \rightarrow \widetilde{\mathrm{A}}(000)$$

Background free fluorescence is observed from spontaneous decay from the $\widetilde{\mathrm{B}}(000)$ state as molecules are repumped off-diagonally. The $\widetilde{\mathrm{X}}(100)$ has natural population that is $\sim$10% of the population of the $\widetilde{\mathrm{X}}(000)$ state.

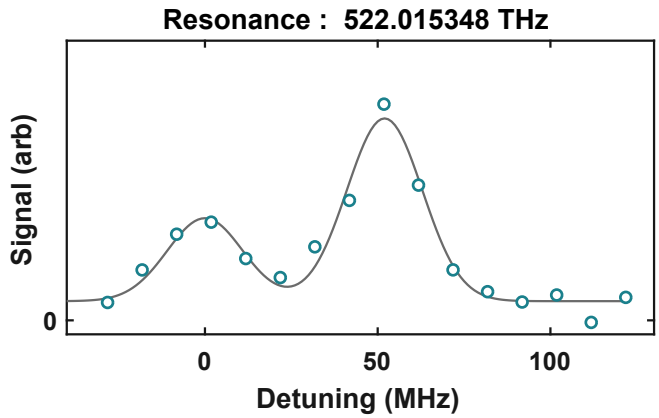

Figure D.1: $P_1(J'' = \frac{3}{2})$ (left) and ${}^{P}Q_{12}(J'' = \frac{1}{2})$(right) branches of the $\widetilde{\mathrm{X}}(100) \rightarrow \widetilde{\mathrm{B}}(000)$ repumping transition.

D.1.2 $\widetilde{\mathrm{X}}(200) \rightarrow \widetilde{\mathrm{A}}(100)$

The $\widetilde{\mathrm{X}}(200) \rightarrow \widetilde{\mathrm{A}}(100)$ transition depicted in Figure D.2 was found by optically pumping molecules into the $\widetilde{\mathrm{X}}(200)$ state with the following laser scheme:

Optical Pumping Lasers

$$\widetilde{\mathrm{X}}(000) \rightarrow \widetilde{\mathrm{A}}(000)$$

$$\widetilde{\mathrm{X}}(100) \rightarrow \widetilde{\mathrm{B}}(000)$$

$$\widetilde{\mathrm{X}}(02^{0}0) \rightarrow \widetilde{\mathrm{A}}(100)$$

The $\widetilde{\mathrm{X}}(200) \rightarrow \widetilde{\mathrm{A}}(100)$ repumping laser was scanned while observing the background free fluorescence due to the $\widetilde{\mathrm{X}}(100) \rightarrow \widetilde{\mathrm{B}}(000)$ repumping laser.

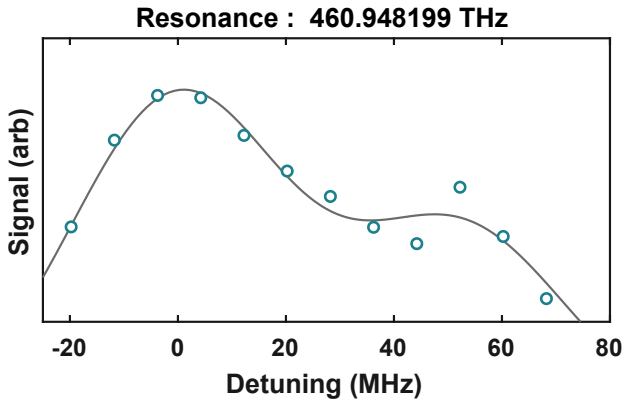

Figure D.2: $P_1(J'' = \frac{3}{2})$ (left) and ${}^{P}Q_{12}(J'' = \frac{1}{2})$(right) branches of the $\widetilde{\mathrm{X}}(200) \rightarrow \widetilde{\mathrm{A}}(100)$ repumping transition.

D.1.3 $\widetilde{\mathbf{X}}(300) \rightarrow \widetilde{\mathbf{B}}(100)$

The $\widetilde{\mathrm{X}}(300) \rightarrow \widetilde{\mathrm{B}}(100)$ transition depicted in Figure D.3 was detected using the natural population in the $\widetilde{\mathrm{X}}(300)$ state by observing the background free fluorescence due to the $\widetilde{\mathrm{X}}(300) \rightarrow \widetilde{\mathrm{B}}(100)$ repumping laser.

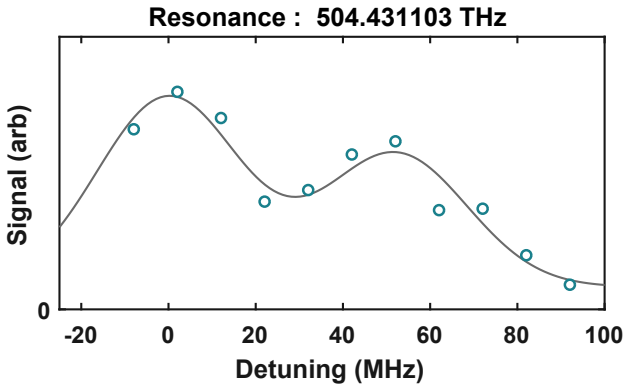

Figure D.3: $P_1(J'' = \frac{3}{2})$ (left) and ${}^{P}Q_{12}(J'' = \frac{1}{2})$(right) branches of the $\widetilde{\mathrm{X}}(300) \rightarrow \widetilde{\mathrm{B}}(100)$ repumping transition.

D.1.4 $\widetilde{\mathbf{X}}(02^{0}0) \rightarrow \widetilde{\mathbf{A}}(100)$

The $\widetilde{\mathrm{X}}(02^{0}0) \rightarrow \widetilde{\mathrm{A}}(100)$ transition depicted in Figure D.4 was found by optically pumping molecules into the $\widetilde{\mathrm{X}}(02^{0}0)$ state with the following laser scheme:

Optical Pumping Lasers

$$\widetilde{\mathrm{X}}(000) \rightarrow \widetilde{\mathrm{A}}(000)$$

$$\widetilde{\mathrm{X}}(100) \rightarrow \widetilde{\mathrm{B}}(000)$$

The $\widetilde{\mathrm{X}}(02^{0}0) \rightarrow \widetilde{\mathrm{A}}(100)$ repumping laser with a sideband at 52 MHz was scanned while observing the background free fluorescence due to the $\widetilde{\mathrm{X}}(100) \rightarrow \widetilde{\mathrm{B}}(000)$ repumping laser. The largest increase in detected fluorescence occurs when both spin-rotation states are addressed, and the smaller increases in fluorescence occur when only one of the spin-rotation components is addressed.

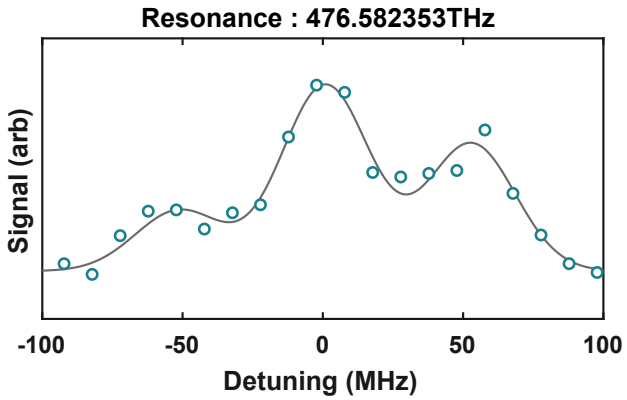

Figure D.4: $P_1(J'' = \frac{3}{2})$ (left) and ${}^{P}Q_{12}(J'' = \frac{1}{2})$(right) branches of the $\widetilde{\mathrm{X}}(02^{0}0) \rightarrow \widetilde{\mathrm{A}}(100)$. Large center feature occurs when both transitions are on resonance. The distinctive three peak structure occurs as two laser frequencies scan across two transitions.

D.1.5 $\widetilde{\mathbf{X}}(02^{2}0) \rightarrow \widetilde{\mathbf{A}}(100)$

The $\widetilde{\mathrm{X}}(02^{2}0) \rightarrow \widetilde{\mathrm{A}}(100)$ transition depicted in Figure D.5 was found by optically pumping molecules into the $\widetilde{\mathrm{X}}(02^{2}0)$ state by scattering photons with the $\widetilde{\mathrm{X}}(000) \rightarrow \widetilde{\mathrm{A}}(000)$ and $\widetilde{\mathrm{X}}(100) \rightarrow \widetilde{\mathrm{B}}(000)$ transitions. Following optical pumping, natural population left in the detection state ($\widetilde{\mathrm{X}}(100)$) was "cleaned out" by application of the $\widetilde{\mathrm{X}}(100) \rightarrow \widetilde{\mathrm{B}}(000)$ repumping laser. After the "clean out" step, the $\widetilde{\mathrm{X}}(02^{2}0) \rightarrow \widetilde{\mathrm{A}}(100)$ laser was applied to populate the $\widetilde{\mathrm{X}}(100)$ state which was subsequently detected with background free fluorescence due to the $\widetilde{\mathrm{X}}(100) \rightarrow \widetilde{\mathrm{B}}(000)$ laser.

There is no spin-rotation splitting for this branch as the presence of vibrational angular momentum ($l = 2$) restricts the rotational quantum number ($N \geq l = 2$). In the $\widetilde{\mathrm{X}}(02^{2}0)$, the selection rules governing J ($\Delta J = \pm 1, 0$) only permit the $J = 3/2$ component of the $N = 2$ to couple to the excited state ($\widetilde{\mathrm{A}}(000)(J = 1/2)$).

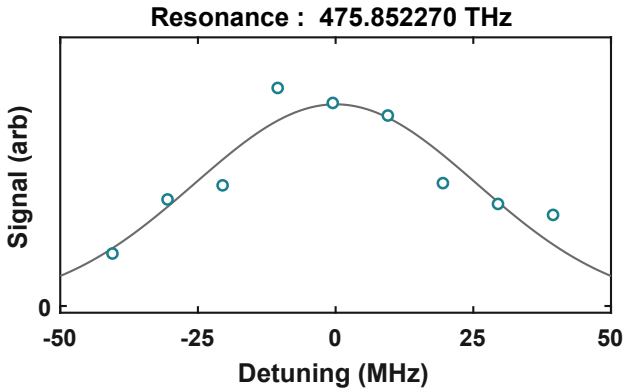

Figure D.5: $P_1(J'' = \frac{3}{2})$ branch of the $\widetilde{\mathrm{X}}(02^20) \rightarrow \widetilde{\mathrm{A}}(100)$ repumping transition.

D.1.6 $\widetilde{\mathbf{X}}(01^10) \rightarrow \widetilde{\mathbf{B}}(000)$

The $\widetilde{\mathrm{X}}(01^10) \rightarrow \widetilde{\mathrm{B}}(000)$ transition, shown in Figure D.6, was found by populating the $\widetilde{\mathrm{X}}(01^10)$ state through application of the $\widetilde{\mathrm{X}}(000) \rightarrow \widetilde{\mathrm{A}}(01^10)$ transition. The $\widetilde{\mathrm{X}}(01^10) \rightarrow \widetilde{\mathrm{B}}(000)$ transition was applied to recover molecular population. The resulting population in the $\widetilde{\mathrm{X}}(000)$ ground state was detected with photon cycling on the $\widetilde{\mathrm{X}}(000) \rightarrow \widetilde{\mathrm{A}}(000)$ transition using an electron multiplying ccd camera.

Curiously, we do not observe spin-rotation splitting of the $\widetilde{\mathrm{X}}(01^10)$ state. Most spectroscopic references [153, 146, 153, 157] simplify the spin-rotation interaction to:

$$H_{SR} = \gamma \vec{N} \cdot \vec{S} \tag{D.1}$$

However, upon investigation this expression is simplified and a more complete description is available in ref. [145] where there are modifications to this expression at low values of N states with $l \neq 0$. For N=1, we would expect a spin-rotation splitting $\frac{3}{2}\gamma = 52$ MHz in a typical $l = 0$ state but in $\widetilde{\mathrm{X}}(01^10)$ where $l = 1$ ref. [145] indicates a splitting of of $\frac{3}{4}\gamma = 26$

MHz. Figure D.6 shows two scans, one that does not appear to to resolve two peaks and one that is suggestive of the expected 26 MHz structure.

Given the experimental parameters, it is likely residual Doppler broadening or power broadening obscured this spectroscopic detail. Practically speaking, addressing this single feature with sufficient power appears to repump all molecular population that decays to $\widetilde{\mathrm{X}}(01^{1}0)$.

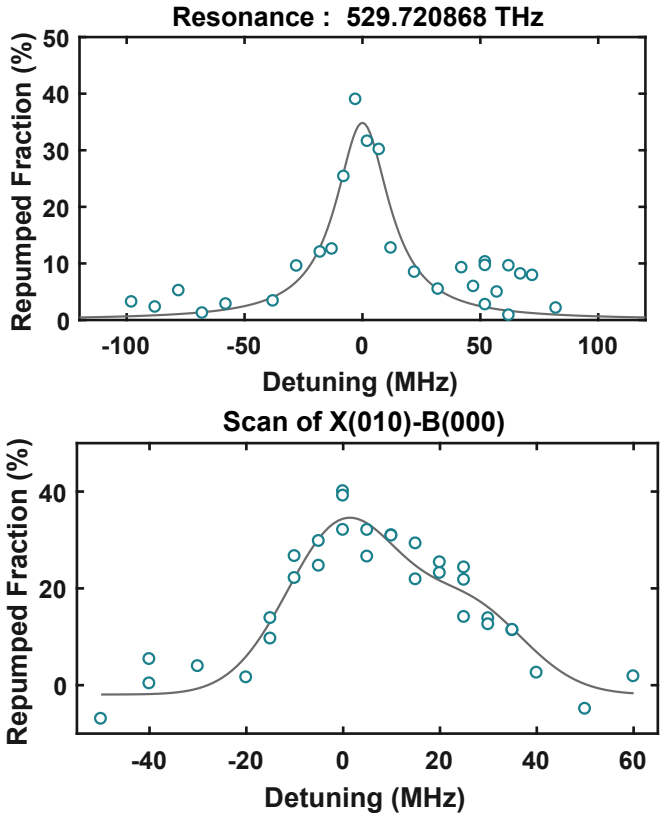

Figure D.6: $\widetilde{\mathrm{X}}(01^{1}0) \rightarrow \widetilde{\mathrm{B}}(000)$ Repumping spectrum. (top) fit to single peak, (bottom) fit to two peaks with 26 MHz splitting.

D.1.7 $\widetilde{\mathrm{X}}(12^{0}0) \rightarrow \widetilde{\mathrm{A}}(100)$

The $\widetilde{\mathrm{X}}(12^{0}0) \rightarrow \widetilde{\mathrm{A}}(100)$ transition depicted in Figure D.7 was found by optically pumping molecules into the $\widetilde{\mathrm{X}}(12^{0}0)$ state with the $\widetilde{\mathrm{X}}(000) \rightarrow \widetilde{\mathrm{A}}(02^{0}0)$ transition and relying on off diagonal decay. In the same location, natural population of the detection state ($\widetilde{\mathrm{X}}(100)$) was "cleaned out" by application of the $\widetilde{\mathrm{X}}(100) \rightarrow \widetilde{\mathrm{B}}(000)$ repumping laser. After the "clean out" step, the $\widetilde{\mathrm{X}}(12^{0}0) \rightarrow \widetilde{\mathrm{A}}(100)$ laser was applied to populate the $\widetilde{\mathrm{X}}(100)$ state, which was subsequently detected with background free fluorescence due to the $\widetilde{\mathrm{X}}(100) \rightarrow \widetilde{\mathrm{B}}(000)$ laser.

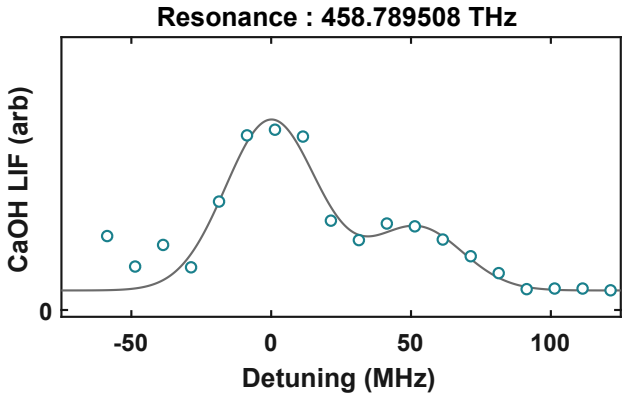

Figure D.7: $P_1(J'' = \frac{3}{2})$ (left) and ${}^{P}Q_{12}(J'' = \frac{1}{2})$(right) branches of the $\widetilde{\mathrm{X}}(12^{0}0) \rightarrow \widetilde{\mathrm{A}}(100)$ repumping transition.

D.1.8 $\widetilde{\mathrm{X}}(12^{2}0) \rightarrow \widetilde{\mathrm{A}}(100)$

The $\widetilde{\mathrm{X}}(12^{2}0) \rightarrow \widetilde{\mathrm{A}}(100)$ transition depicted in Figure D.8 was found by optically pumping molecules into the $\widetilde{\mathrm{X}}(12^{2}0)$ state with the $\widetilde{\mathrm{X}}(000) \rightarrow \widetilde{\mathrm{A}}(02^{2}0)$ transition relying on off diagonal decay. The signal was further enhanced by cycling photons on the $\widetilde{\mathrm{X}}(02^{2}0) \rightarrow \widetilde{\mathrm{A}}(02^{2}0)$ transition. In the same location, natural population of the detection state ($\widetilde{\mathrm{X}}(100)$) was "cleaned out" by application of the $\widetilde{\mathrm{X}}(100) \rightarrow \widetilde{\mathrm{B}}(000)$ repumping laser. After the "clean out" step, the

$\widetilde{\mathrm{X}}(12^20) \rightarrow \widetilde{\mathrm{A}}(100)$ laser was applied to populate the $\widetilde{\mathrm{X}}(100)$ state which was subsequently detected with background free fluorescence due to $\widetilde{\mathrm{X}}(100) \rightarrow \widetilde{\mathrm{B}}(000)$ laser.

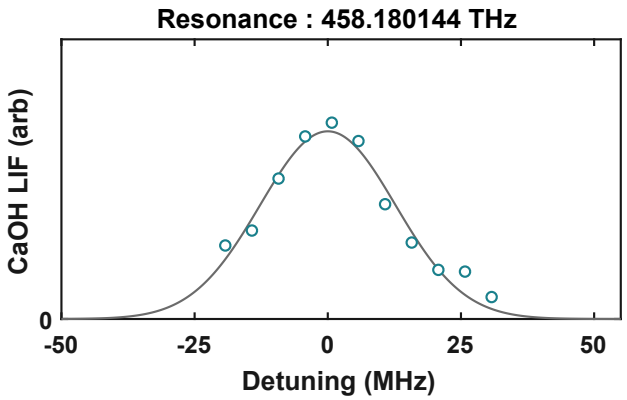

Figure D.8: $P_1(J'' = \frac{3}{2})$ branch of the $\widetilde{\mathrm{X}}(12^20) \rightarrow \widetilde{\mathrm{A}}(100)$ repumping transition.

D.2 Summary of known transitions

This section summarizes the transitions we found in the course of this experimental work. The frequencies listed in Table D.1 are referenced to our wavemeter (High Finesse WS7). We have empirically determined that the wavemeter can provide substantially more precision than specified by the manufacturer, however the accuracy is subject to a number of environmental parameters. Appendix B of ref. [14] provides an excellent description of the steps that should be taken to stabilize the wavemeter. In short, we continuously calibrate the wavemeter with a laser locked to an atomic reference, we exclusively use single mode fibers, and we have sealed the wavemeter in a large ISO nipple to prevent atmospheric pressure fluctuations.

The only other vibrational state known at high resolution in the literature is $\widetilde{\mathrm{X}}(400)$ [143], all other states are only known to several cm^{-1}, ref. [254] was an invaluable resource when performing broadband spectroscopy to determine the transition frequencies for the $\widetilde{\mathrm{X}}(12^{0}0)$ and $\widetilde{\mathrm{X}}(12^{2}0)$ vibrational repumpers.

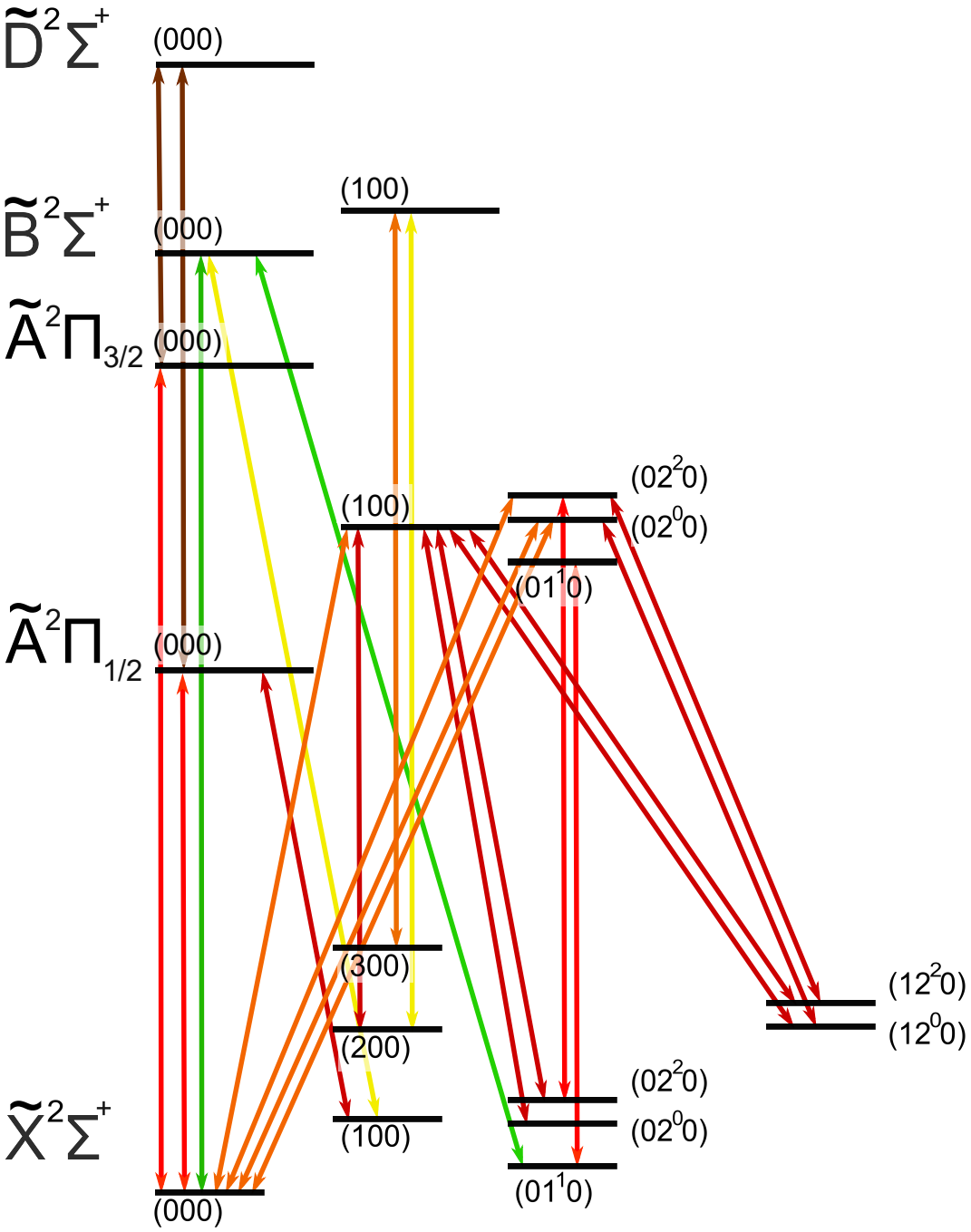

Figure D.9: All transitions of CaOH known to < 10 MHz. Transitions, frequencies and wavelengths are specified in Table D.1

Laser Transition	Wavelength (nm)	Resonance Frequency[1] (THz)
$\widetilde{X}(000) \rightarrow \widetilde{A}(000)$	626.4	478.600015
$\widetilde{X}(000) \rightarrow \widetilde{A}(100)$	602.9	497.227900
$\widetilde{X}(000) \rightarrow \widetilde{A}(01^10)$	613.1	488.947546
$\widetilde{X}(000) \rightarrow \widetilde{A}(02^00)$	600.6	499.117130
$\widetilde{X}(000) \rightarrow \widetilde{A}(02^20)$	595.8	503.172718
$\widetilde{X}(000) \rightarrow \widetilde{B}(000)$	554.9	540.273325
$\widetilde{X}(100) \rightarrow \widetilde{A}(000)$	651.2	460.342042
$\widetilde{X}(100) \rightarrow \widetilde{B}(100)$	574.3	522.015349
$\widetilde{X}(200) \rightarrow \widetilde{A}(100)$	650.4	460.948200
$\widetilde{X}(200) \rightarrow \widetilde{B}(000)$	594.8	503.993613
$\widetilde{X}(200) \rightarrow \widetilde{B}(100)$	574.1	522.203949
$\widetilde{X}(300) \rightarrow \widetilde{B}(100)$	594.3	504.431104
$\widetilde{X}(01^10) \rightarrow \widetilde{A}(000)$	640.5	468.029550
$\widetilde{X}(01^10) \rightarrow \widetilde{B}(000)$	566.0	529.702860
$\widetilde{X}(02^00) \rightarrow \widetilde{A}(000)$	654.6	457.954463
$\widetilde{X}(02^00) \rightarrow \widetilde{A}(100)$	629.0	476.582353
$\widetilde{X}(02^00) \rightarrow \widetilde{A}(02^20)$	621.3	482.527179
$\widetilde{X}(02^00) \rightarrow \widetilde{B}(000)$	576.9	519.627790
$\widetilde{X}(02^20) \rightarrow \widetilde{A}(100)$	630.0	475.852270
$\widetilde{X}(02^20) \rightarrow \widetilde{A}(02^20)$	622.2	481.797102
$\widetilde{X}(12^00) \rightarrow \widetilde{A}(100)$	653.4	458.789511
$\widetilde{X}(12^00) \rightarrow \widetilde{A}(02^00)$	650.5	460.878719
$\widetilde{X}(12^20) \rightarrow \widetilde{A}(100)$	654.3	458.180145
$\widetilde{X}(12^20) \rightarrow \widetilde{A}(02^00)$	651.6	460.069392
$\widetilde{X}(000) \rightarrow \widetilde{A}_{3/2}(000)$ 2-photon[2]	626.3	478.682785
$\widetilde{A}_{3/2}(000) \rightarrow \widetilde{D}(000)$ 2-photon[2]	820.4	365.419040

Table D.1: List of transition frequencies for CaOH. All transitions are the (N"=1) $\rightarrow$ (J'=1/2) laser cooling lines unless otherwise noted. Additional rotation lines not listed here have also been observed.

[1] Listed frequency is has a known offset when compared to the literature ($\sim$ -550 MHz). Our wavemeter is calibrated to a lithium saturation absorption crossover peak, with a nominal frequency of 446.799286 THz.

[2] ($\Omega' = 1/2,\ J' = 5/2$) This transition is used to avoid the confusion resulting from the spin-rotation frequency structure when performing Doppler-sensitive measurements.

References

[1] W. D. Phillips, Rev. Mod. Phys. **70**, 721 (1998).

[2] S. Chu, Rev. Mod. Phys. **70**, 685 (1998).

[3] E. A. Cornell and C. E. Wieman, Rev. Mod. Phys. **74**, 875 (2002).

[4] W. Ketterle, Rev. Mod. Phys. **74**, 1131 (2002).

[5] H. L. Bethlem, G. Berden, F. M. Crompvoets, R. T. Jongma, A. J. Van Roij, and G. Meijer, Nature **406**, 491 (2000).

[6] J. D. Weinstein, R. DeCarvalho, T. Guillet, B. Friedrich, and J. M. Doyle, Nature **395**, 148 (1998).

[7] S. A. Moses, J. P. Covey, M. T. Miecnikowski, B. Yan, B. Gadway, J. Ye, and D. S. Jin, Science **350**, 659 (2015).

[8] A. D. Ludlow, M. M. Boyd, J. Ye, E. Peik, and P. O. Schmidt, Rev. Mod. Phys. **87**, 637 (2015).

[9] I. Bloch, J. Dalibard, and S. Nascimbene, Nat. Phys. **8**, 267 (2012).

[10] R. Krems, B. Friedrich, and W. C. Stwalley, *Cold molecules: theory, experiment, applications* (CRC press, 2009).

[11] J. L. Bohn, A. M. Rey, and J. Ye, Science **357**, 1002 (2017).

[12] S. A. Moses, J. P. Covey, M. T. Miecnikowski, D. S. Jin, and J. Ye, Nat. Phys. **13**, 13 (2017).

[13] L. D. Carr, D. DeMille, R. V. Krems, and J. Ye, New J. Phys. **11**, 055049 (2009).

[14] L. Anderegg, *Ultracold molecules in optical arrays: from laser cooling to molecular collisions*, Ph.D. thesis, Harvard University (2019).

[15] M. Quack, Angew. Chem. **41**, 4618 (2002).

[16] M. Quack, Angew. Chem. **28**, 571 (1989).

[17] D. G. Blackmond, Philos. Trans. R. Soc. B **366**, 2878 (2011).

[18] I. Kozyryev, L. Baum, K. Matsuda, and J. M. Doyle, ChemPhysChem **17**, 3641 (2016).

[19] S. F. Rice, H. Martin, and R. W. Field, J. Chem. Phys. **82**, 5023 (1985).

[20] E. S. Shuman, J. F. Barry, and D. DeMille, Nature **467**, 820 (2010).

[21] L. Anderegg, B. L. Augenbraun, E. Chae, B. Hemmerling, N. R. Hutzler, A. Ravi, A. Collopy, J. Ye, W. Ketterle, and J. M. Doyle, Phys. Rev. Lett. **119**, 103201 (2017).

[22] V. Zhelyazkova, A. Cournol, T. E. Wall, A. Matsushima, J. J. Hudson, E. Hinds, M. Tarbutt, and B. Sauer, Phys. Rev. A **89**, 053416 (2014).

[23] M. T. Hummon, M. Yeo, B. K. Stuhl, A. L. Collopy, Y. Xia, and J. Ye, Phys. Rev. Lett. **110**, 143001 (2013).

[24] W. Duley and T. Millar, Astrophys. J. **220**, 124 (1978).

[25] T. Tsuji, Astron. Astrophys. **23**, 411 (1973).

[26] P. Pesch, Astrophys. J. **174**, L155 (1972).

[27] A. Collaboration *et al.*, Nature **562**, 355 (2018).

[28] W. B. Cairncross, D. N. Gresh, M. Grau, K. C. Cossel, T. S. Roussy, Y. Ni, Y. Zhou, J. Ye, and E. A. Cornell, Phys. Rev. Lett. **119**, 153001 (2017).

[29] E. R. Meyer and J. L. Bohn, Phys. Rev. A **78**, 010502 (2008).

[30] M. Tarbutt, B. Sauer, J. Hudson, and E. Hinds, New J. Phys. **15**, 053034 (2013).

[31] I. Kozyryev and N. R. Hutzler, Phys. Rev. Lett. **119**, 133002 (2017).

[32] B. L. Augenbraun, Z. D. Lasner, A. Frenett, H. Sawaoka, C. Miller, T. C. Steimle, and J. M. Doyle, New J. Phys. (2020), https://doi.org/10.1088/1367-2630/ab687b.

[33] M. G. Kozlov and S. A. Levshakov, Annalen der Physik **525**, 452 (2013).

[34] A. Shelkovnikov, R. J. Butcher, C. Chardonnet, and A. Amy-Klein, Phys. Rev. Lett. **100**, 150801 (2008).

[35] P. Jansen, H. L. Bethlem, and W. Ubachs, J. Chem. Phys. **140**, 010901 (2014).

[36] J. Bagdonaite, P. Jansen, C. Henkel, H. L. Bethlem, K. M. Menten, and W. Ubachs, Science **339**, 46 (2013).

[37] D. DeMille, S. Sainis, J. Sage, T. Bergeman, S. Kotochigova, and E. Tiesinga, Phys. Rev. Lett. **100**, 043202 (2008).

[38] M. Gacesa and R. Côté, J. Mol. Spec **300**, 124 (2014).

[39] S. Truppe, R. Hendricks, S. Tokunaga, H. Lewandowski, M. Kozlov, C. Henkel, E. Hinds, and M. Tarbutt, Nat. Commun. **4**, 1 (2013).

[40] I. Kozyryev, Z. Lasner, and J. M. Doyle, arXiv (2018), https://arxiv.org/abs/1805.08185.

[41] J. Croft, N. Balakrishnan, and B. Kendrick, Phys. Rev. A **96**, 062707 (2017).

[42] S. Stellmer, B. Pasquiou, R. Grimm, and F. Schreck, Phys. Rev. Lett. **110**, 263003 (2013).

[43] H.-I. Lu, I. Kozyryev, B. Hemmerling, J. Piskorski, and J. M. Doyle, Phys. Rev. Lett. **112**, 113006 (2014).

[44] J. Lim, M. D. Frye, J. M. Hutson, and M. Tarbutt, Phys. Rev. A **92**, 053419 (2015).

[45] M. Morita, J. Kłos, A. A. Buchachenko, and T. V. Tscherbul, Phys. Rev. A **95**, 063421 (2017).

[46] L. D. Augustovičová and J. L. Bohn, New J. Phys. **21**, 103022 (2019).

[47] G. Quéméner and J. L. Bohn, Phys. Rev. A **93**, 012704 (2016).

[48] A. Gorshkov, P. Rabl, G. Pupillo, A. Micheli, P. Zoller, M. Lukin, and H. Büchler, Phys. Rev. Lett. **101**, 073201 (2008).

[49] R. V. Krems, *Molecules in electromagnetic fields: from ultracold physics to controlled chemistry* (John Wiley & Sons, 2018).

[50] A. Klein, Y. Shagam, W. Skomorowski, P. S. Żuchowski, M. Pawlak, L. M. Janssen, N. Moiseyev, S. Y. van de Meerakker, A. van der Avoird, C. P. Koch, *et al.*, Nat. Phys. **13**, 35 (2017).

[51] S. Ospelkaus, K.-K. Ni, D. Wang, M. De Miranda, B. Neyenhuis, G. Quéméner, P. Julienne, J. Bohn, D. Jin, and J. Ye, Science **327**, 853 (2010).

[52] M. T. Hummon, T. V. Tscherbul, J. Kłos, H.-I. Lu, E. Tsikata, W. C. Campbell, A. Dalgarno, and J. M. Doyle, Phys. Rev. Lett. **106**, 053201 (2011).

[53] M.-G. Hu, Y. Liu, D. Grimes, Y.-W. Lin, A. Gheorghe, R. Vexiau, N. Bouloufa-Maafa, O. Dulieu, T. Rosenband, and K.-K. Ni, Science **366**, 1111 (2019).

[54] I. C. Lane, Phys. Chem. Chem. Phys. **14**, 15078 (2012).

[55] N. Wells and I. C. Lane, Phys. Chem. Chem. Phys. **13**, 19036 (2011).

[56] R. J. Crossley, *Chirality and biological activity of drugs*, Vol. 7 (CRC Press, 1995).

[57] E. J. Ariëns, Med. R. Rev. **6**, 451 (1986).

[58] B. Gadway and B. Yan, J. Phys. B **49**, 152002 (2016).

[59] M. A. Baranov, Phys. Rep. **464**, 71 (2008).

[60] A. Micheli, G. Brennen, and P. Zoller, Nat. Phys. **2**, 341 (2006).

[61] H. Büchler, A. Micheli, and P. Zoller, Nat. Phys. **3**, 726 (2007).

[62] N. Y. Yao, C. R. Laumann, A. V. Gorshkov, S. D. Bennett, E. Demler, P. Zoller, and M. D. Lukin, Phys. Rev. Lett. **109**, 266804 (2012).

[63] M. Wall, K. Maeda, and L. D. Carr, New J. Phys. **17**, 025001 (2015).

[64] D. DeMille, Phys. Rev. Lett. **88**, 067901 (2002).

[65] S. Yelin, K. Kirby, and R. Côté, Phys. Rev. A **74**, 050301 (2006).

[66] M. Karra, K. Sharma, B. Friedrich, S. Kais, and D. Herschbach, J. Chem. Phys. **144**, 094301 (2016).

[67] M. Ortner, Y. Zhou, P. Rabl, and P. Zoller, Quantum Inf. Process. **10**, 793 (2011).

[68] J. Zhu, S. Kais, Q. Wei, D. Herschbach, and B. Friedrich, J. Chem. Phys. **138**, 024104 (2013).

[69] K.-K. Ni, T. Rosenband, and D. D. Grimes, Chem. Sci. **9**, 6830 (2018).

[70] D. Mitra, N. B. Vilas, C. Hallas, L. Anderegg, B. L. Augenbraun, L. Baum, C. Miller, S. Raval, and J. M. Doyle, "Direct laser cooling of a symmetric top molecule," (2020), arXiv:2004.02848 .

[71] P. Yu, L. W. Cheuk, I. Kozyryev, and J. M. Doyle, New J. Phys. **21**, 093049 (2019).

[72] L. Anderegg, L. W. Cheuk, Y. Bao, S. Burchesky, W. Ketterle, K.-K. Ni, and J. M. Doyle, Science **365**, 1156 (2019).

[73] L. W. Cheuk, L. Anderegg, B. L. Augenbraun, Y. Bao, S. Burchesky, W. Ketterle, and J. M. Doyle, Phys. Rev. Lett. **121**, 083201 (2018).

[74] K.-K. Ni, S. Ospelkaus, M. De Miranda, A. Pe'Er, B. Neyenhuis, J. Zirbel, S. Kotochigova, P. Julienne, D. Jin, and J. Ye, Science **322**, 231 (2008).

[75] L. De Marco, G. Valtolina, K. Matsuda, W. G. Tobias, J. P. Covey, and J. Ye, Science **363**, 853 (2019).

[76] T. M. Rvachov, H. Son, A. T. Sommer, S. Ebadi, J. J. Park, M. W. Zwierlein, W. Ketterle, and A. O. Jamison, Phys. Rev. Lett. **119**, 143001 (2017).

[77] J. Ulmanis, J. Deiglmayr, M. Repp, R. Wester, and M. Weidemüller, Chem. Rev. **112**, 4890 (2012).

[78] L. Liu, J. Hood, Y. Yu, J. Zhang, K. Wang, Y.-W. Lin, T. Rosenband, and K.-K. Ni, Phys. Rev. X **9**, 021039 (2019).

[79] C. P. Koch and M. Shapiro, Chem. Rev. **112**, 4928 (2012).

[80] J. M. Hayes and G. J. Small, Anal. Chem. **55**, 565A (1983).

[81] B. R. Cameron, *Investigations of the flow dynamics of supersonic molecular beams and the ionization of molecular clusters by electron impact*, Ph.D. thesis, University of Canterbury (1993).

[82] R. E. Smalley, L. Wharton, and D. H. Levy, Acc. Chem. Res. **10**, 139 (1977).

[83] A. Osterwalder, EPJ Techniques and Instrumentation **2**, 10 (2015).

[84] Q. Wei, I. Lyuksyutov, and D. Herschbach, J. Chem. Phys. **137**, 054202 (2012).

[85] M. D. Morse, Experimental methods in the physical Sciences **29**, 21 (1996).

[86] U. Even, EPJ Techniques and Instrumentation **2**, 17 (2015).

[87] J. M. Hollas and D. Phillips, *Jet spectroscopy and molecular dynamics* (Springer Science & Business Media, 1994).

[88] N. R. Hutzler, H.-I. Lu, and J. M. Doyle, Chem. Rev. **112**, 4803 (2012).

[89] H. Lu, *Magnetic trapping of molecules via optical loading and magnetic slowing*, Ph.D. thesis, Harvard University (2013).

[90] D. Patterson and J. M. Doyle, J. Chem. Phys. **126**, 154307 (2007).

[91] W. C. Campbell and J. M. Doyle, Cold molecules: theory, experiment, applications , 473 (2009).

[92] S. C. Doret, C. B. Connolly, W. Ketterle, and J. M. Doyle, Phys. Rev. Lett. **103**, 103005 (2009).

[93] J. M. Doyle, B. Friedrich, J. Kim, and D. Patterson, Phys. Rev. A **52**, R2515 (1995).

[94] S. E. Maxwell, N. Brahms, R. deCarvalho, D. R. Glenn, J. Helton, S. V. Nguyen, D. Patterson, J. Petricka, D. DeMille, and J. M. Doyle, Phys. Rev. Lett. **95**, 173201 (2005).

[95] B. Hemmerling, G. K. Drayna, E. Chae, A. Ravi, and J. M. Doyle, New J. Phys. **16**, 063070 (2014).

[96] J. Baron, W. C. Campbell, D. DeMille, J. M. Doyle, G. Gabrielse, Y. V. Gurevich, P. W. Hess, N. R. Hutzler, E. Kirilov, I. Kozyryev, *et al.*, Science **343**, 269 (2014).

[97] Y. Segev, M. Pitzer, M. Karpov, N. Akerman, J. Narevicius, and E. Narevicius, Nature **572**, 189 (2019).

[98] Y. Liu, M. Vashishta, P. Djuricanin, S. Zhou, W. Zhong, T. Mittertreiner, D. Carty, and T. Momose, Phys. Rev. Lett. **118**, 093201 (2017).

[99] B. C. Sawyer, B. L. Lev, E. R. Hudson, B. K. Stuhl, M. Lara, J. L. Bohn, and J. Ye, Phys. Rev. Lett. **98**, 253002 (2007).

[100] H. Williams, L. Caldwell, N. Fitch, S. Truppe, J. Rodewald, E. Hinds, B. Sauer, and M. Tarbutt, Phys. Rev. Lett. **120**, 163201 (2018).

[101] D. McCarron, M. Steinecker, Y. Zhu, and D. DeMille, Phys. Rev. Lett. **121**, 013202 (2018).

[102] S. Y. van de Meerakker, P. H. Smeets, N. Vanhaecke, R. T. Jongma, and G. Meijer, Phys. Rev. Lett. **94**, 023004 (2005).

[103] T. Rieger, T. Junglen, S. A. Rangwala, P. W. Pinkse, and G. Rempe, Phys. Rev. Lett. **95**, 173002 (2005).

[104] S. Hoekstra, M. Metsälä, P. C. Zieger, L. Scharfenberg, J. J. Gilijamse, G. Meijer, and S. Y. van de Meerakker, Phys. Rev. A **76**, 063408 (2007).

[105] B. K. Stuhl, M. T. Hummon, M. Yeo, G. Quéméner, J. L. Bohn, and J. Ye, Nature **492**, 396 (2012).

[106] A. L. Collopy, S. Ding, Y. Wu, I. A. Finneran, L. Anderegg, B. L. Augenbraun, J. M. Doyle, and J. Ye, Phys. Rev. Lett. **121**, 213201 (2018).

[107] J. F. Barry, D. McCarron, E. Norrgard, M. Steinecker, and D. DeMille, Nature **512**, 286 (2014).

[108] H. Williams, S. Truppe, M. Hambach, L. Caldwell, N. Fitch, E. Hinds, B. Sauer, and M. Tarbutt, New J. Phys. **19**, 113035 (2017).

[109] L. Anderegg, B. L. Augenbraun, Y. Bao, S. Burchesky, L. W. Cheuk, W. Ketterle, and J. M. Doyle, Nat. Phys. **14**, 890 (2018).

[110] A. Prehn, M. Ibrügger, R. Glöckner, G. Rempe, and M. Zeppenfeld, Phys. Rev. Lett. **116**, 063005 (2016).

[111] M. Zeppenfeld, B. G. Englert, R. Glöckner, A. Prehn, M. Mielenz, C. Sommer, L. D. van Buuren, M. Motsch, and G. Rempe, Nature **491**, 570 (2012).

[112] M. Zeppenfeld, M. Motsch, P. W. Pinkse, and G. Rempe, Phys. Rev. A **80**, 041401 (2009).

[113] S. Y. van de Meerakker, H. L. Bethlem, N. Vanhaecke, and G. Meijer, Chem. Rev. **112**, 4828 (2012).

[114] S. Y. Van De Meerakker, H. L. Bethlem, and G. Meijer, Nat. Phys. **4**, 595 (2008).

[115] E. Narevicius and M. G. Raizen, Chem. Rev. **112**, 4879 (2012).

[116] R. Fulton, A. I. Bishop, M. N. Shneider, and P. F. Barker, Nat. Phys. **2**, 465 (2006).

[117] E. Lavert-Ofir, S. Gersten, A. B. Henson, I. Shani, L. David, J. Narevicius, and E. Narevicius, New J. Phys. **13**, 103030 (2011).

[118] S. Chervenkov, X. Wu, J. Bayerl, A. Rohlfes, T. Gantner, M. Zeppenfeld, and G. Rempe, Phys. Rev. Lett. **112**, 013001 (2014).

[119] X. Wu, T. Gantner, M. Koller, M. Zeppenfeld, S. Chervenkov, and G. Rempe, Science **358**, 645 (2017).

[120] N. Fitch and M. Tarbutt, ChemPhysChem **17**, 3609 (2016).

[121] M. Petzold, P. Kaebert, P. Gersema, M. Siercke, and S. Ospelkaus, New J. Phys. **20**, 042001 (2018).

[122] J. F. Barry, E. Shuman, E. Norrgard, and D. DeMille, Phys. Rev. Lett. **108**, 103002 (2012).

[123] B. Hemmerling, E. Chae, A. Ravi, L. Anderegg, G. K. Drayna, N. R. Hutzler, A. L. Collopy, J. Ye, W. Ketterle, and J. M. Doyle, J. Phys. B **49**, 174001 (2016).

[124] M. Yeo, M. T. Hummon, A. L. Collopy, B. Yan, B. Hemmerling, E. Chae, J. M. Doyle, and J. Ye, Phys. Rev. Lett. **114**, 223003 (2015).

[125] S. Truppe, H. Williams, N. Fitch, M. Hambach, T. Wall, E. Hinds, B. Sauer, and M. Tarbutt, New J. Phys. **19**, 022001 (2017).

[126] M. Di Rosa, Eur. Phys. J. D **31**, 395 (2004).

[127] T. Chen, W. Bu, and B. Yan, Phys. Rev. A **94**, 063415 (2016).

[128] T. Isaev, S. Hoekstra, and R. Berger, Phys. Rev. A **82**, 052521 (2010).

[129] A. M. Ellis, Int. Rev. Phys. Chem. **20**, 551 (2001).

[130] T. A. Isaev and R. Berger, Phys. Rev. Lett. **116**, 063006 (2016).

[131] W. Demtröder, *Mol. Phys.: theoretical principles and experimental methods* (John Wiley & Sons, 2008).

[132] P. F. Bernath, *Spectra of atoms and molecules* (Oxford university press, 2015).

[133] M. Born and J. R. Oppenheimer, Ann. Physik (1927), http://elib.bsu.by/handle/123456789/154381.

[134] J. M. Brown, J. M. Brown, and A. Carrington, *Rotational spectroscopy of diatomic molecules* (Cambridge University Press, 2003).

[135] A. Allouche, G. Wannous, and M. Aubert-Frécon, Chem. Phys. **170**, 11 (1993).

[136] M. J. Dick, *Spectroscopy of selected calcium and strontium containing polyatomic molecules*, Ph.D. thesis, University of Waterloo (2007).

[137] G. Herzberg, *Molecular spectra and molecular structure. Vol. 3: Electronic spectra and electronic structure of polyatomic molecules* (New York: Van Nostrand, Reinhold, 1966).

[138] C. H. Townes and A. L. Schawlow, *Microwave spectroscopy* (Courier Corporation, 2013).

[139] G. Herzberg, *Spectra of diatomic molecules, molecular spectra and molecular structure* (Van Nostrand, New York, 1950).

[140] R. L. C. Walter Gordy, *Microwave Molecular Spectroscopy* (John Wiley & Sons, 1984).

[141] R. C. Hilborn, Z. Qingshi, and D. O. Harris, J. Mol. Spec **97**, 73 (1983).

[142] C. Scurlock, D. Fletcher, and T. Steimle, J. Mol. Spec. **159**, 350 (1993).

[143] J. A. Coxon, M. Li, and P. I. Presunka, Mol. Phys. **76**, 1463 (1992).

[144] P. I. Presunka and J. A. Coxon, J. Chem. Phys. **101**, 201 (1994).

[145] A. Merer and J. Allegretti, Can. J. Phys. **49**, 2859 (1971).

[146] M. Li and J. A. Coxon, J. Chem. Phys. **97**, 8961 (1992).

[147] E. Chae, L. Anderegg, B. L. Augenbraun, A. Ravi, B. Hemmerling, N. R. Hutzler, A. L. Collopy, J. Ye, W. Ketterle, and J. M. Doyle, New J. Phys. **19**, 033035 (2017).

[148] I. Kozyryev, L. Baum, K. Matsuda, B. L. Augenbraun, L. Anderegg, A. P. Sedlack, and J. M. Doyle, Phys. Rev. Lett. **118**, 173201 (2017).

[149] B. K. Stuhl, B. C. Sawyer, D. Wang, and J. Ye, Phys. Rev. Lett. **101**, 243002 (2008).

[150] I. Kozyryev, T. C. Steimle, P. Yu, D.-T. Nguyen, and J. M. Doyle, New J. Phys. **21**, 052002 (2019).

[151] N. H. Rosenbaum, J. C. Owrutsky, L. M. Tack, and R. J. Saykally, J. Chem. Phys. **84**, 5308 (1986).

[152] D. R. Lide Jr and C. Matsumura, J. Chem. Phys. **50**, 3080 (1969).

[153] M. Li, *High Resolution Laser Spectroscopy of the* $\tilde{A}^2\Pi$ - $\tilde{X}^2\Sigma^+$ *system of CaOH and CaOD Radicals*, Ph.D. thesis, Dalhousie University (1995).

[154] L. M. Ziurys, W. Barclay Jr, and M. Anderson, Astrophys. J. **384**, L63 (1992).

[155] P. Bernath and C. Brazier, Astrophys. J. **288**, 373 (1985).

[156] P. Bernath and S. Kinsey-Nielsen, Chem. Phys. Lett. **105**, 663 (1984).

[157] C. Jarman and P. Bernath, J. Chem. Phys. **97**, 1711 (1992).

[158] J. A. Coxon, M. Li, and P. I. Presunka, J. Mol. Spec **164**, 118 (1994).

[159] E. Toolbox, "Emissivity coefficients materials," (2003).

[160] P. Fortescue, G. Swinerd, and J. Stark, *Spacecraft systems engineering* (John Wiley & Sons, 2011).

[161] E. Marquardt, J. Le, and R. Radebaugh, in *Cryocoolers 11* (Springer, 2002) pp. 681–687.

[162] J. Ekin, *Experimental techniques for low-temperature measurements: cryostat design, material properties and superconductor critical-current testing* (Oxford university press, 2006).

[163] W. C. Campbell, *Magnetic Trapping of Imidogen Molecules*, Ph.D. thesis, Harvard University (2008).

[164] D. Sedgley, A. Tobin, T. Batzer, and W. Call, J. Vac. Sci. Technol. A **5**, 2572 (1987).

[165] P. A. Lessard, J. Vac. Sci. Technol. A **7**, 2373 (1989).

[166] A. Van Itterbeek and W. Van Dingenen, Physica **5**, 529 (1938).

[167] I. Kozyryev, *Laser cooling and Inelastic Collisions of the Polyatomic Radical SrOH*, Ph.D. thesis, Harvard University (2017).

[168] G. A. Miller, J. Chem. Eng. Data **9**, 418 (1964).

[169] H. F. Gibbard and J. L. Creek, J. Chem. Eng. Data **19**, 308 (1974).

[170] M. D. Oberlander and J. M. Parson, J. Chem. Phys. **105**, 5806 (1996).

[171] I. Kozyryev, L. Baum, K. Matsuda, P. Olson, B. Hemmerling, and J. M. Doyle, New J. Phys. **17**, 045003 (2015).

[172] A. Roth, *Vacuum technology* (Elsevier, 2012).

[173] J. B. Hasted, *Physics of atomic collisions* (Butterworth & Co., 1972).

[174] J. D. Weinstein, *Magnetic Trapping of Atomic Chromium and Molecular Calcium Monohydride*, Ph.D. thesis, Harvard University (2001).

[175] K. Maussang, D. Egorov, J. S. Helton, S. V. Nguyen, and J. M. Doyle, Phys. Rev. Lett. **94**, 123002 (2005).

[176] H.-I. Lu, J. Rasmussen, M. J. Wright, D. Patterson, and J. M. Doyle, Phys. Chem. Chem. Phys. **13**, 18986 (2011).

[177] D. Budker, D. Kimball, D. F. Kimball, and D. P. DeMille, *Atomic physics: an exploration through problems and solutions* (Oxford University Press, USA, 2004).

[178] D. Trung, Private Communication (2019).

[179] J. F. Barry, E. Shuman, and D. DeMille, Phys. Chem. Chem. Phys. **13**, 18936 (2011).

[180] R. A. Hailey, *Laser spectroscopy of calcium monohydroxide and calcium monodeuteroxide*, Master's thesis, Univeristy of Arizona (1991).

[181] M. D. Oberlander, *Laser excited fluorescence studies of reactions of group 2 metals with oxygen containing molecules and of heavy group 15 clusters with fluorine*, Ph.D. thesis, Ohio State University (1995).

[182] A. L. Collopy, *A Three-Dimensional MOT of YO Towards Narrow-Line Cooling*, Ph.D. thesis, University of Colorado (2018).

[183] J. F. Barry, *Laser cooling and slowing of a diatomic molecule*, Ph.D. thesis, Yale University (2013).

[184] S. Truppe, M. Hambach, S. M. Skoff, N. E. Bulleid, J. S. Bumby, R. J. Hendricks, E. A. Hinds, B. E. Sauer, and M. R. Tarbutt, J. Mod. Opt. **65**, 648 (2018).

[185] A. Lurio, R. DeZafra, and R. J. Goshen, Phys. Rev. **134**, A1198 (1964).

[186] R. Drozdowski, M. Ignaciuk, J. Kwela, and J. Heldt, Zeitschrift für Physik D Atoms, Molecules and Clusters **41**, 125 (1997).

[187] P. F. Bernath, Science **254**, 665 (1991).

[188] P. F. Bernath, Advances in Photochemistry **23**, 1 (1997).

[189] A. Jadbabaie, N. H. Pilgram, J. Klos, S. Kotochigova, and N. R. Hutzler, New J. Phys. (2020), https://doi.org/10.1088/1367-2630/ab6eae.

[190] I. Norris, *Laser Cooling and Trapping of Neutral Calcium Atoms*, Ph.D. thesis, University of Strathclyde (2009).

[191] M. Tarbutt and T. Steimle, Phys. Rev. A **92**, 053401 (2015).

[192] L. Baum, N. B. Vilas, C. Hallas, B. L. Augenbraun, S. Raval, D. Mitra, and J. M. Doyle, Phys. Rev. Lett. **124**, 133201 (2020).

[193] E. Chae, *Laser Slowing of CaF Molecules and Progress towards a Dual-MOT for Li and CaF*, Ph.D. thesis, Harvard University (2015).

[194] D. E. Oates and J. G. King, Phys. Rev. Lett. **26**, 735 (1971).

[195] M. Hamamda, P. Pillet, H. Lignier, and D. Comparat, J. Phys. B **48**, 182001 (2015).

[196] P. Asenbaum, S. Kuhn, S. Nimmrichter, U. Sezer, and M. Arndt, Nat. Commun. **4**, 1 (2013).

[197] R. Peterson, T. Purdy, N. Kampel, R. Andrews, P.-L. Yu, K. Lehnert, and C. Regal, Phys. Rev. Lett. **116**, 063601 (2016).

[198] J. Chan, T. M. Alegre, A. H. Safavi-Naeini, J. T. Hill, A. Krause, S. Gröblacher, M. Aspelmeyer, and O. Painter, Nature **478**, 89 (2011).

[199] N. Kiesel, F. Blaser, U. Delić, D. Grass, R. Kaltenbaek, and M. Aspelmeyer, PNAS **110**, 14180 (2013).

[200] S. Eibenberger, X. Cheng, J. Cotter, and M. Arndt, Phys. Rev. Lett. **112**, 250402 (2014).

[201] E. Shuman, J. F. Barry, D. Glenn, and D. DeMille, Phys. Rev. Lett. **103**, 223001 (2009).

[202] D. McCarron, E. Norrgard, M. Steinecker, and D. DeMille, New J. Phys. **17**, 035014 (2015).

[203] E. Norrgard, D. McCarron, M. Steinecker, M. Tarbutt, and D. DeMille, Phys. Rev. Lett. **116**, 063004 (2016).

[204] M. H. Steinecker, D. J. McCarron, Y. Zhu, and D. DeMille, ChemPhysChem **17**, 3664 (2016).

[205] S. Truppe, H. Williams, M. Hambach, L. Caldwell, N. Fitch, E. Hinds, B. Sauer, and M. Tarbutt, Nat. Phys. **13**, 1173 (2017).

[206] L. Caldwell, J. Devlin, H. Williams, N. Fitch, E. Hinds, B. Sauer, and M. Tarbutt, Phys. Rev. Lett. **123**, 033202 (2019).

[207] I. Kozyryev, L. Baum, K. Matsuda, B. Hemmerling, and J. M. Doyle, J. Phys. B **49**, 134002 (2016).

[208] H. J. Metcalf and P. van der Straten, JOSA B **20**, 887 (2003).

[209] C. J. Foot *et al.*, *Atomic physics*, Vol. 7 (Oxford University Press, 2005).

[210] T. Sharp and H. Rosenstock, J. Chem. Phys. **41**, 3453 (1964).

[211] E. Fermi, Zeitschrift für Physik **71**, 250 (1931).

[212] J. A. Coxon, M. Li, and P. I. Presunka, J. Mol. Spec **150**, 33 (1991).

[213] M. Li and J. A. Coxon, J. Chem. Phys. **104**, 4961 (1996).

[214] C. Brazier and P. Bernath, J. Mol. Spec. **114**, 163 (1985).

[215] E. Hirota, *High-resolution spectroscopy of transient molecules*, Vol. 40 (Springer Science & Business Media, 2012).

[216] J. Brown, J. Mol. Spec **68**, 412 (1977).

[217] E. Raab, M. Prentiss, A. Cable, S. Chu, and D. E. Pritchard, Phys. Rev. Lett. **59**, 2631 (1987).

[218] M. Tarbutt, New J. Phys. **17**, 015007 (2015).

[219] R. Fulton, A. I. Bishop, and P. F. Barker, Phys. Rev. Lett. **93**, 243004 (2004).

[220] N. Vanhaecke, U. Meier, M. Andrist, B. H. Meier, and F. Merkt, Phys. Rev. A **75**, 031402 (2007).

[221] E. B. Norrgard, N. Sitaraman, J. F. Barry, D. McCarron, M. H. Steinecker, and D. DeMille, Rev. Sci. Instrum. **87**, 053119 (2016).

[222] E. Erikson, D. Berger, and B. Frazier, J. Vac. Sci. Technol., A **3**, 1711 (1985).

[223] A. collaboration, New J. Phys. **19**, 073029 (2017).

[224] D. Boiron, A. Michaud, P. Lemonde, Y. Castin, C. Salomon, S. Weyers, K. Szymaniec, L. Cognet, and A. Clairon, Phys. Rev. A **53**, R3734 (1996).

[225] G. Grynberg and J.-Y. Courtois, EPL (Europhysics Lett.) **27**, 41 (1994).

[226] D. R. Fernandes, F. Sievers, N. Kretzschmar, S. Wu, C. Salomon, and F. Chevy, EPL (Europhysics Lett.) **100**, 63001 (2012).

[227] F. Sievers, N. Kretzschmar, D. R. Fernandes, D. Suchet, M. Rabinovic, S. Wu, C. V. Parker, L. Khaykovich, C. Salomon, and F. Chevy, Phys. Rev. A **91**, 023426 (2015).

[228] J. Devlin and M. Tarbutt, New J. Phys. **18** (2016), https://doi.org/10.1088/1367-2630/18/12/123017.

[229] S. Ding, Y. Wu, I. A. Finneran, J. J. Burau, and J. Ye, arXiv (2020), https://arxiv.org/abs/2002.00056.

[230] M. L. Wall, K. Maeda, and L. D. Carr, Ann. Phys. (Berlin) **525**, 845 (2013).

[231] N. Balakrishnan, J. Chem. Phys. **145**, 150901 (2016).

[232] R. V. Krems, Phys. Chem. Chem. Phys. **10**, 4079 (2008).

[233] R. W. Boyd, *Nonlinear optics* (Elsevier, 2003).

[234] P. Maker, R. Terhune, M. Nisenoff, and C. Savage, Phys. Rev. Lett. **8**, 21 (1962).

[235] M. Hobden, J. Appl. Phys. **38**, 4365 (1967).

[236] R. Eckardt and J. Reintjes, IEEE J.of quantum electronics **20**, 1178 (1984).

[237] A. M. Schober, M. Charbonneau-Lefort, and M. M. Fejer, JOSA B **22**, 1699 (2005).

[238] D. S. Hum and M. M. Fejer, Comptes Rendus Physique **8**, 180 (2007).

[239] J. Yue, C.-Y. She, B. Williams, J. Vance, P. Acott, and T. Kawahara, Opt. Lett. **34**, 1093 (2009).

[240] H.-Y. Lo, J. Alonso, D. Kienzler, B. C. Keitch, L. E. de Clercq, V. Negnevitsky, and J. P. Home, App. Phys. B **114**, 17 (2014).

[241] M. Tawfieq, O. B. Jensen, A. K. Hansen, B. Sumpf, K. Paschke, and P. E. Andersen, Opt. Commun. **339**, 137 (2015).

[242] R. Rengelink, R. Notermans, and W. Vassen, App. Phys. B **122**, 122 (2016).

[243] J. Wang, J. Bai, J. He, and J. Wang, Opt. Commun. **370**, 150 (2016).

[244] D. N. Nikogosyan, *Nonlinear optical crystals: a complete survey* (Springer Science & Business Media, 2006).

[245] K. Niwa, Y. Furukawa, S. Takekawa, and K. Kitamura, J.of Crystal Growth **208**, 493 (2000).

[246] F. Jermann, M. Simon, and E. Krätzig, J. Opt. Soc. Am. B **12**, 2066 (1995).

[247] Y. Furukawa, K. Kitamura, A. Alexandrovski, R. Route, M. Fejer, and G. Foulon, App. Phys. Lett. **78**, 1970 (2001).

[248] G. Boyd and D. Kleinman, J. App. Phys. **39**, 3597 (1968).

[249] M. A. de Araújo, R. Silva, E. de Lima, D. P. Pereira, and P. C. de Oliveira, App. Opt. **48**, 393 (2009).

[250] A. Glassford, J. Space. Rock. **7**, 1464 (1970).

[251] D. Sedgley, T. Batzer, and W. Call, J. Vac. Sci. Technol. A **6**, 1209 (1988).

[252] L. Gurevich, V. Petrovsky, and A. Pustovoit, Plasma Devices Oper. **1**, 97 (1990).

[253] E. P. West, *A Thermochemical Cryogenic Buffer Gas Beam Source of ThO for Measuring the Electric Dipole Moment of the Electron*, Ph.D. thesis, Harvard University (2017).

[254] R. Pereira and D. H. Levy, J. Chem. Phys. **105**, 9733 (1996)